

# Silicon Quantum Electronics

Floris A. Zwanenburg\*

*NanoElectronics Group MESA+ Institute for Nanotechnology University of Twente,  
Enschede The Netherlands  
Centre of Excellence for Quantum Computation and Communication Technology,  
The University of New South Wales Sydney Australia*

Andrew S. Dzurak, Andrea Morello, Michelle Y. Simmons

*Centre of Excellence for Quantum Computation and Communication Technology,  
The University of New South Wales Sydney Australia*

Lloyd C. L. Hollenberg

*Centre of Excellence for Quantum Computation and Communication Technology,  
University of Melbourne Melbourne Australia*

Gerhard Klimeck

*School of Electrical and Computer Engineering Birck Nanotechnology Center,  
Network for Computational Nanotechnology Purdue University West Lafayette Indiana USA*

Sven Rogge

*Centre of Excellence for Quantum Computation and Communication Technology,  
The University of New South Wales Sydney Australia  
Kavli Institute of Nanoscience Delft University of Technology Delft The Netherlands*

Susan N. Coppersmith, Mark A. Eriksson

*University of Wisconsin-Madison Madison Wisconsin USA*

(Dated: June 23, 2022)

This review describes recent groundbreaking results in Si, Si/SiGe and dopant-based quantum dots, and it highlights the remarkable advances in Si-based quantum physics that have occurred in the past few years. This progress has been possible thanks to materials development for both Si quantum devices, and thanks to the physical understanding of quantum effects in silicon. Recent critical steps include the isolation of single electrons, the observation of spin blockade and single-shot read-out of individual electron spins in both dopants and gated quantum dots in Si. Each of these results has come with physics that was not anticipated from previous work in other material systems. These advances underline the significant progress towards the realization of spin quantum bits in a material with a long spin coherence time, crucial for quantum computation and spintronics.

## CONTENTS

I. Introduction and motivation	2	III. Physics of Si nanostructures	8
A. Silicon Quantum Electronics	2	A. Bulk silicon: valley degeneracy	8
B. Outline of this review	3	B. Quantum wells and dots	10
II. Quantum confinement	3	1. Valley splitting in quantum dots	10
A. From single atoms to quantum wells	3	2. Mixing of valleys and orbits	11
B. Transport regimes	4	C. Dopants in Si	13
1. The multi-electron regime	7	1. Wave function engineering of single dopant electron states	13
2. The sequential multi-level regime	7	2. Two-donor systems and exchange coupling	15
3. The sequential single-level regime	7	3. Planar donor structures: delta-doped layers and nanowires	17
4. The coherent regime	7	IV. Quantum dots in Si and SiGe	18
5. The Kondo regime	8	A. Early work: Coulomb blockade in silicon	18
		B. Single quantum dots	19
		1. Self-assembled nanocrystals	19
		2. Bottom-up grown nanowires	20
		3. Electrostatically Gated Si/SiGe quantum dots	20
		4. Quantum dots in planar MOS structures	22

\* f.a.zwanenburg@utwente.nl

5. Quantum dots in etched silicon nanowires	24
C. Charge sensing techniques	25
D. Few-electron quantum dots	26
E. Spins in single quantum dots	27
1. Spin-state spectroscopy	28
2. Spin filling in valleys and orbits	28
F. Double quantum dots	29
1. Charge-state control	29
2. Spin transport in double quantum dots	32
V. Dopants in silicon	33
A. Dopants in silicon transistors	33
1. Early work: mesoscopic silicon transistors	33
2. Nano-scale transistors	34
B. Single dopant transistors	34
1. The demand for single dopant architectures	34
2. Single dopants in MOS-based architectures	36
3. Single dopants in crystalline silicon	39
C. Discussion	41
1. Orbital structure of a dopant in a nanostructure	42
2. Charging energy of a dopant in a nanostructure	42
3. Interactions between donors	43
D. Double dopant quantum dots	43
E. Charge sensing in few-electron dopants	44
VI. Outlook: relaxation, coherence and measurements	45
A. Spin relaxation and decoherence	45
1. Electron spin relaxation in donors	46
2. Electron spin relaxation in quantum dots	47
3. Singlet-triplet relaxation	48
4. Spin decoherence	48
B. Orbital and valley relaxation	49
C. Control and readout of spins in silicon	50
1. Bulk spin resonance	50
2. Electrically-detected magnetic resonance	51
3. Single-shot readout of a single electron spin	51
4. Readout and control of singlet-triplet states in double quantum dots	53
Acknowledgments	54
A. One-dimensional tight-binding model with valley degeneracy	54
B. Effective mass theory for quantum wells	56
C. Atomistic treatment of valley splitting in silicon	57
1. Atomistic representations for nanometer-scaled devices	57
2. Atomistic valley splitting in ideal, freestanding slabs	58
3. Atomistic description of disorder in SiGe alloys	59
a. Atom-type-disorder	59
b. Atom-position-disorder	59
c. Alloy concentration disorder	60
4. Valley splitting in disordered systems	60
a. Flat disordered SiGe buffers	60
b. A slanted Si quantum well without explicit SiGe	60
c. A slanted Si quantum well with disordered SiGe buffer	60
d. A slanted Si quantum well with disordered steps without SiGe buffer	61
e. A slanted Si quantum well with disordered $\text{Si}_x\text{Ge}_{1-x}$ buffer and disordered steps	61
f. Flat disordered SiGe buffer - effects of system size	62
g. Buffer fluctuations - conclusions	62
References	62

## I. INTRODUCTION AND MOTIVATION

### A. Silicon Quantum Electronics

The exponential progress of microelectronics in the last half century has been based on silicon technology. After decades of progress and the incorporation of many new materials, the core technological platform for classical computation remains based on silicon. At the same time, it is becoming increasingly evident that silicon can be an excellent host material for an entirely new generation of devices, based on the quantum properties of charges and spins. These range from quantum computers to a wide spectrum of spintronics applications. Silicon is an ideal environment for spins in the solid state, due to its weak spin-orbit coupling and the existence of isotopes with zero nuclear spin. The prospect of combining quantum spin control with the exquisite fabrication technology already in place for classical computers has encouraged extensive effort in silicon-based quantum devices over the past decade.

While there are many proposed physical realizations for quantum information processors (Ladd *et al.*, 2010; Lloyd, 1993), semiconductor-based quantum bits (qubits) are extremely interesting, in no small part because of their commonalities with classical electronics (Kane, 1998; Loss and DiVincenzo, 1998). Electron spins in quantum dots have received considerable attention, and significant experimental progress has been made since Loss and DiVincenzo (1998) presented their original proposal. Experiments on lithographically defined quantum dots in GaAs/AlGaAs heterostructures have shown qubit initialization, single-shot single-electron spin readout (Elzerman *et al.*, 2004), and coherent control of single-spin (Koppens *et al.*, 2006) and two-spin (Petta *et al.*, 2005) states. One of the major issues in AlGaAs/GaAs heterostructures is the inevitable presence of nuclear spins in the host material, leading to relatively short spin relaxation and coherence times.

A way to increase the coherence time is to use materials with a large fraction of non-magnetic nuclei. Natural silicon consists of 95% non-magnetic nuclei (92%  $^{28}\text{Si}$  and 3%  $^{30}\text{Si}$ ) and carbon even of 99% ( $^{12}\text{C}$ ). Moreover, both materials can be purified to nearly 100% zero-nuclear-spin isotopes. For these reasons, various proposals have been made for electron spin qubits based on donors (De Sousa *et al.*, 2004; Hill *et al.*, 2005; Hollenberg *et al.*, 2006; Vrijen *et al.*, 2000) in Si and quantum dots Si (Friesen *et al.*, 2003) and graphene (Trauzettel *et al.*, 2007). The key requirement for spin quantum bits is to confine single electrons to either a quantum dot or a donor, thus posing a scientific challenge. In contrast with the technological maturity of classical field-effect transistors, Si quantum dot systems have lagged behind GaAs systems, which were historically more advanced because of the very early work in epitaxial growth

in lattice-matched III-V materials. Kouwenhoven *et al.* (1997b) studied the excitation spectra of a single-electron quantum dot in a III-V material. Even though Coulomb blockade in Si structures was observed very early (Ali and Ahmed, 1994; Paul *et al.*, 1993), it took another 5 years before regular Coulomb oscillations were reported (Simmel *et al.*, 1999). Silicon systems needed nearly ten years to reach the single-electron occupation in quantum dots (Lim *et al.*, 2009b; Simmons *et al.*, 2007; Zwanenburg *et al.*, 2009b) and dopants (Fuechsle *et al.*, 2011; Sellier *et al.*, 2006). For quantum dots this has laid the foundation for spin filling in valleys in few-electron quantum dots (Borselli *et al.*, 2011a; Lim *et al.*, 2011), tunnel rate measurements in few-electron single and double quantum dots (Thalakulam *et al.*, 2010), Pauli spin blockade in the few-electron regime (Borselli *et al.*, 2011b), and very recently Rabi oscillations of singlet-triplet states (Maune *et al.*, 2012). In case of dopants valley excited states have been reported (Fuechsle *et al.*, 2010), gate-induced quantum-confinement transition of a single dopant atom (Lansbergen *et al.*, 2008), a deterministically fabricated single-atom transistor (Fuechsle *et al.*, 2011) and single-shot read out of an electron spin bound to a phosphorus donor (Morello *et al.*, 2010). All these results underline the incredible potential of silicon for quantum information processing.

It is tempting to project the achievements in integrated-circuit technology onto a supposed scalability of quantum bits in silicon. Even though current silicon industry standards, with 22 nm features, have higher resolution than typical quantum devices discussed in this review, superb patterning alone does not guarantee any sort of 'quantum CMOS' (Complementary Metal-Oxide-Semiconductor). As one example, interface traps have a very different effect on classical transistors (where they serve as scattering centers or shift threshold voltages) than in quantum dots (where issues of spin coherence also come into play). Nonetheless, a fully-integrated CMOS foundry has been used for many steps in the fabrication of silicon quantum devices (Nordberg *et al.*, 2009a).

While silicon-based devices generate special interest for quantum computation, because of zero nuclear spin isotopes and low spin-orbit coupling, they also face some special challenges and display physics that, until recently, has been little explored in the context of quantum computation. Examples of the challenges include the relatively large effective mass in silicon and the large difference in lattice constant between silicon and germanium. An example of the unexplored physics is the presence of multiple conduction band valleys in silicon.

As described in this review, there have been rapid advances addressing the challenges and exploring the new physics available in silicon-based quantum devices. The extent to which these advances will lead to larger-scale quantum systems in silicon is an exciting question as of this writing.

## B. Outline of this review

This review covers the field of electronic transport in silicon and focuses on single-electron tunneling through quantum dots and dopants. We restrict ourselves to experiments and theory involving electrons confined to single or double (dopant) quantum dots, describing the development from the observation of Coulomb blockade to single-electron quantum dots and single dopant atom transistors. Ensembles of quantum dots or dopants are beyond the scope of this article. Also, the review is strictly limited to electron transport experiments, and does not cover optical spectroscopy measurements. Optical spectroscopy on quantum dots and ensembles of dopants is a very active and emerging field, see for example the recent work by Greenland *et al.* (2010) and Steger *et al.* (2012) and references therein.

*Section II Quantum Confinement* starts with a general introduction to transport through quantum-confined silicon nanostructures. The silicon bandstructure is described in *Section III Physics of Silicon nanostructures* with specifics such as the valley degeneracy and splitting in bulk and quantum dots, and wave function control and engineering of dopant states. *Section IV Quantum dots in Si and SiGe* explains the development from the discovery of Coulomb blockade in 1990 to single-electron occupancy in single and double quantum dots in recent years. Analogously, dopant transport in silicon has evolved from tunneling through 1980's MOSFETs to current-day single-atom transistors, see *Section V Dopants in silicon*. The remarkable advances of Sections IV and V have led to the relaxation and coherence measurements on single spins in *Section VI Outlook: relaxation, coherence and measurements*.

## II. QUANTUM CONFINEMENT

This section introduces quantum electronic experiments in silicon, starting with the quantum mechanical confinement of electrons in silicon, which can be achieved by a combination electrostatic fields, interfaces between materials, and/or placement of individual atoms. All of these approaches lead to single-electron tunneling devices consisting of a silicon potential well coupled to source, drain and gate electrodes.

### A. From single atoms to quantum wells

This section describes how electrons can be confined to Si nanostructures using a combination of material and electrostatic confinement. The shape and size of nanostructured materials provide natural confinement of electrons to 0, 1 or 2 dimensions. The exact confinement potential of the structure in x, y and z-directions sets the

additional requirements in terms of additional electric fields. Figure 1 gives an overview of materials of different dimensionality and their integration into single-electron tunneling devices.

### Dopants

The electrostatic potential of a single dopant atom is radially symmetric, resulting in the same steep potential well in all directions, as shown in the first row of Fig. 1. The Bohr radius  $a_B$  is the mean radius of the orbit of an electron around the nucleus of an atom in its ground state, and equals for example 2.5 nm for phosphorus in silicon. A dopant atom has three charge states: the ionized  $D^+$  state, the neutral  $D^0$  state (one electron bound to the dopant) and the negatively charged  $D^-$  state (two electrons bound to the dopant). Because the  $D^+$  state corresponds to an empty dopant it does not appear as an electron state in the potential well. Measuring electron transport through a single atom has been a great challenge, as described in Section V, but the single-dopant regime as sketched in the third column has been reached by several groups. Depending on the architecture, the source and drain reservoirs can be made up of highly-doped Si (Fuechsle *et al.*, 2011; Pierre *et al.*, 2010; Sellier *et al.*, 2006), or of a two-dimensional electron gas (Tan *et al.*, 2010). The same goes for the gates, but they can also be metallic (Tan *et al.*, 2010). The resulting single-electron transistors consist of a steep dopant potential well connected to source and drain reservoirs.

### 0D structures

Like dopants, self-assembled nanocrystals also provide confinement to zero dimensions but the confinement is better described by a hard-wall potential well in  $x$ ,  $y$  and  $z$ -directions and is much wider (Fig. 1). The size  $L$  of a quantum well must be small enough to confine the electron wave function such that the energy levels are quantized according to basic quantum mechanics, see for example Cohen-Tannoudji *et al.* (1992). The energy level spacing  $\Delta E$  is on the order of  $h^2/m_{\text{eff}}L^2$ , where  $m_{\text{eff}}$  is the electron effective mass. The separation between energy levels thus decreases quadratically with the well width: as a result, the discrete levels of e.g. a 30 nm size nanocrystal are expected to have energy spacings 2 orders of magnitude smaller than those of a dopant with a 3 nm Bohr radius. Making source and drain contacts requires very precise alignment by means of electron-beam lithography. The tunnel coupling of these devices relies on statistics; creating tunable tunnel coupling to self-assembled dots is very challenging. A highly-doped substrate can be used as a global backgate and metallic leads on a dielectric as a local gate.

### 1D structures

The high aspect ratio of nanowires (NWs) implies a large

level spacing in the transverse directions, and a small level spacing in the longitudinal direction ( $L_x \gg L_{y,z}$ ), creating a (quasi) 1-dimensional channel with few subbands in the transverse direction (see second row of Fig. 1). Within this channel a zero-dimensional well can be created by local gates on the nanowire, or by Schottky tunnel barriers to source and drain contacts. In the latter case the barrier height is determined by the material work functions and hardly tuneable in-situ — the tunnel coupling will generally decrease as electrons leave the well and the wave function overlap with source and drain shrinks. Local gates, however, can tune the tunnel barriers since the applied gate voltage induces an electric field which locally pulls up the conduction band. Electrons tunnel from the quantum well into reservoirs which are part of the nanowire itself. The metallic leads connecting the nanowire to the macroscopic world must be ohmic; i.e., the contacts should have high transparency, to prevent the formation of multiple quantum dots in series (particularly if the contacts are very close to the quantum dot).

### 2D structures

A 2-dimensional electron gas (2DEG) can be created in a Si MOSFET (Metal-Oxide-Semiconductor Field Effect Transistor) and in Si/SiGe heterostructures. Electrons can move freely in the  $x$ - $y$ -plane and be subject to a triangular potential well perpendicular to the plane, as sketched in in Fig. 1. A more realistic band diagram is drawn in Fig. 2 in the review by Ando *et al.* (1982) for Si MOS and Fig. 11 in the review by Schäffler (1997) for Si/SiGe heterostructures. In a 2DEG-based quantum dot, the lateral confinement is a soft-wall potential that is defined by top gate electrodes, enabling tunnel-coupling to source and drain reservoirs in the 2DEG. Those reservoirs are connected to macroscopic wires via ohmic contacts, which are often highly doped regions at the edge of the chip. The resulting potential landscape has a high degree of tuneability thanks to local electrostatic gating via the top gates.

## B. Transport regimes

Having introduced quantum-confined devices we will now cover the basics of quantum transport through single-electron transistors (SETs), which are made up of a zero-dimensional island, source and drain reservoirs and gate electrodes.

Electronic measurements on single electrons require a confining potential which is tunnel coupled to electron reservoirs in source and drain leads, see Fig. 2. The SET-island is also coupled capacitively to one or more gate electrodes, which can be used to tune the electrostatic potential of the well. The discrete levels are spaced by the addition energy  $E_{\text{add}}(N) = E_C + \Delta E$ , which con-

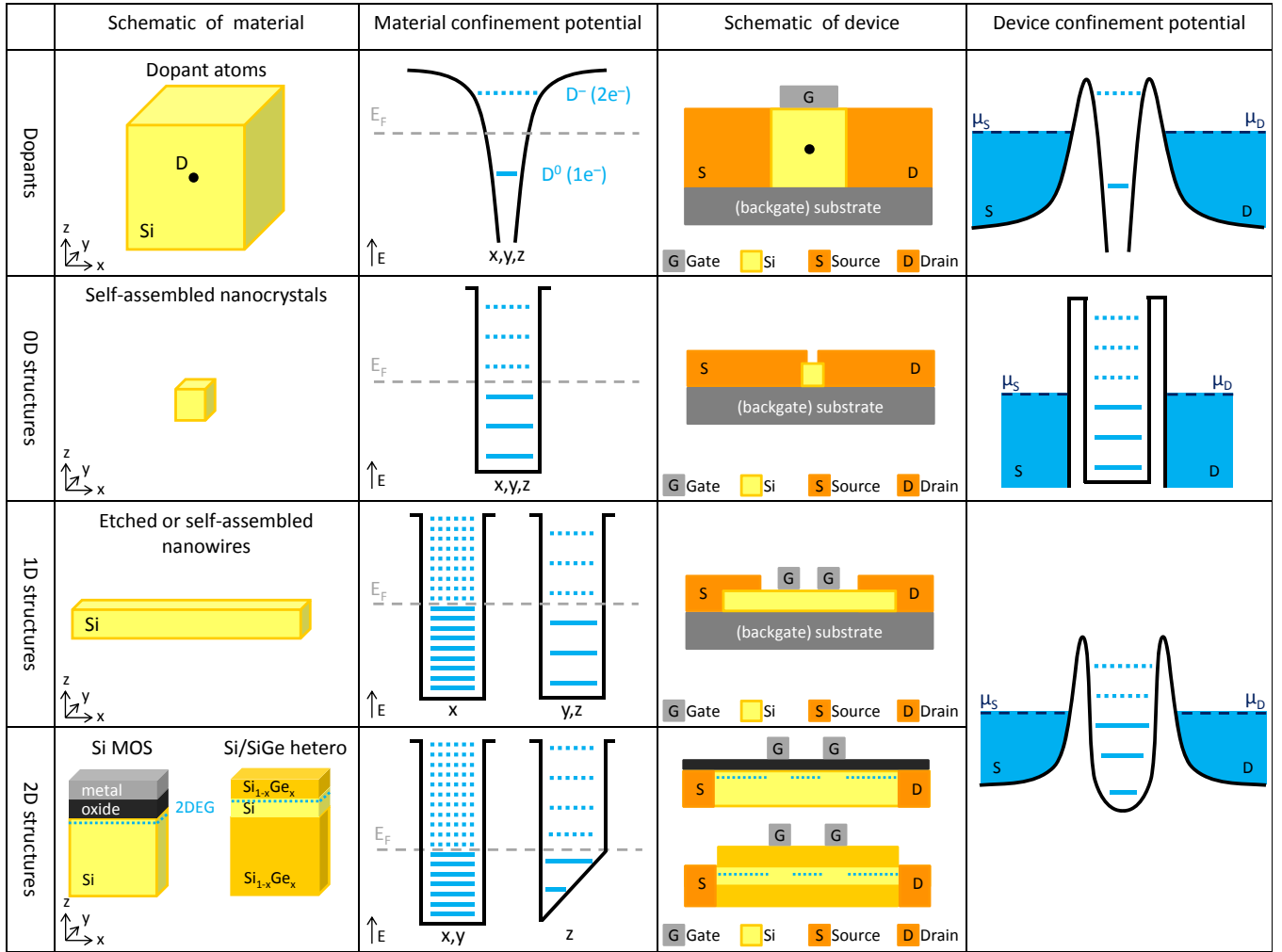


FIG. 1 **Combining material and electrostatic confinement to create single-electron transistors.** The first column shows a schematic of dopants, 0D-, 1D- and 2D-structures. Second column: in the corresponding confinement potentials in  $x$ -,  $y$ - and  $z$ -directions electron states are occupied up to the Fermi energy  $E_F$  (dashed grey line). Occupied and unoccupied electron states are indicated as straight and dashed lines respectively. Third column: Schematic of the silicon nanostructure integrated into a transport device with source, drain and gate electrodes. Fourth column: The potential landscape of the single-electron transistor is made up of a potential well which is tunnel-coupled to source and drain reservoir and electrostatically coupled to gates which can move the ladder of electrochemical potentials, as described in Section II.B.

sists of a purely electrostatic part, the charging energy  $E_C$ , plus the energy spacing between two discrete quantum levels,  $\Delta E$ .  $\Delta E$  is zero when two consecutive electrons are added to the same spin-degenerate level. The charging energy  $E_C = e^2/2C$ , where  $C$  is the sum of all capacitances to the SET-island<sup>1</sup>.

If we only consider first-order processes, energy conservation needs to be satisfied for transport to occur. The electrochemical potential  $\mu_N$  is the energy required for

adding the  $N$ th electron to the island. Electrons can only tunnel through the SET when  $\mu_N$  falls within the bias window (Figure 2(b)), i.e. when  $\mu_S \geq \mu_N \geq \mu_D$ . Here  $\mu_S$  and  $\mu_D$  are the electrochemical potential of the source and the drain respectively. Current cannot flow without an available level in the bias window, and the device is in Coulomb blockade, see Fig. 2(a). A gate voltage can shift the whole ladder of electrochemical potential levels up or down, and thus switch the device from Coulomb blockade to single-electron tunneling mode. By sweeping the gate voltage and measuring the conductance, one obtains Coulomb peaks as shown in Fig. 3(a).

Usually, one measures the conductance versus source-drain voltage  $V_{SD}$  and gate voltage  $V_G$  in a bias spectroscopy, see Figure 3(b). Inside the diamond-shaped

<sup>1</sup> We refer to other review articles on quantum dots and single-electron transistors for more background and details: Beenakker and van Houten (1991); Grabert *et al.* (1993); Hanson *et al.* (2007); Kouwenhoven *et al.* (2001, 1997a); Reimann and Manninen (2002); and Van der Wiel *et al.* (2003)

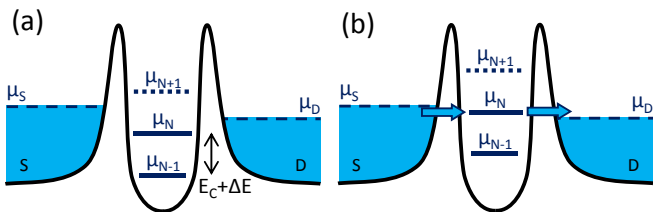


FIG. 2 **Schematic diagrams of the electrochemical potential of a single-electron transistor.** (a) There is no available level in the bias window between  $\mu_S$  and  $\mu_D$ , so the electron number is fixed at  $N$  due to Coulomb blockade. (b) The  $\mu_N$  level aligns with source and drain electrochemical potentials, and the number of electrons alternates between  $N$  and  $N - 1$ , resulting in a single-electron tunneling current.

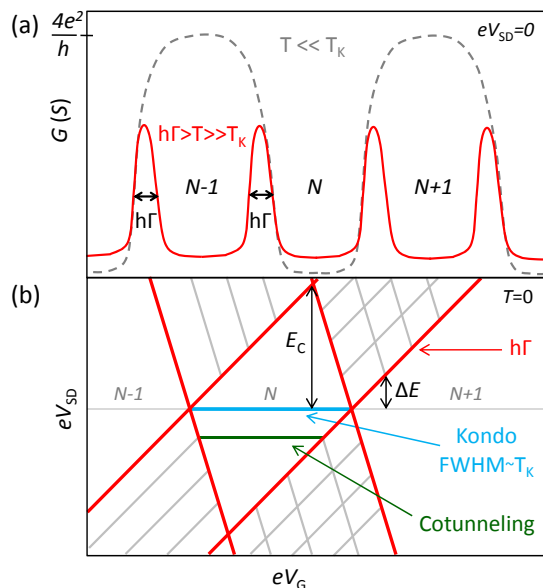


FIG. 3 **Zero-bias and finite-bias spectroscopy.** (a) Zero-bias conductance of transport both at  $T \gg T_K$  (solid line) and  $T \ll T_K$  (dashed line). In the first regime, the full width at half maximum (FWHM) of the Coulomb peaks corresponds to the level broadening  $h\Gamma$ . In the Kondo regime ( $T \ll T_K$ ), Coulomb blockade is overcome by coherent second-order tunneling processes (see main text). From Lansbergen, 2010. (b) Stability diagram showing Coulomb diamonds in differential conductance,  $dI/dV_{SD}$ , versus  $eV_{SD}$  and  $eV_G$  at  $T = 0K$ . The edges of the diamond-shaped regions (red) correspond to the onset of current. Diagonal lines of increased conductance emanating from the diamonds (gray) indicate transport through excited states. The indicated internal energy scales  $E_C$ ,  $\Delta E$ ,  $h\Gamma$  and  $T_K$  define the boundaries between different transport regimes, see main text.

regions, the current is blocked and the number of electrons is constant. At the edges of these Coulomb diamonds a level is resonant with either source or drain and single-electron tunneling occurs. When an excited state enters the bias window as well, this can result in a line of increased conductance parallel to the diamond edges. From such a bias spectroscopy one can read off

the excited-states and the charging energy directly, as indicated in Figure 3(b).

The simple model described above explains successfully how quantization of charge and energy leads to effects like Coulomb blockade and Coulomb oscillations. Nevertheless, it is too simplified in many respects. Up until now we only worried about the electronic properties of the localized state but not about the physics of the electron transport through that state. In this section, based on Lansbergen, 2010, we will describe the five different regimes of electron transport through a localized state in a three-terminal-geometry. How electrons traverse a quantum device is strongly dependent on the coherence during the tunneling process and thus depends strongly on  $eV_{SD}$  and  $k_B T$ . These external energy scales should be compared to the internal energy scales of the tunneling geometry that determine the transport regime, namely the charging energy  $E_C$ , the level spacing  $\Delta E$ , the level broadening  $h\Gamma$  and the Kondo temperature  $T_K$ . Here,  $\Gamma$  is the total tunnel rate to the localized state which can be separated into the tunnel coupling to the source electrode  $\Gamma_S$  and to the drain electrode  $\Gamma_D$ , i.e.  $\Gamma = \Gamma_S + \Gamma_D$ . The internal energy scales are all fixed by the confinement potential and the external environment, namely the temperature  $T$  and the applied bias  $V_{SD}$ .

A great deal of literature exists which describes the electronic transport in all possible proportionalities of these energy scales with each other (Alhassid, 2000; Beenakker, 1991; Buttiker, 1988). In most cases the internal energy scales are typically related to each other by  $T_K \ll h\Gamma \ll \Delta E \ll E_C$ , and occasionally by  $T_K \ll \Delta E < h\Gamma \ll E_C$ , limiting the number of separate transport regimes we need to consider. Fig. 4(a) is a schematic depiction of transport regimes as a function of  $eV_{SD}$  and  $k_B T$ . It should be noted that the boundaries between transport regimes are typically not abrupt transitions. For clarity, internal and external energy scales (except  $T_K$  and  $h\Gamma$ ) are indicated in a schematic representation of our geometry, see Fig. 4(b).

Here, we will not make a distinction between the external energy scales  $k_B T$  and  $eV_{SD}$  when we compare them to internal energy scales, as indicated by Fig. 4(a). The reason behind this equality is that both these external energy scales have a very similar effect on the transport characteristics. Their only relevant effect is that they introduce (hot) phonons to the crystal lattice, either directly by temperature or by inelastic tunneling processes induced by the non-equilibrium Fermi energies of the source/drain contacts.

Next, we will describe the five separate tunneling regimes and their corresponding expressions for the source/drain current  $I$  shortly. These regimes are the so-called multi-electron regime, the sequential multi-level regime, the sequential single level regime, the coherent regime and the Kondo regime, see Fig. 4(a).

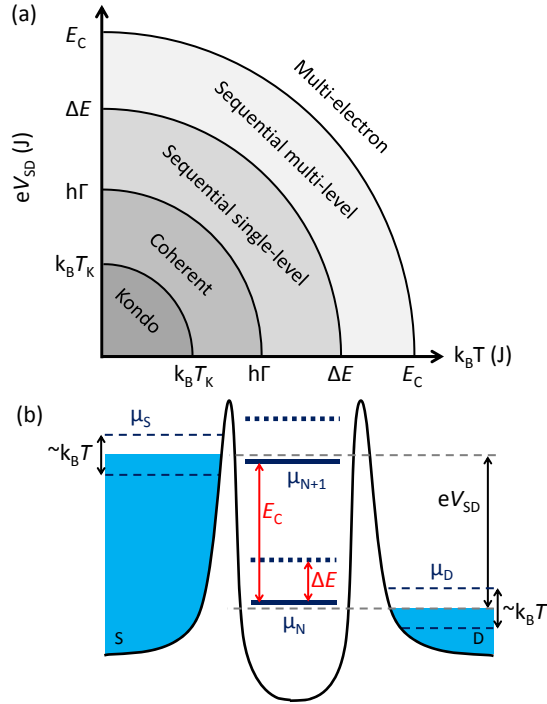


FIG. 4 Depiction of the five separate transport regimes in a three terminal quantum device. (a) Schematic depiction of the regimes in which transport through a localized takes place as a function of the external energy scales  $k_B T$  and  $V_{SD}$ . The transitions between regimes take place on the order of the internal energy scales  $E_C$ ,  $\Delta E$ ,  $h\Gamma$  and  $T_K$  (b) Potential landscape of the three terminal geometry, where the quantum states and the electrochemical potential of the leads are shown together with  $k_B T$ ,  $V_{SD}$  and  $E_C$ ,  $\Delta E$ .

### 1. The multi-electron regime

Firstly there is the multi-electron regime ( $E_C \ll k_B T, eV_{SD}$ ) where Coulomb blockade does not occur, as mentioned in the start of this chapter. This regime is not relevant for this review.

### 2. The sequential multi-level regime

At  $\Delta E \ll k_B T, eV_{SD} \ll E_C$  the system is in the sequential multi-level regime. The transport is given by (Beenakker, 1991; Van der Vaart *et al.*, 1993)

$$I = e \frac{(\Gamma_{in}^1 + \Gamma_{in}^2 + \dots + \Gamma_{in}^n) \Gamma_{out}^1}{\Gamma_{in}^1 + \Gamma_{in}^2 + \dots + \Gamma_{in}^n + \Gamma_{out}^1}, \quad (1)$$

where the subscript denotes the direction of transport, into- or out of the localized state, and the superscript indicates the level, where 1 refers to the ground state and  $n$  indicates the highest orbital within the energy window set by  $eV_{SD}$ . The current thus depends on the ingoing rates of all levels in the bias window and the outgoing rate

of *only* the ground state. Physically, electrons can enter any orbital state which they are energetically allowed to. Once a single electron is transferred to the localized state, Coulomb blockade prevents another electron from entering. The  $(N + 1)$  bound electron will relax back to the ground state before it has a chance to tunnel out of the localized state, since the orbital relaxation times ( $\sim 1$  ps) are much faster than the outgoing tunnel rates ( $\sim 1$  ns) in these structures. The inelastic nature of the relaxation prohibits any coherent transfer of electrons from the source to the drain electrode.

### 3. The sequential single-level regime

The next transport regime is the sequential single-level regime, roughly bounded by  $h\Gamma \ll k_B T, eV_{SD} \ll \Delta E$ , where only a single level resides inside the bias window. This regime is a transition between phase-coherent and phase-incoherent transport between source- and drain-electrodes and the tunneling current depends vitally on  $k_B T$ . For  $V_{SD} = 0$  the conductance is given by (Beenakker, 1991)

$$G = \frac{e^2}{4k_B T} \frac{\Gamma_{in}^1 \Gamma_{out}^1}{\Gamma_{in}^1 + \Gamma_{out}^1}, \quad (2)$$

where  $\Gamma_{in}$  is the tunnel rate into the localized state and  $\Gamma_{out}$  is the tunnel rate out. Note that  $\Gamma_{in} = \Gamma_S, \Gamma_{out} = \Gamma_D$  for  $V_{SD} > 0$  and  $\Gamma_{in} = \Gamma_D, \Gamma_{out} = \Gamma_S$  for  $V_{SD} < 0$ .

If the localized state is strongly coupled to the contacts higher-order transport processes become apparent in the Coulomb blocked region, *i.e.* the so called cotunneling lines indicated in Fig. 3(b). This is the case when  $E_C/\Gamma$  approaches unity in the open regime. There is an elastic and inelastic component to the cotunneling (Averin and Nazarov, 1990; Nazarov and Blanter, 2009). The inelastic component leads to a constant background current in the Coulomb diamond. The inelastic component leads to a step in the current when the applied bias exceeds  $\Delta E$ . The current is given by

$$I_{el} = \frac{\rho^2 e^2}{8\pi^2 h} \Gamma_{in} \Gamma_{out} \frac{1}{\Delta E}, \quad (3)$$

$$I_{in} = \frac{\rho^2 e^2}{6h} \Gamma_{in} \Gamma_{out} \left( \frac{k_B T}{E_e} + \frac{k_B T}{E_h} \right), \quad (4)$$

for the elastic and inelastic cotunneling respectively with  $E_e + E_h = E_C$ , where the energies  $E_e$  and  $E_h$  denote the distance to the Fermi energy of the filled and empty state. The complex co-tunneling line shape is discussed in depth in Wegewijs and Nazarov, 2001.

### 4. The coherent regime

As soon as the external energy scales are much smaller than  $h\Gamma$  ( $T_K \ll k_B T, eV_{SD} \ll h\Gamma \ll \Delta E$ ) the system is

in the coherent regime, where the conductance is given by Buttiker (1988)

$$G = \frac{e^2}{h} \frac{\Gamma_{\text{in}}^1 \Gamma_{\text{out}}^1}{(\Gamma_{\text{in}}^1 + \Gamma_{\text{out}}^1)^2} \quad (5)$$

The conductance is thus given by the quantum conductance  $e^2/h$  multiplied by a factor that only depends on the symmetry between  $\Gamma_S$  and  $\Gamma_D$ . It has been proven explicitly that this expression, easily derived for resonances in 1D double barrier structures (Ricco and Azbel, 1984), also holds in three dimensions (Kalmeyer and Laughlin, 1987).

### 5. The Kondo regime

The final transport regime occurs when  $eV_{SD}, k_B T \ll T_K$ . The Kondo temperature is the energy scale below which second-order charge transitions start to play a role in the transport (Meir and Wingreen, 1993). Up to now, the discussion of transport in single dopant- or quantum dot -structures has considered first-order transitions, where the transferred electrons make a direct transition from their initial to their final state. It should be noted that the constant interaction model only considers first-order charge transitions (Kouwenhoven *et al.*, 1997a). In a second-order transition, the transferred electron goes from the initial to the final state via a virtual state of the atom or dot. A virtual state is an electronic state whose wave function does not commute with the Hamiltonian of the system and therefore has a finite lifetime. The lifetime of the virtual state is related to the Heisenberg uncertainty principle, as the electron can only reside on the virtual state on a timescale  $t \sim \hbar / (\mu_N - \mu_{S,D})$ , where  $\mu_N - \mu_{S,D}$  is the energy difference between the virtual state and the nearest real state. The main characteristic of this transport regime is a zero-bias resonance inside the Coulomb diamond for  $N$ =odd, as we will explain next, see also Fig. 3(a) and (b).

When  $N$  = even, the total localized spin is zero due to the (typical) even-odd filling of the (spin) states, resulting in zero localized magnetic moment. When  $N$  = odd, one electron is unpaired, giving the localized state a net magnetic moment. In contrast to metals doped with magnetic impurities, the conductance of double barrier structures actually *increases* due the Kondo effect. This is because the density of states in the channel at a  $\mu_S, \mu_D$  (associated with the newly formed Kondo singlet state) acts as a transport channel for electrons, as if it were a “regular” localized state in the channel. The Kondo temperature can be expressed as (Glazman and Pustilnik, 2003)

$$T_K = \sqrt{E_C \Gamma} \exp\left(-\pi \frac{\mu_N - \mu_{S,D}}{2\Gamma}\right) \quad (6)$$

assuming  $\mu_N - \mu_{S,D} \ll \mu_{N-1} - \mu_{S,D}$ . The zero-bias Kondo resonance is furthermore characterized by its temperature and magnetic field dependence. The conductance of the Kondo resonance has a logarithmic temperature dependence, which is described by the phenomenological relationship (Goldhaber-Gordon *et al.*, 1998)

$$G(T) = (G)_0 \left( \frac{T_K'^2}{T^2 + T_K'^2} \right)^s \quad (7)$$

where  $T_K' = T_K / \sqrt{2^{1/s} - 1}$ ,  $G_0$  is the zero-temperature Kondo conductance and  $s$  is a constant found to be equal to 0.22 (Goldhaber-Gordon *et al.*, 1998).

## III. PHYSICS OF SI NANOSTRUCTURES

Here we describe the fundamental physical properties of Si nanostructures. Some of these arise from the electron confinement into a small region (tens of nanometers or less) and are similar to those of other semiconductors, but other properties are present only in Si. One example arises because Si has multiple degenerate valleys in its conduction band, described in the first section. The valleys play an important role in both dopant and quantum dot devices, although the details of the valley physics in those two systems are different. Moreover, in heterostructures, strain often plays an important role, and the interplay between strain, disorder, and the properties of the valleys are important in determining the low-energy properties of the devices.

### A. Bulk silicon: valley degeneracy

Because silicon is used in many technical applications, methods for manufacturing extremely high purity samples are well-developed. Silicon has several stable nuclear isotopes, with  $^{28}\text{Si}$ , which has no nuclear spin, being the most abundant (its abundance in natural silicon is 92%). This availability of a spin-zero silicon isotope is useful for applications in which one wishes to preserve the coherence of electron spins, since the absence of hyperfine interaction eliminates a possible decoherence channel for the electron spin, see section VI.A.4.

The properties of electrons in silicon have been studied in great detail for many decades (Cohen and Chelikowsky, 1988; Yu and Cardona, 2001). Here we review aspects of the material that will prove critical in understanding the challenges that arise as one works to create devices with desired properties on the nanoscale. One such aspect is how the effects of multiple valleys present in the conduction band in bulk silicon appear in specific silicon nanodevices. The manifestations of valley physics in quantum dots are different from those in dopant-based devices, and understanding the relevant effects is critical



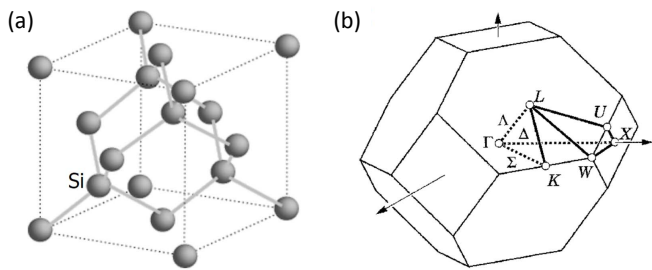


FIG. 5 **Silicon crystal in real and reciprocal space.** (a) 3D plot of the unit cell of the bulk silicon crystal in real space, showing the diamond or Face-Centered Cubic lattice, which has cubic symmetry. (b) Silicon crystal in reciprocal space. Brillouin zone of the silicon crystal lattice. It is the Wigner-Seitz cell of the Body-Centered Cubic lattice.  $\Gamma$  is the center of the polyhedron.

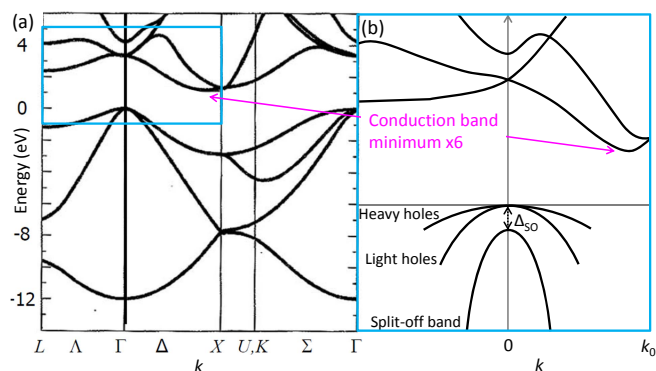


FIG. 6 **Band structure of bulk silicon.** (a) The conduction band has six degenerate minima or valleys at  $0.85k_0$ . Figure from Davies (1998). (b) Zoom-in on the bottom of the conduction band and the top of the valence band (schematic, not exact). The bandgap in bulk Si is 1.12 eV at room temperature, increasing to 1.17 eV at 4 K (Green, 1990). The heavy and light hole bands are degenerate for  $k = 0$ . The split-off band is separated from the other subbands by the spin-orbit splitting  $\Delta_{so}$  of 44 meV.

for manipulating the spin degrees of freedom of the electrons in nanodevices. In the following subsections, we first define and discuss the conduction band valleys in bulk silicon, and then the behavior and consequences of valley physics for quantum dots and for dopant devices.

Crystalline silicon is a covalently bonded crystal with a diamond lattice structure, as shown in Fig. 5. The band structure of bulk silicon (Phillips, 1962), shown in Fig. 6, has the property that the energies of electron states in the conduction band is not minimized when the crystal momentum  $k = 0$ , but rather at a nonzero value,  $k_0$ , that is 85% of the way to the Brillouin zone boundary, as shown in Fig. 6(b). Because bulk silicon has cubic symmetry, there are six equivalent minima. Thus we say that bulk silicon has six degenerate valleys in its conduction band.

In conventional electronic devices, the presence of mul-

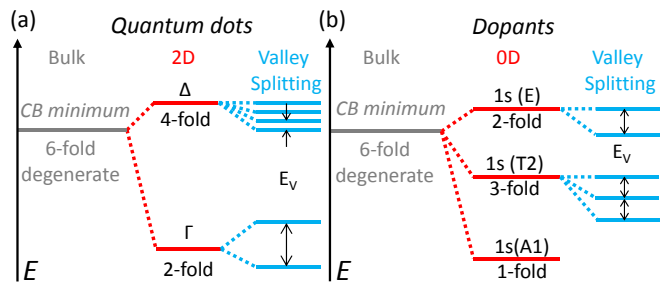


FIG. 7 **Valley splitting of dopants and of quantum dots in silicon quantum wells.** (a) For a quantum well, in which a thin silicon layer is sandwiched between two layers of  $\text{Si}_x\text{Ge}_{1-x}$ , with  $x$  typically  $\sim 0.25 - 0.3$ , the six-fold valley degeneracy of bulk silicon is broken by the large in-plane tensile strain in the quantum well so that two  $\Gamma$ -levels are about 200 meV below the four  $\Delta$ -levels (Schäffler *et al.*, 1992). The remaining two-fold degeneracy is broken by the confinement in the quantum well and by electric fields, with the resulting valley splitting typically  $\sim 0.1 - 1$  meV. (b) For phosphorus dopants, strong central-cell corrections near the dopant break the six-fold valley degeneracy of bulk silicon so that the lowest-energy valley state is non-degenerate (except for spin degeneracy), lowered by an energy 11.7 meV. The degeneracies of higher-energy levels are broken by lattice strain and by electric fields.

tiply valleys typically does not affect transport properties in a profound way. However, valley physics plays a critical role in quantum electronics because of interference between different valleys that arises when the electronic transport is fundamentally quantum. For example, the presence of an additional valley greatly complicates spin manipulation because it can lift Pauli spin blockade, which is fundamental for many strategies for spin manipulation in quantum dot nanodevices (Hüttel *et al.*, 2003; Johnson *et al.*, 2005a; Koppens *et al.*, 2005; Ono *et al.*, 2002; Rokhinson *et al.*, 2001). In bulk silicon, the valleys are degenerate (the energies of the six states related by the cubic symmetry are the same), but in nanodevices this degeneracy can be and usually is broken by various effects that include strain, confinement, and electric fields. When valley degeneracy is lifted, at low temperatures the carriers populate only the lowest-energy valley state, thus eliminating some of the quantum effects that arise when the valleys are degenerate.

A summary of valley splitting in heterostructures and in dopant devices is presented in Fig. 7. For strained silicon quantum wells, the large in-plane strain lifts the energies of the in-plane ( $x$  and  $y$ ) valleys. The remaining two-fold degeneracy of the  $z$ -valleys is broken by electronic  $z$ -confinement induced by electric fields and by the quantum well itself, resulting in a valley splitting of order  $0.1 - 1$  meV. The breaking of the two-fold valley degeneracy is very sensitive to atomic-scale details of the interface, and is discussed in detail in Sec. III.B and Appendices A, B, and C.

For an electron bound to a dopant in silicon, the valley

degeneracy of bulk silicon is lifted because of the strong confinement potential from the dopant atom (Kohn and Luttinger, 1955a). For phosphorus donors in silicon, the electronic ground state is non-degenerate, with an energy gap of  $\sim 11.7$  meV between the non-degenerate ground state and the excited states (Andresen *et al.*, 2009; Ramdas and Rodriguez, 1981). Thus, additional degeneracy of the electronic ground state is not a concern in dopant devices. However, the fact that the conduction band minimum in silicon is at a large crystal momentum  $k_0$  that is near the zone boundary gives rise to other physical effects that are important for quantum electronic devices. One such consequence arises because the wave functions of the electronic states in dopants oscillate in space on the very short length scale  $\sim 2\pi/k_0$ , which is roughly on the scale of one nanometer. These charge oscillations differ from the electron charge variations due to Bloch oscillations because they can cause the exchange coupling to change sign, and thus have significant implications for the design of quantum electronic devices, as discussed in Section III.C.

## B. Quantum wells and dots

In the quantum well devices we discuss here, one starts with a material that has a two-dimensional electron gas (2DEG), and then creates the quantum dot by lithographically patterning top gates to which voltages are applied that deplete the 2DEG surrounding the dot. By carefully adjusting the gate voltages, one can achieve dots with occupancy of a single electron, see section IV.D. Moreover, the same gate voltages that are used to define the dot are also used to perform the manipulations required for initialization, gate operations, and readout of charge and spin states (Maune *et al.*, 2012), see section VI.C.4.

### 1. Valley splitting in quantum dots

Understanding the valley degrees of freedom is important for being able to make sure that the valley splitting is in a regime suitable for spin-based quantum computation. Even in the low-density limit appropriate to single-electron quantum dots, where electron-electron interactions (Ando *et al.*, 1982) are unimportant, valley splitting is complex: the breaking of the valley degeneracy involves physics on the atomic scale, many orders of magnitude smaller than the quantum dot itself, so it depends on the detailed properties of alloy and interface disorder that are unknown in a given experimental sample. Because the locations of the individual atoms in a given device are not known, statistical approaches to atomistic device modeling or averaging theories like effective mass must be utilized. Theory, modeling, and simulation provide

insight into the physical mechanisms giving rise to valley splitting, so that device design and fabrication methods can be developed to yield dots with valley splitting compatible with use in spin-based quantum information processing devices.

In bulk silicon, there are six degenerate conduction band minima in the Brillouin zone (valleys) as depicted in Figure 6. In a Si/SiGe heterostructure, the silicon quantum well is under large tensile strain, and the six-fold degeneracy is broken into a two-fold one (Schäffler, 1997). Similarly, confinement of electrons in the  $z$ -direction in a 2-dimensional electron gas lifts the remaining two-fold valley degeneracy, resulting in four  $\Delta$ -valleys with a heavy effective mass parallel to the interface have an energy several tens of meV higher than the two  $\Gamma$ -valleys (Ando *et al.*, 1982), as shown in Fig. 7. The sharp and flat interface produces a potential step in the  $z$ -direction and can lift the degeneracy of the  $\Gamma$ -valleys in two levels separated by the valley splitting  $E_V$ . Theoretical predictions for the valley splitting of flat interfaces are generally on the order of 0.1–0.3 meV (Boykin *et al.*, 2004c; Culcer *et al.*, 2010a; Ohkawa and Uemura, 1977b; Saraiva *et al.*, 2010). Experimental values in Si inversion layers mostly vary from 0.3–1.2 meV, but some are substantially smaller (Koester *et al.*, 1997; Köhler and Roos, 1979; Lai *et al.*, 2006; Nicholas *et al.*, 1980; Pudalov *et al.*, 1985; Weitz *et al.*, 1996). A giant valley splitting of 23 meV measured in a similar structure (Takashina *et al.*, 2006) is still not completely understood theoretically (Saraiva *et al.*, 2010).

The two main approaches for understanding valley splitting in silicon heterostructures are tight-binding calculations (Boykin *et al.*, 2007b, 2004a, 2005; Kharche *et al.*, 2007; Srinivasan *et al.*, 2008) and theories that use an effective mass formalism (Friesen *et al.*, 2007; Friesen and Coppersmith, 2010; Saraiva *et al.*, 2009). Appendix A reviews a simple one-dimensional tight-binding model (Boykin *et al.*, 2004c) that exhibits a true valley degeneracy in the limit of finite size, and illustrates some of the physical mechanisms that lead the breaking of the valley degeneracy and hence the emergence of valley splitting. A pictorial sketch of the two lowest-energy eigenstates of this one-dimensional model is presented in Fig. 8. The eigenfunctions have very similar envelopes and fast oscillations with period very close to  $2\pi/k_0$ , where  $k_0$  is the wavevector of the valley minimum. The different alignments of the phases of the fast oscillations with sharp interfaces cause the energies of the two states to be different, thus giving rise to valley splitting.

Valley splitting has complicated dependence on environmental and structural conditions. Large-scale atomistic tight-binding calculations can incorporate realistic inhomogeneity in the atomic arrangement, both in terms of alloy disorder and in terms of disorder in the locations of interface steps, as discussed in Appendix C. Important conclusions from these studies include:

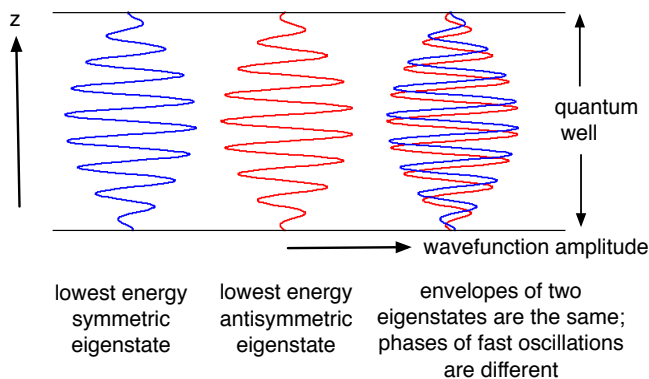


FIG. 8 Sketch of the two lowest energy eigenstates of the two-band model presented in Appendix A in an infinite square well. The envelopes of the two eigenfunctions are very similar to each other and to the sine behavior obtained in the absence of valley degeneracy; the effects of the valley degeneracy give rise to fast oscillations within this envelope. For a square well, one eigenfunction is symmetric and the other is antisymmetric; the symmetries are different because the fast oscillations have different phases, as measured from the quantum well boundaries. This sensitive dependence of valley splitting on the atomic-scale physics near the well boundary is the source of the sensitive dependence of the valley splitting on disorder at the quantum well interfaces.

1. The Si band structure is complex with 6 conduction band valleys that are not independent but coupled within a single Hamiltonian. 6 valleys in bulk are degenerate, however several mechanisms can cause modifications to the Hamiltonian which will break the degeneracy of the 6 valleys.
2. Biaxial tensile strain raises the energies of 4 valleys from the remaining 2 valleys. One modern strategy for fabricating Si devices for quantum electronics applications is to use a bi-axially strained thin film of Si grown on a pseudomorphic  $\text{Si}_x\text{Ge}_{1-x}$  substrate.
3. Built-in or externally applied electric fields break the symmetry of the Hamiltonian and can couple the various valleys and thus lift the valley degeneracy.
4. Interfaces break the translationally symmetry of the system Hamiltonian and couple valleys. The strength of the valley interaction and the resulting valley splitting depends on the atomistic details of the symmetry breaking interface. Detailed phase information at the interface on the length of atomic distances regulate the valley splitting.
5. Technically well controlled interfaces in Si are buffers of either  $\text{SiO}_2$  or  $\text{Si}_x\text{Ge}_{1-x}$ , which are intrinsically atomistically disordered. Some of the effects

of this disorder can be understood qualitatively using effective mass theory, but because of the importance of atomic-scale physics in determining valley splitting, atom-scale theory is required for quantitative understanding.

6. For  $\text{Si}_x\text{Ge}_{1-x}$ , there are 3 critical disorder effects to consider: atom-type disorder, atom-position disorder, alloy concentration disorder. A detailed discussion of the characterization of the effects of these different types is presented in Appendix C.

Many of the features of the physics that give rise to valley splitting can be understood qualitatively and even semi-quantitatively using effective mass theories (Kohn and Luttinger, 1955b; Seitz and Turnbull, 1957), if these theories are formulated carefully to incorporate the microscopic effects that give rise to valley splitting (Friesen, 2005; Friesen *et al.*, 2007; Fritzsche, 1962; Nestoklon *et al.*, 2006; Pantelides, 1978). In the envelope function or effective mass formalism, the theory is written in terms of an envelope function for the wave function, which is well-suited for describing variations on relatively long scales (such as the quantum dot confinement), while the effects of the degenerate valleys are incorporated using a valley coupling parameter that is treated as a delta function whose strength is determined by the atomic scale physics (Chutia *et al.*, 2008; Friesen *et al.*, 2007; Saraiva *et al.*, 2009). The envelope function formalism has the advantage that one can obtain analytic results for valley splitting in nontrivial geometries (Culcer *et al.*, 2010a,b; Friesen *et al.*, 2007; Friesen and Coppersmith, 2010). However, the theory must explicitly incorporate information from the atomic scale, either as a valley coupling parameter that is fit to tight-binding results, as the output of a multiscale approach (Chutia *et al.*, 2008; Saraiva *et al.*, 2009), or by explicit atomistic calculation on large scales, as embodied by the NEMO tool suite (Boykin *et al.*, 2004c; Klimeck *et al.*, 2007, 2002; Steiger *et al.*, 2011). More details of effective mass theory treatment of valley splitting are presented in Appendix B.

## 2. Mixing of valleys and orbits

When the valley splitting  $E_V$  is much greater than the orbital level spacing  $\Delta E$ , electrons will occupy single-particle levels with orbital numbers 1, 2, 3, ... and valley number  $V1$ , the lowest valley state (see Fig. 9(a)). Conversely, if  $\Delta E \gg E_V$  the first four electrons will occupy the valleys  $V1$  and  $V2$  in the lowest orbit before going to the next orbit with  $n = 2$ , as shown in Fig. 9(b). However, valleys and orbits can also hybridize (Friesen and Coppersmith, 2010), making it inappropriate to define distinct orbital and valley quantum numbers (see Fig. 9(c)). Depending on the degree of mixing, the valley-orbit levels  $VO1$ ,  $VO2$  etc, behave mostly like

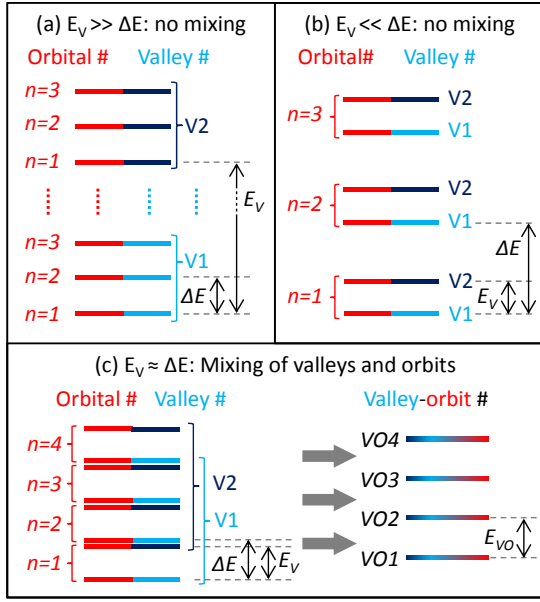


FIG. 9 **Valley-orbit mixing.** (a,b) If the valley splitting  $E_V$  and orbital level spacing  $\Delta E$  have very different values, the orbital and valley quantum numbers are well-defined and there will be no mixing of orbital and valley-like behavior. (c) When  $E_V \approx \Delta E$  the valleys and orbits can hybridize into single-particle levels separated by the valley-orbit splitting  $E_{VO}$ .

valleys or like orbits. Instead of referring to a pure valley splitting  $E_V$  the term valley-orbit splitting is used,  $E_{VO} = E_{VO2} - E_{VO1}$  for the difference in energy between the first two single-particle levels,  $E_{VO1}$  and  $E_{VO2}$ . This is referred to as the ground-state gap (Friesen and Coppersmith, 2010).

The behavior of the valley splitting in real quantum wells is complicated by the fact that in real devices the quantum well interface is not perfectly smooth and oriented perpendicular to  $\hat{z}$ . The energy difference between the two lowest eigenstates depends on the relationship between the phase of the fast oscillations of the wave function with the heterostructure boundary, and a step in the interface alters this phase relationship. The lowest energy wave function minimizes the energy, and, as shown in Fig. 10, can cause the phase of the fast oscillations to become dependent on the transverse coordinates  $x$  and  $y$ . This coupling between the  $z$ -behavior and the  $x$ - $y$  behavior is called valley-orbit coupling.

As discussed in subsection III.B.1 above, in a silicon quantum well under tensile strain, there are two low-lying conduction band valleys at wavevectors  $+k_0\hat{z}$  and  $-k_0\hat{z}$ , whose energies are split by the effects of confinement potentials and electric fields perpendicular to  $z$ . In the limit of a perfectly smooth interface aligned perpendicular to  $\hat{z}$ , the valley splitting of a quantum well with typical width and doping is of order 0.1 meV, a magnitude that can be understood using the simple one-



FIG. 10 **Valley-orbit coupling from interface steps.** *Top:* gray-scale visualization of wave function oscillations in the presence of a perfectly smooth interface, oriented perpendicular to  $\hat{z}$ . *Middle:* The relationship between the phase of the wave function oscillations and the interface is different on the two sides of an interface step. When the steps are close together, the phase does not adjust to the individual steps, and the valley splitting is suppressed. *Bottom:* When steps are far enough apart, the oscillations line up with the interface location on both sides of the steps, which causes the phase of the oscillations to depend on the transverse coordinate. This coupling between the behavior of the wave function in the  $z$  direction and in the  $x - y$  plane, which arises even when the well is atomically thin, is known as valley-orbit coupling.

dimensional model presented in Appendix A.

If the step density of the quantum well interface is reasonably high, then the transverse oscillations of the charge density cannot align with the entire interface, and valley splitting is greatly suppressed (Ando, 1979; Friesen *et al.*, 2007, 2006). The physical picture that emerges from effective mass theory that incorporates valley-orbit coupling is that the envelope function for the wave function in a silicon heterostructure is qualitatively similar to typical wave functions in quantum dots, but that there are also fast oscillations with wave vector  $\sim k_0$  in the  $z$ -direction. The fast oscillations of the two valley states have different phases. In the presence of interfacial disorder such as interfacial steps, the value of the valley phase that minimizes the energy becomes position-dependent, so that one fixed value of the phase cannot minimize the energy everywhere, and the energy difference between the two different valley states decreases. This suppression explains measurements of valley splitting performed in Hall bars (Khrapai *et al.*, 2003; Koester *et al.*, 1997; Lai *et al.*, 2004; Weitz *et al.*, 1996) that yield very small values for the valley splitting of only  $\mu\text{eV}$ , and also why singlet-triplet splittings in dots with two electrons have been observed with both positive and negative values at non-zero magnetic field (Borselli *et al.*, 2011a) — if the electron wave function straddles a step, then the val-

ley splitting is small, which, together with the effects of electron-electron interactions, causes the triplet state to have lower energy than the singlet state. If an electron is confined to a region small enough that it does not extend over multiple steps, then the valley splitting is not affected by the steps. Over the past several years, measurements of valley splitting in quantum point contacts (Goswami *et al.*, 2007) and of singlet-triplet splittings in quantum dots (Borselli *et al.*, 2011a,b; Simmons *et al.*, 2011; Thalakulam *et al.*, 2011) in Si/SiGe heterostructures demonstrate that these splittings can be relatively large, of order 1 meV, when the electrons are highly confined. These splittings are large enough that valley excitations are frozen out at the relevant temperatures for quantum devices ( $\sim 100$  mK).

There are two different manifestations of valley-orbit coupling. The first, illustrated in the bottom panel of Fig. 10, occurs when the phase of the valley oscillations depends on the transverse coordinate. The second type of valley-orbit coupling can be visualized by considering an interface with a nonuniform step density. A wave function localized in a region with few steps has larger valley splitting and hence lower energy than a wave function localized in a region with many steps (Shi *et al.*, 2011). Therefore, the presence of the valley degree of freedom leads to translation of the wave function in the  $x - y$  plane. Valley-orbit coupling is important when the scale of the variations of the orbital and valley contributions to the energy are similar, a situation that occurs frequently in few-electron quantum dot devices.

Because valley-orbit coupling and valley splitting depend on interface details, the observation of valley splittings that vary substantially between devices (Borselli *et al.*, 2011b) is not unexpected. Understanding and controlling this variability is important for being able to scale up the technology and for the development of devices that exploit the valley degree of freedom (Culcer *et al.*, 2009a, 2012; Li *et al.*, 2010; Shi *et al.*, 2012). Therefore, improved understanding of the physical mechanisms that affect valley splitting in real devices remains an important topic of active research.

## C. Dopants in Si

### 1. Wave function engineering of single dopant electron states

The central theme of quantum electronics applications using single dopants is the ability to modify the dopant electron wave function using external electric fields and/or to manipulate the spin degrees of freedom using magnetic fields. In many proposals for dopant based qubits using either electron or nuclear spins as the qubit states, dopant electron wave function engineering is critical to effect single and two qubit gates. Since most work has been done on n-type dopants, this section will

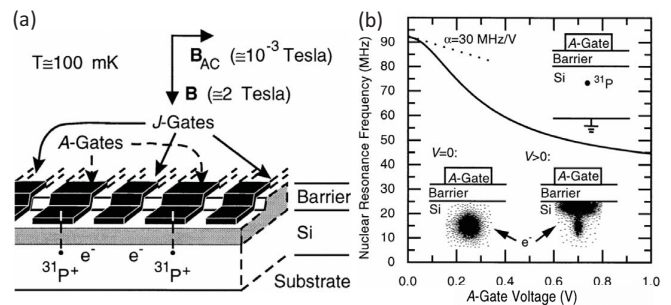


FIG. 11 **A silicon-based nuclear spin quantum computer** (a) Schematic of Kane's proposal for a scalable quantum computer in silicon using a linear array of  $^{31}\text{P}$  donors in a silicon host.  $J$ -gates and  $A$ -gates control respectively the exchange interaction  $J$  and the wave function, as shown in (b). Reproduced from Kane (1998).

focus on donors. The original idea comes from the Kane proposal for a nuclear-spin based quantum computer in silicon (Kane, 2000) where the single qubit operations are implemented by tuning the contact hyperfine interaction to bring the donor electron into resonance with a transverse oscillating magnetic driving field (see Fig. 11). To see this we write the effective spin qubit Hamiltonian of a single donor nucleus-electron system in the presence of a gate potential with strength  $V$  at the donor position as (Goan, 2005; Kane, 1998)

$$H_{1Q} = \mu_B B_z \sigma_e^z - g_n \mu_n B_z \sigma_n^z + A(V_A) \vec{\sigma}_n \cdot \vec{\sigma}_e, \quad (8)$$

where  $\mu_B$  is the Bohr magneton,  $g_n$  the Landé factor for  $^{31}\text{P}$ , and  $\mu_n$  is the nuclear magneton. The contact hyperfine interaction strength can be tuned by distorting the electron wave function through  $V_A$  using an  $A$ -gate electrode located above the qubit:

$$A(V_A) = \frac{2}{3} |\psi(0, V_A)|^2 \mu_B g_n \mu_n \mu_0, \quad (9)$$

where  $\mu_0$  is the permeability of silicon and  $\psi(0, V_A)$  is the donor electron wave-function evaluated at the nucleus under the “ $A$ -gate” potential  $V_A$ .

The change in the strength of the contact-hyperfine coupling due to the application of gate biases has been studied by several authors since Kane's proposal. To determine the change in the contact hyperfine coupling strength due to the application of a potential, it is necessary to calculate the shift in the donor electron wave function at the position of the donor nucleus. Depending on the applied bias polarity, an  $A$ -gate control electrode will either draw the wave function toward the gate, or push it away. In either scenario the wave function is perturbed to some extent, altering the contact hyperfine coupling depending critically on device parameters such as the bias applied and the depth of the donor from the interface. The level of sophistication of the treatment of the donor electron has steadily improved since

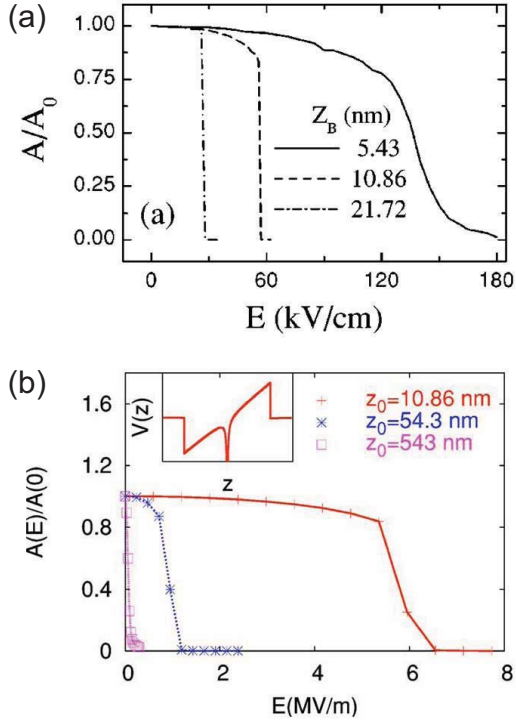


FIG. 12 **Relative Stark shift of the contact hyperfine interaction for different donor depths ( $z$ ) calculated for a uniform field in the  $z$  direction.** (a) Using the tight-binding approach (Martins *et al.*, 2004), and (b) Direct diagonalization in momentum space (Wellard and Hollenberg, 2005). Agreement in overall trends is reasonable, and for the  $z = 10.86$  nm case both methods predict ionization at  $\sim 6$  MV/m.

the original calculations following Kane (1998). The earliest approaches used fairly simple hydrogenic wave functions scaled by the dielectric constant of silicon. Larionov *et al.* (2000) treated the bias potential analytically, the gate electrode was modeled both as an infinite conducting strip, and as a small circular pad. The shift in the hyperfine interaction constant as a function of applied bias voltage was calculated using perturbation theory. Wellard *et al.* (2002), again using scaled hydrogenic orbitals treated the problem using a more realistic potential. They used a commercial semi-conductor software package, with built in Poisson solver, to calculate the electric potential produced inside a silicon substrate due to the application of a bias voltage to a control electrode. The wave function was expanded in a large basis of hydrogenic orbitals, with the Hamiltonian matrix being both constructed and diagonalized numerically. Kettle *et al.* (2003) extended these calculations using a basis of non-isotropic scaled hydrogenic orbital states. Smit *et al.* (2003, 2004) used group theory over the valley manifold and perturbation theory to describe the Stark shift of the donor electron while Martins *et al.* (2005, 2004) applied tight-binding theory to obtain the first description of the Stark shift of orbital states and the hyperfine interaction

including Bloch structure details. Meanwhile, the effective mass treatment was further developed in a combined variational approach (Friesen, 2005) and (Calderón *et al.*, 2009), and in (Debernardi *et al.*, 2006) using a Gaussian expansion of the effective-mass theory (EMT, see Appendix B) envelope functions. This was followed by the application of direct diagonalization in momentum space (Wellard and Hollenberg, 2005) allowing the potential due to the  $A$ -gate to be included at the Hamiltonian level and gave a similar picture of the Stark shift of the hyperfine interaction as a function of external field strength and donor depth as the earlier tight-binding treatment of Martins *et al.* (2004) (see Fig. 12). Although not optimized computationally, the momentum space diagonalization approach has served as a consistency check against larger scale real-space tight-binding calculations of the Stark shift of the donor hyperfine interaction at low fields (Rahman *et al.*, 2007) in the overall benchmarking against experiment (Bradbury *et al.*, 2006) which shows the theoretical description of has converged to a reasonable level in terms of internal consistency and comparison with experiment (see Fig. 13). It should be noted that in such descriptions encompassing the overall donor electron wave function it is the relative change in the contact hyperfine interaction as a function of electric field that is computed since these approaches do not describe well the details of the electron state at the nucleus. Absolute calculations of the contact hyperfine interaction are the domain of ab-initio theories where they have had remarkable success despite the truncation of the long range part of the donor potential (Gerstmann, 2011; Overhof and Gerstmann, 2004).

In more recent years, the effect of depth and proximity to the interface on donor orbital states (Calderón *et al.*, 2008, 2006b; Hao *et al.*, 2009; Rahman *et al.*, 2009a) has received more attention as key experimental measurements became available. A turning point was the measurement of donor orbital states through transport in FinFET devices which showed significant deviation from the expected bulk spectrum (see section V.C). Extensive tight-binding calculations were used to explore the space of electric field and donor depth on the quantum confinement conditions of the donor-associated electron, providing an excellent description of the low lying donor states observed and even allowing a determination of the donor species (Lansbergen *et al.*, 2008). It would appear that the theoretical description of electric field “wave function engineering” of the donor electron across device dimensions is now well understood. The context of the Kane donor qubit has spurred further refinements of the theoretical description of donor states, including the site-specific contact and non-isotropic hyperfine interaction terms (Ivey and Mieher, 1975a,b) for wave function mapping under electric fields (Park *et al.*, 2009), interaction with magnetic fields and gate control of the  $g$ -factor (Rahman *et al.*, 2009b; Thilderkvist

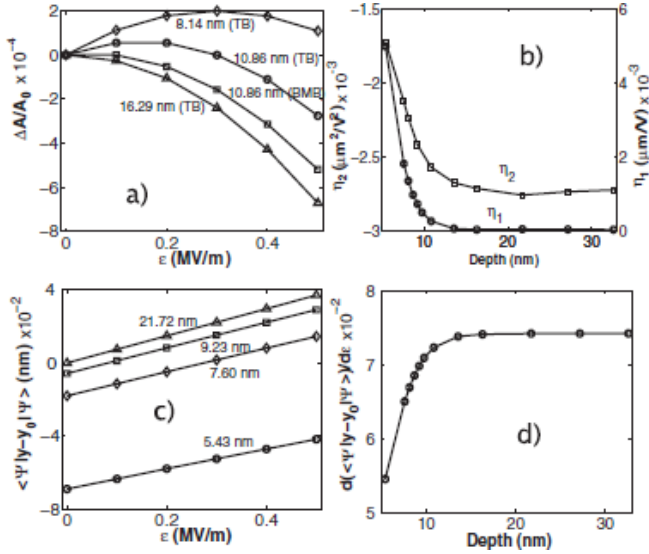


FIG. 13 Low field Stark shift of the hyperfine interaction for momentum space diagonalization (BMB) and tight-binding (TB) methods. (a) Electric field response of hyperfine coupling at various donor depths (BMB and TB). (b) Quadratic (lefthand axis) and linear (right-hand axis) Stark coefficients as a function of donor depth (TB). (c) Shift of the ground state electron distribution (dipole moment) as a function of the electric field (TB). (d) The electric field gradient of the dipole moments as a function of donor depth (TB).

*et al.*, 1994), dynamics of molecular donor-based systems (Hollenberg *et al.*, 2004; Hu *et al.*, 2005; Rahman *et al.*, 2011b; Wellard *et al.*, 2006), cross-talk in hyperfine control (Kandasamy *et al.*, 2006), coherent single electron transport through chains of ionized donor chains (Rahman *et al.*, 2009b), spin-to-charge readout mechanisms (Fang *et al.*, 2002; Hollenberg *et al.*, 2004), and the calculation of donor levels in the presence of STM-fabricated nanostructures providing modifications to the overall potential in a single-atom transistor, as shown in section V.B.3 (Fuechsle *et al.*, 2010).

## 2. Two-donor systems and exchange coupling

In the quantum computing context, the two main approaches to directly couple the spins of donor electrons are through the Coulomb-based exchange interaction between proximate donor electrons, or the magnetic dipole interaction. The Kane model uses gate control of the exchange interaction as per the two-qubit effective spin Hamiltonian:

$$\begin{aligned}
 H_{2Q} = & \mu_B B_z \sigma_{e_1}^z - g_n \mu_n B_z \sigma_{n_1}^z + A_1 (V_{A1}) \vec{\sigma}_{n_1} \cdot \vec{\sigma}_{e_1} \\
 & + \mu_B B_z \sigma_{e_2}^z - g_n \mu_n B_z \sigma_{n_2}^z + A_2 (V_{A2}) \vec{\sigma}_{n_2} \cdot \sigma_{e_2} \\
 & + J(V_J) \vec{\sigma}_{e_1} \cdot \sigma_{e_2}.
 \end{aligned}
 \tag{10}$$

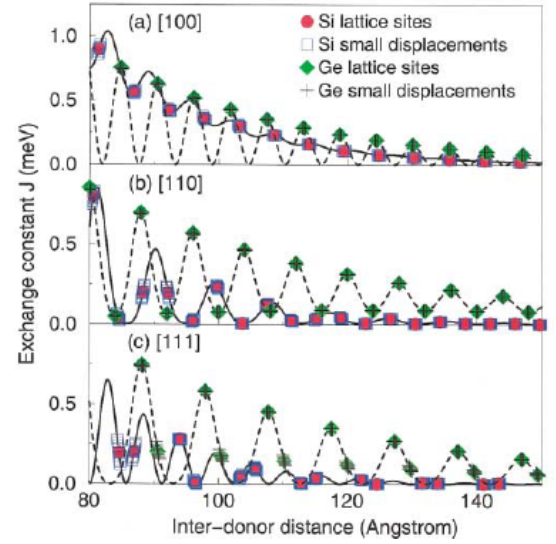


FIG. 14 **J-oscillations in the exchange coupling.** Calculated exchange coupling between two phosphorus donors in Si (solid lines) and Ge (dashed lines) along high-symmetry directions for the diamond structure. Values appropriate for impurities at substitutional sites are given by the circles (Si) and diamonds (Ge). Off-lattice displacements by 10% of the nearest-neighbor distance lead to the perturbed values indicated by the squares (Si) and crosses (Ge). Reproduced from Koiller *et al.* (2002a).

In this equation we apply equation 8 on two dopants and add the exchange-coupling  $J$  between the dopants. There have been a number of papers investigating the construction and fidelity of two-qubit gates (e.g. such as the controlled-NOT) from this Hamiltonian (Fang *et al.*, 2005; Fowler *et al.*, 2003; Hill and Goan, 2003, 2004; Kerridge *et al.*, 2006; Tsai *et al.*, 2009; Tsai and Goan, 2008). From a microscopic physics viewpoint, in general the exchange energy  $J$  is stronger than the dipole interaction for smaller separations, however it decays roughly as (Herring and Flicker, 1964)

$$J(R) \sim (R/a^*) \exp(-2R/a^*), \tag{11}$$

where  $R$  is the donor separation and  $a^*$  is the effective Bohr radius of the electron wave function. The strength of the dipole coupling  $D$  on the other hand is much weaker for small separations, but is longer ranged, decaying as  $D(R) \sim R^{-3}$ . The result is that exchange coupling dominates for donors that are separated by less than approximately 20-30 nm.

However, the valley degeneracy of the silicon conduction band gives rise to a far more complicated dependence on the donor separation, than this for the exchange interaction as noted in the seminal work of Cullis and Marko (Cullis and Marko, 1970) and expanded upon in the Kane quantum computer (Koiller and Hu, 2005; Koiller *et al.*, 2002a, 2003) (see Fig. 14). The exchange integrals over Bloch states were carried out (Koiller *et al.*,

2004; Wellard *et al.*, 2003) For some time these “exchange oscillations” were seen as a fundamental limitation of donor based quantum computing as it was thought that to achieve a given exchange coupling the donors would have to be placed in the lattice with lattice site precision (Koiller *et al.*, 2002a), although Koiller *et al.* (2002b) found that strain could be used to lift the valley degeneracy and alleviate the problem to some extent. In these treatments the exchange coupling is calculated in the Heitler-London approximation (Calderón *et al.*, 2006a; Koiller *et al.*, 2004) using effective mass wave functions containing a single Bloch component from each valley minimum, hence it is perhaps not surprising that the overlap integral results in an oscillatory behavior in the donor separation at the level of the lattice constant. When the exchange integral is computed using the more accurate BMB wave function including many such Bloch states to reproduce the donor levels the lattice constant “interference” effect is somewhat averaged out (Wellard and Hollenberg, 2005) over the background Herring-Flicker dependence in equation 11 (see Fig. 16). Nonetheless, the issue remains that in fabricating donor devices there will be some level of imprecision in the donor atom placement, however, using STM fabrication these errors might be constrained to the single lattice site level.

In any case, all components of a quantum computer will need some form of characterization. For all donor qubit logic gates (single and two qubit), considerations of background noise sources and decoherence also need to be taken into account, e.g. see Fowler *et al.* (2003); Hill and Goan (2003); Saikin and Fedichkin (2003); Wellard and Hollenberg (2001, 2002) (the decoherence of donor electron spins is covered in Section VI). Robust control techniques have been developed specifically for the eventuality of some level of variation in the exchange coupling (Hill, 2007), which in conjunction with gate characterization protocols (Cole *et al.*, 2006; Devitt *et al.*, 2006) have the potential to produce high fidelity two qubit gates in the Kane scheme (Testolin *et al.*, 2005). Tsai *et al.* (2009) have applied control techniques to optimize the CNOT gate in the Kane scheme. A more serious impediment to employing the exchange interaction for quantum gates is the effect of charge noise (Hu and Das Sarma, 2006; Vorobjtov *et al.*, 2004). Because the exchange interaction is ultimately derived from an overlap of electronic wave functions, variations in the background potential such as from charge noise in the device can affect the exchange coupling significantly and can only be mitigated by optimizing the materials design (Kane, 2005).

The control of the exchange interaction  $J$  has also received considerable attention since the original Kane paper. Early calculations of the dependence of  $J$  on an external  $J$ -gate bias were carried out by Fang *et al.* (2002) using a Gaussian expansion (see Fig. 16). Subsequent calculations of the  $J$ -gate control in various ap-

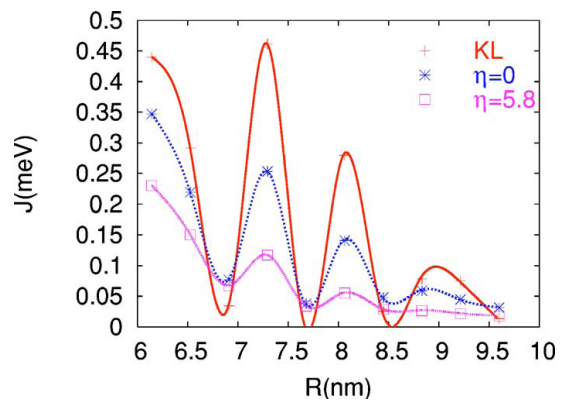


FIG. 15 **Smoothing out the exchange oscillations - the exchange coupling  $J$  as a function of donor separation along [110].** Red curve: Calculation using the effective-mass wave function. Blue: Calculation of  $J$  based on wave functions obtained using direct momentum diagonalization over a large basis of Bloch states (BMB) with no core-correction of the impurity potential ( $\eta = 0$ ). Pink curve: BMB calculation of  $J$  with a core-correction ( $\eta = 5.8$ ) that reproduces the donor ground-state and valley-splitting. Note that the points refer to substitutional sites in the silicon matrix. Although the donor separations are relatively small in this case, the spatial variation of the exchange interaction appears to be significantly damped compared to the effective mass treatment. All  $J$  values are calculated in the Heitler-London approximation. Reproduced from Wellard and Hollenberg (2005)

proaches describing the two-electron physics were carried out (Calderón *et al.*, 2007; Fang *et al.*, 2005; Kettle *et al.*, 2006, 2004; Wellard and Hollenberg, 2004) given further insight into the controllability of the exchange interaction. However, the gate modification of the overlap between electron states is a difficult calculation and most likely a full configuration interaction framework incorporating valley physics and Bloch structure is required to obtain quantitative results to compare with experiments once measurements are made. A related problem is the calculation of the two-electron donor state ( $D^-$ ), notoriously difficult in the case of a hydrogen ion in vacuum, but even more so when the non-trivial valley physics is added in to complicate such simple points of reference as Hund’s Rule. In the context of single donor quantum computing Fang *et al.* (2002) calculated the effect of electric fields on the  $D^-$  state, which was a key component of the spin-to-charge conversion read-out scheme of Kane. In Hollenberg *et al.* (2004) time-dependent calculations of the  $D^0 D^0 \rightarrow D^+ D^-$  transition were undertaken in a proposal for resonant based spin-to-charge conversion. More recent calculations have focussed on the complication of valley physics in the  $D^-$  bound states particularly under electric fields (Calderón *et al.*, 2010a; Rahman *et al.*, 2011a), with some notable success in comparisons with recent experimental measurements (Fuechsle *et al.*, 2010; Lansbergen *et al.*, 2008).



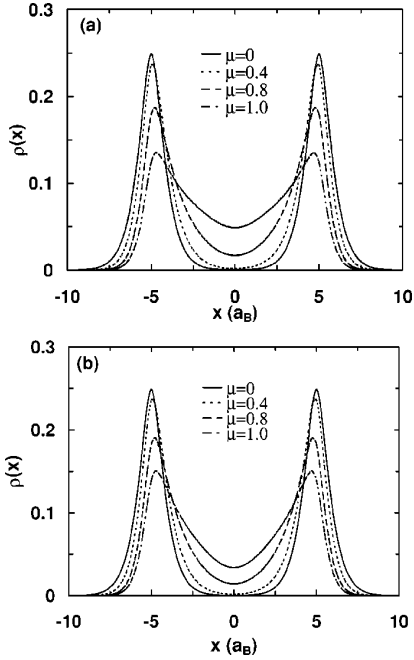


FIG. 16 **Gate control of the two-donor system.** Averaged charge distribution along the interdonor axis for various strengths of the  $J$ -gate potential ( $\mu$ ) for the singlet (a) and triplet (b) states (fixed donor separation at  $10 a_B$ ). Reproduced from Fang *et al.* (2002).

### 3. Planar donor structures: delta-doped layers and nanowires

The atom-by-atom fabrication of monolayer donor structures using STM techniques represents the state-of-the-art in precision silicon devices (see section V.B.3). From a theoretical point of view these structures present new challenges in order to describe not just their inherent physics (band structure, Fermi level, electronic extent, valley splitting, effect of disorder etc), but their use as in-plane gates in quantum electronic devices, including quantum computing. In understanding the physics of these highly doped monolayer systems *ab-initio* techniques have been used to good effect. Paradoxically, *ab-initio* techniques whilst being severely limited to relatively small numbers of atoms can handle planar systems with a high degree of symmetry, exploiting periodic boundary conditions of the supercell in the plane of the structure with sufficient silicon “cladding” vertically for convergence. The earliest calculations in this context were by Qian *et al.* (2005) for the infinite 2D planar (“delta-doped”) ordered layer using a Wannier-based Density Functional Theory (DFT) approach (see Fig. 17(a)). Carter *et al.* (2009) carried out an extensive DFT calculation of the same Si:P structures using a somewhat restrictive single zeta polarized basis providing a comprehensive picture of the band structure, effective potential, Fermi energy and electronic width as a function of planar doping density, finding converged re-

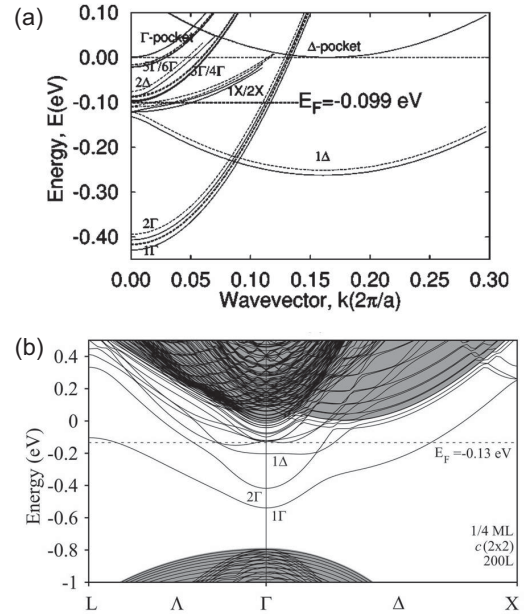


FIG. 17 **Band structure of the 1/4 monolayer phosphorus  $\delta$ -doped layer** Top: (a) The calculation by Qian *et al.* (2005): the solid lines show the band structure without exchange-correlation and short-range effects, while the dotted lines show the band structure obtained in the full model. (b) The DFT calculation in a supercell with 200 cladding layers by Carter *et al.* (2009). The plane projected bulk band structure of Si is represented by the gray continuum. The Fermi level is indicated by a horizontal dashed line. Reproduced from Carter *et al.* (2009) and Qian *et al.* (2005).

sults for cladding above 80 layers (see Fig. 17(b)). More recently the effect of disorder on the physics of the delta-doped layer has been investigated both in a modified pseudo-DFT approach (Carter *et al.*, 2011), and in a self-consistent tight-binding approach which can handle much larger supercell sizes and hence more accurately represent instances of disorder (Lee *et al.*, 2011). These calculations indicate that the valley splitting of the sub-Fermi bands is quite sensitive to the degree of disorder and will play an important role in eventual device applications.

The question of convergence between methodologies still remains on important quantities such as valley splitting. Drumm *et al.* (2012) have applied distinct DFT approaches based on localized and de-localized basis sets to calculate the properties of delta-doped layers. They obtain convergence in the description of the valley splitting and Fermi level only when the localized basis set is extended to the double zeta polarized level. The DFT calculations of the band structure have informed a self-consistent effective mass description of Si:P monolayer structures, which has been effective in describing states observed in a STM fabricated 7-donor planar quantum dot (Fuechsle *et al.*, 2010). The self-consistent tight-binding approach has also been employed beyond the

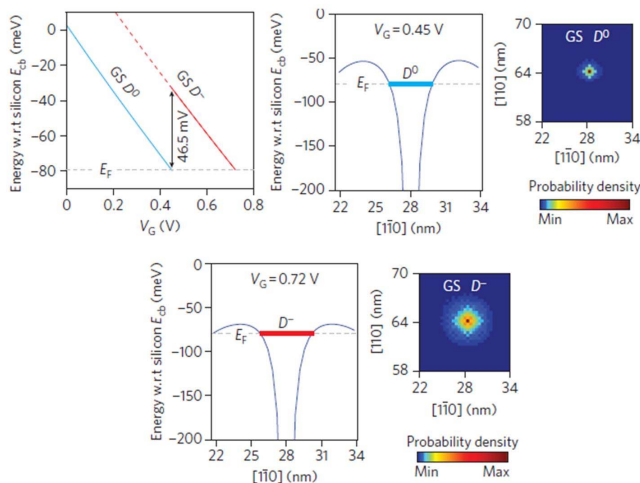


FIG. 18 **Calculated electronic spectrum of a single-atom transistor.** Top left: Calculated energies of the  $D^0$  and  $D^-$  ground states (GS) as a function of the applied gate voltage  $V_G$ . The difference in the energy of these two ground states gives a charging energy of  $E_C \approx 46.5$  meV, which is in excellent agreement with the measurement in this device. Potential profiles between source and drain electrodes calculated for  $V_G = 0.45$  V (top middle) and  $0.72$  V (bottom left). The calculated orbital probability density of the ground state for the  $D^0$  potential (top right) is more localized around the donor than for the  $D^-$  potential (bottom right), which is screened by the bound electron. Reproduced from Fuechsle *et al.* (2011).

delta-doped layer to describe recent STM fabricated devices. In Weber *et al.* (2012) the electronic structure of Si:P monolayer wires only four atoms wide was calculated and gave results in terms of the number of conduction modes in good agreement with experiment. The most ambitious calculation to date was a simulation of the single-atom transistor (Fuechsle *et al.*, 2011) where the same self-consistent tight-binding approach was used to determine the effective potential due to planar gates at the channel-donor site and subsequently coupled with a tight-binding description of the donor electronic levels. The agreement of the calculated  $D^0$  and  $D^-$  charge transitions with the measurements was indeed remarkable given the complexity of the system and is a strong indication that the theoretical description of donor based quantum electronic devices is well in hand.

#### IV. QUANTUM DOTS IN SI AND SIGE

Quantum dots showing Coulomb blockade and displaying single-electron physics can be created in Si and SiGe in many different ways. In this section we first briefly review the early work aimed at the demonstration of Coulomb charging effects in Si and SiGe. An emphasis in this work was the quest to see Coulomb effects

at as high a temperature as possible. We then discuss modern approaches to quantum dot fabrication. The application of charge sensing methods is shown to enable a wide range of experiments, including calibration of the absolute electron number, spin-state spectroscopy, and the measurement of spin filling as a function of electron number. We close this section with a discussion of both transport and charge sensing measurements in silicon-based double quantum dots.

#### A. Early work: Coulomb blockade in silicon

In this section we discuss early experiments studying Coulomb blockade in Si devices. Additional background and details can be found in Ahmed (1997); Likharev (1999); Meirav and Foxman (1996); Ono *et al.* (2005); Takahashi *et al.* (2002); and Tilke *et al.* (2001).

Experiments exploring intentional Coulomb blockade and transport through Si/SiO<sub>2</sub> and Si/SiGe quantum dots dates to the early 1990s, shortly after the discovery of Coulomb blockade (Field *et al.*, 1990; Fulton and Dolan, 1987; Meirav *et al.*, 1990; Scott-Thomas *et al.*, 1989). The primary requirements for the observation of Coulomb blockade are to isolate a small island while maintaining a weak but nonzero tunnel coupling to the leads. The addition of one or more gates to control the charge on the dot is essential for more complicated experiments.

Coulomb blockade was achieved very early in structures formed by etching delta-doped SiGe or doped silicon-on-insulator (SOI) structures (Ali and Ahmed, 1994; Paul *et al.*, 1993). Ali and Ahmed (1994) made use of two separate lithography and etching steps to modulate the thickness of a patterned silicon-on-insulator layer, resulting in a weakly coupled island between two leads. Coulomb blockade, which was observed in measurements of current versus source-drain voltage that showed a Coulomb gap, persisted up to  $T = 3.8$  K. The Coulomb gap could be modulated by an integrated side gate. In this type of highly-doped SOI structure, current in the doped leads was three-dimensional, as the mean free path was smaller than the lead thickness.

Silicon nanowires formed in SOI can be transformed into a quantum dot by pattern-dependent oxidation (PA-DOX), a process that makes use of the dependence of oxidation in silicon on the exposed surface area and strain (Takahashi *et al.*, 1994, 1995). One of the features of this process is that very small quantum dots can be formed, enabling measurement of Coulomb oscillations at high temperatures, with a demonstration of some modulation persisting to room temperature as early as 1994 (Takahashi *et al.*, 1994). Fujiwara and co-workers studied the few-electron regime in similar devices using photoexcitation techniques (Fujiwara *et al.*, 1997). Electron beam lithography can be used to help control the

shape of small silicon dots that show Coulomb effects at temperature above 100 K (Leobandung *et al.*, 1995). Very narrow triangular cross-section wires also can be formed by anisotropic etching on SIMOX, resulting in Coulomb effects at room temperature from disorder-induced dots along the length of each wire (Ishikuro *et al.*, 1996).

Coulomb blockade can in fact be observed in devices that are similar to production FETs, provided a small island of electrons can be isolated in the device. Isolation of such an island of electrons can be accomplished by the use of a gate that does not overlap the source and drain, leading to Coulomb blockade in CMOS devices (Boeuf *et al.*, 2003). This approach has culminated very recently in a single-electron transistor operating at room temperature (Shin *et al.*, 2010).

In 1994 Matsuoka and co-workers proposed using “two-story gates” to create single-electron devices (Matsuoka *et al.*, 1994). As shown in Fig. 19, a single gate was used to form an inversion layer for transport, and an upper gate was reverse-biased to generate barriers and define a quantum dot (Matsuoka and Kimura, 1995). While this structure has only a single gate to control the tunnel barriers and differs in significant ways from later work, it anticipates the use of two layers of gates that would be used more than a decade later for experiments on spin blockade, spin measurement, and spin manipulation (see Sections IV.F.2 and VI).

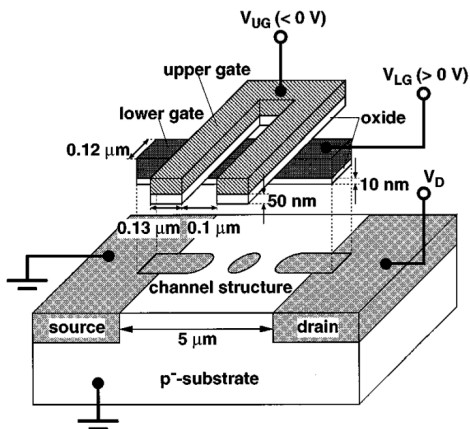


FIG. 19 **Two-story gated quantum dot** Figure from Matsuoka and Kimura (1995).

## B. Single quantum dots

This section assesses quantum dots formed different silicon nanostructures by presenting the experimental analogues of the quantum dot concepts explained in section II.A.

## 1. Self-assembled nanocrystals

The material dimensions of nanocrystals can easily be made as small as 10 nm, resulting in large and thus easily observable level splittings, even at room temperature (Otobe *et al.*, 1998). On the other hand, those dimensions make electron transport measurements cumbersome because the crystals are not easily connected to source and drain reservoirs. Self-assembled silicon nanocrystals with diameters varying from 3-12 nm have been grown by chemical vapor deposition techniques (Baron *et al.*, 2000; Steimle *et al.*, 2007). Coulomb oscillations have been observed by electrostatic trapping between Al source and drain electrodes (Dutta *et al.*, 2000). Zaknoon *et al.* (2008) showed charging energies of  $\sim 50$  meV using scanning tunneling spectroscopy. Twelve resonances in the conductance versus bias voltage were attributed to the twelve-fold conduction band degeneracy owing to spin and the six-fold valley degeneracy as described in section III.A.

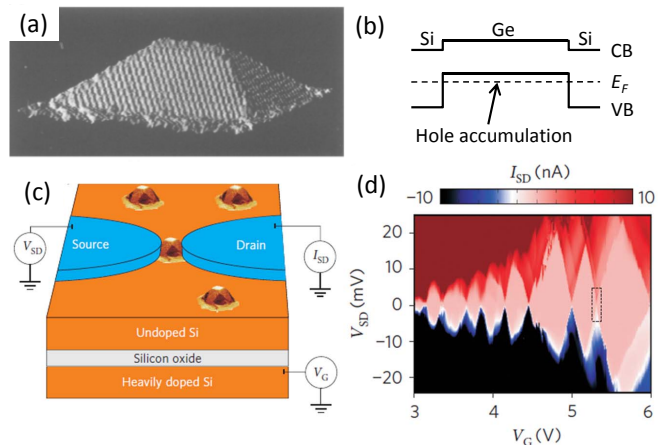


FIG. 20 **Self-assembled nanocrystals.** (a), STM image of a Ge/Si(001) cluster with a height of 2.8 nm. Scan area is  $40 \times 40$  nm, from (Mo *et al.*, 1990). (b), Band diagram for a Si/Ge/Si heterostructure, showing the accumulation of holes owing to the valence band offset between Ge and Si. (c), Schematic of a quantum-dot device obtained by contacting a single SiGe nanocrystal to aluminum source/drain electrodes. The heavily doped substrate is used as a back-gate for the measurements in (d) where  $I_{SD}$  is plotted as a function of  $V_G$  and  $V_{SD}$ . (c,d) from Katsaros *et al.* (2010).

Small Ge islands can be grown on Si(001) via Stranski-Krastanov growth resulting in huts, pyramids and domes with heights of 5-70 nm and lateral dimensions varying from 20-80 nm (Eaglesham and Cerullo, 1990; Katsaros *et al.*, 2008; Medeiros-Ribeiro *et al.*, 1998; Mo *et al.*, 1990; Ross *et al.*, 1999; Stangl *et al.*, 2004), see Fig. 20(a). The group of De Franceschi in Grenoble made Al contacts to Ge domes with an additional 2 nm Si capping layer (Katsaros *et al.*, 2011, 2010), see Fig. 20. In this configuration the SiGe nanocrystal acts

as a confining potential for holes due to the valence band offset between Ge and Si at the heterostructure interface (Schäffler, 1997; Van de Walle and Martin, 1986). Free holes will accumulate in the Ge when the Fermi level lies below the valence band edge of the Ge center, see Fig. 20(b). Electron transport measurements at 15 mK show Coulomb diamonds with charging energies varying from few to 20 meV as 8 holes leave the quantum dot. Due to the limited tunability reaching the few-charge regime in self-assembled nanocrystals will be a great challenge.

## 2. Bottom-up grown nanowires

Bottom-up grown nanowires are generally synthesized by means of a vapor-liquid-solid process (Wagner and Ellis, 1964), allowing for growth of single-crystal Si and Ge nanowires (Morales and Lieber, 1998) with diameters varying from 3-100 nm and lengths up to tens of microns, see Fig. 21(a,b). Both n-type and p-type dopants have been incorporated, and their location depends on the diameter (Xie *et al.*, 2009). The doping can be varied during growth: such modulation doping has been used to intersect heavily-doped n-Si regions with two short lightly-doped regions, resulting in single-electron tunneling at 1.5 K (Yang *et al.*, 2005). Within one nanowire heterostructures of different materials can be created both radially and axially, such as core/shell Ge/Si nanowires (Lauhon *et al.*, 2002). In the latter case the valence band offset will induce hole population in the Ge core, see Fig. 20(b).

When metallic contacts are made to nanowires the Schottky tunnel barriers can define the quantum dot length as shown in core/shell Ge/Si nanowires (Lu *et al.*, 2005) and Si nanowires (Zhong *et al.*, 2005), see Fig. 21(c). The Si nanowire quantum dot length can be shortened by silicidation transforming the device into e.g. a NiSi-Si-NiSi nanowire as shown in Fig. 21(d) (Mongillo *et al.*, 2011; Weber *et al.*, 2006; Zwanenburg *et al.*, 2009a).

After the demonstration of Coulomb blockade oscillations in Ge/Si nanowires by the Lieber group from Harvard (Lu *et al.*, 2005), they joined forces with the Marcus group and created double quantum dots with tuneable tunnel barriers, see Section IV.F. Here the source and drain contacts were ohmic, while the tunnel barrier were defined by local top gates (Hu *et al.*, 2007). Roddaro *et al.* (2008) used the same configuration to create single quantum dots and probe the hole spin states, see section IV.E. Recently, Ge/Si nanowires were predicted to have an unusually large spin-orbit interaction (Kloeffel *et al.*, 2011), making them particularly attractive candidates for quantum information processing via electric-dipole induce spin resonance (Golovach *et al.*, 2006; Nadj-

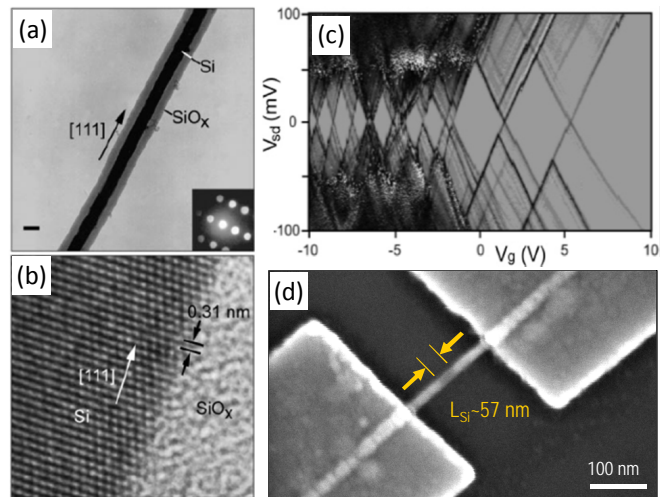


FIG. 21 **Bottom-up grown nanowires.** (a), TEM image of a Si nanowire; crystalline material (the Si core) appears darker than amorphous material ( $\text{SiO}_x$  sheath) in this imaging mode. Scale bar, 10 nm. (Inset) Convergent beam ED pattern recorded along the  $[211]$  zone axis perpendicular to the nanowire growth axis. (b) High-resolution TEM image of the crystalline Si core and amorphous  $\text{SiO}_x$  sheath. The (111) planes (black arrows) (spacing, 0.31 nm) are oriented perpendicular to the growth direction (white arrow). (a) and (b) from Morales and Lieber (1998). (c) Stability diagram of a p-Si nanowire quantum dot, from Zhong *et al.* (2005) (d) SEM image of a nanowire quantum dot with NiSi Schottky contacts, taken from Zwanenburg *et al.* (2009a).

Perge *et al.*, 2010; Nowack *et al.*, 2007), and for research on Majorana fermions (Majorana, 1937).

## 3. Electrostatically Gated Si/SiGe quantum dots

A powerful way to achieve tunability of tunnel couplings in quantum dots is to provide confinement in one or more directions through the use of electrostatic gates. Using Si/SiGe heterostructures or MOS structures, it is possible to form high-quality two-dimensional electron systems that can be partitioned into tunable quantum dots using depletion or accumulation gates, a procedure described in detail in this section and the next. In general, at least direction of confinement must be provided by a non-electrostatic method; usually a materials interface is used, the two most common being the interface between single-crystal silicon and its amorphous oxide (in MOS structures, see next section), and the epitaxial interface between single-crystal Si and  $\text{Si}_{1-x}\text{Ge}_x$ . When the precise composition  $x$  is unimportant and no confusion will arise, we refer to these heterostructures as Si/SiGe. Both MOS devices and Si/SiGe devices have been reviewed extensively: see, for example, (Sze and Ng, 1981; Wolf, 1990) for the former, and (Mooney, 1996; Schäffler, 1997) for the latter.

A convenient, if incomplete, figure of merit for two-dimensional electron systems is the mobility  $\mu$ . For Si MOS, mobilities in the range 5,000 – 15,000  $\text{cm}^2/\text{Vs}$  are quite good (see e.g. Eng *et al.* (2005, 2007)), and mobilities in excess of 40,000 have been reported (Kravchenko and Sarachik, 2004). The low-temperature mobility in Si/SiGe two-dimensional electron gases is not limited by defects at the interface and has been improving rapidly in recent years. In 1995, Ismail and coworkers reported a low-temperature mobility of 520,000  $\text{cm}^2/\text{Vs}$  in a modulation doped Si/SiGe heterostructure. Even higher mobility 800,000  $\text{cm}^2/\text{Vs}$  was reported by a group from Hitachi in 1998 (Sugii *et al.*, 1998). Very recently, Si/SiGe two-dimensional electron systems have been formed using undoped structures with a positively-biased accumulation gate. In this approach, an intervening oxide such as  $\text{Al}_2\text{O}_3$  (Lai *et al.*, 2005) is used to separate the accumulation gate from the semiconductor surface to avoid injecting current into the heterostructure (Lu *et al.*, 2007). The positively biased accumulation gate removes the need for any doping in the structure, removing a source of background impurities and eliminating the modulation doping layer altogether, both of which cause scattering. Resulting mobilities as high as  $\mu = 1.6 \times 10^6$   $\text{cm}^2/\text{Vs}$  have been reported (Lu *et al.*, 2009). Further, the removal of intentional doping appears to significantly reduce low-frequency charge noise in the devices.

Because both Si and Ge have isotopes with zero nuclear spin, the proposal by Loss and DiVincenzo to use quantum dots as hosts for semiconductor spin qubits (Loss and DiVincenzo, 1998) led to great interest in the development of high-quality quantum dots in Si/SiGe heterostructures (Friesen *et al.*, 2003; Vrijen *et al.*, 2000). The challenge in the early work in this field was to find ways to fabricate such dots with low-leakage gates, sufficient tunability, and in such a way as to yield stable, low-noise devices. As we discuss later in this review, modern Si/SiGe quantum dots have achieved performance that rivals that of any materials system available. In this section we discuss the materials and device research that enabled this advance.

Here we discuss a few critical materials issues relevant to Si/SiGe heterostructures. Interest in Si/SiGe arises because of the inevitability of defects at the interface between crystalline Si and its amorphous oxide. Heterostructures formed from Si and  $\text{Si}_{1-x}\text{Ge}_x$  offer a natural alternative with, in principle, no interfacial traps (although other types of disorder, such as atomic steps and strain variation are certainly present).

Although both Ge and Si have the diamond structure, Ge sits one row beneath Si in Group IV of the periodic table, so that the lattice constant of  $\text{Si}_{1-x}\text{Ge}_x$  increases as  $x$  increases, achieving a mismatch between pure Si and Ge of approximately 4.17% (Schäffler, 1997). Because of this mismatch, pure Ge will grow epitaxially only three monolayers on Si (REF). Beyond this critical thickness,

self-assembled quantum dots or “huts” form (Mo *et al.*, 1990), as discussed in Sec. IV.B.1, preventing the growth of uniform quantum wells.

Because the lattice constant of  $\text{Si}_{1-x}\text{Ge}_x$  depends on  $x$ , a full description of a heterostructure of these two materials must include the strain of the various layers. For the structures considered here, the layers of interest typically include a Si quantum well with  $\text{Si}_{1-x}\text{Ge}_x$  barriers on either side, as shown in Fig. 22; typically,  $x \sim 0.3$ . If the quantum well is below the critical thickness for dislocation formation, the in-plane lattice constant will remain unchanged passing vertically from the  $\text{Si}_{1-x}\text{Ge}_x$  through the Si quantum well and into the upper barrier. The band offsets at the Si/ $\text{Si}_{1-x}\text{Ge}_x$  interfaces depend on this in-plane lattice constant. For an unstrained, relaxed  $\text{Si}_{0.7}\text{Ge}_{0.3}$  barrier layer, the minimum in the conduction band is approximately 160 meV lower inside a Si quantum well compared with the barriers (Schäffler, 1997).

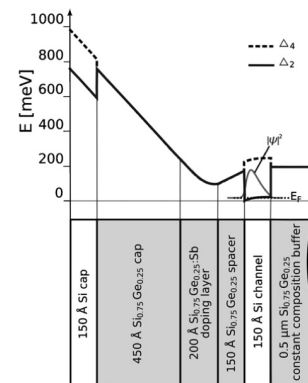


FIG. 22 **Layer design and corresponding band diagram of a Si/SiGe modulation doped heterostructure used to form top-gated quantum dots.** Figure reproduced from Berer *et al.* (2007).

Because it is very challenging to grow bulk, relaxed  $\text{Si}_{1-x}\text{Ge}_x$  with even moderately large  $x$ , relaxed  $\text{Si}_{1-x}\text{Ge}_x$  substrates conventionally are formed by slowly increasing the Ge concentration  $x$  from zero to the desired final value over a thickness of several microns. This procedure induces the formation of misfit dislocations, increasing the overall lattice constant, and can yield low-defect structures (Mooney, 1996).

Quantum dots in Si/SiGe demonstrating Coulomb blockade were first formed using a combination of etching and electrostatic gating. Notargiacomo *et al.* (2003) observed Coulomb blockade oscillations in a gated nanowire etched into a Si/SiGe heterostructure. This early device had a single overall top gate used to control the number of electrons in the quantum dot. Klein *et al.* (2004) formed a quantum dot with three separate electrostatic gates. These gates were formed of the same two-dimensional electron gas as the quantum dot, source and drain leads (Eriksson *et al.*, 2004). To avoid current

flowing from the gates to the dot, deep trenches were etched between the gates and the dots; the intervening gaps make it difficult to apply local fields and separately gate the quantum dot and the tunnel barriers. This drawback was partially ameliorated by the demonstration that gates could be formed by metal deposited into etched regions surrounding the dot (Sakr *et al.*, 2005), and by the use of extremely small top gates used to break an etched wire into a gated quantum dot (Slinker *et al.*, 2005). The drawback of etching, however, is the potentially large degree of side-wall depletion (Klein *et al.*, 2006).

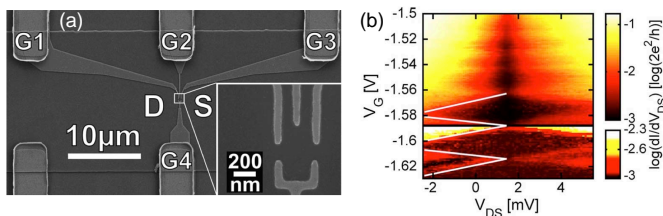


FIG. 23 (a) Scanning electron micrograph of the Schottky gates used to form a gated quantum dot in Si/SiGe. (b) Coulomb diamonds: conductance of the dot as a function of the voltage  $V_G$  applied to gates G1 and G2 and of the drain-source voltage  $V_{DS}$ . Figure from Berer *et al.* (2006).

Berer *et al.* (2006) demonstrated a fully top-gate defined quantum dot formed in a modulation-doped 2DEG. They showed that Pd Schottky gates, when fabricated on heterostructures like that shown in Fig. 22, in which care was taken to reduce the dopant density near the surface, enabled low-leakage gates (Berer *et al.*, 2006). There had been great concern about leakage between the top gates and the electron-gas, but the Pd Schottky gate approach has proven to be very robust (Klein *et al.*, 2007; Payette *et al.*, 2012; Wild *et al.*, 2010). The Schottky gate approach has also been used successfully to gate heterostructures with enhanced concentration of  $^{28}\text{Si}$  and  $^{70}\text{Ge}$  (Sailer *et al.*, 2009). A second approach to eliminating leakage is to use a dielectric material beneath the gates, creating metal-oxide-semiconductor split gates to define the quantum dot (Shin *et al.*, 2011).

The primary advantage of top-gated quantum dots, in which the lateral confinement is entirely provided by adjustable gate voltages, is their extreme tunability. At zero gate voltage in most cases current can flow directly under a gate, enabling a smooth transition from a completely open two-dimensional electron gas to a fully confined quantum dot. This tunability led both to the observation of the Kondo effect in a Si/SiGe top-gated quantum dot (Klein *et al.*, 2007) and the demonstration of single-electron occupation, as shown in Fig. 29 below.

#### 4. Quantum dots in planar MOS structures

The silicon MOSFET is arguably the world's most important electronic device, being the basic component of all modern microprocessor chips. Its success has been built on the ability to grow a high-quality  $\text{SiO}_2$  layer on the Si(001) surface by thermal oxidation, forming a high band-gap insulator that isolates the gate from the silicon channel. In current processor chips a  $\text{SiO}_2$  layer of  $\sim 1$  nm is sufficient to maintain gate voltages that are a significant fraction of a volt with negligible leakage. The Si/SiO<sub>2</sub> interface, which confines the electron layer in a MOSFET, can also have relatively low disorder, with reported electron mobilities as high as 40,000  $\text{cm}^2/\text{Vs}$  (Kravchenko and Sarachik, 2004), although the imperfect lattice match between the Si and SiO<sub>2</sub> creates defects at the interface, thus constraining the electron mobilities below those attainable at Si/SiGe interfaces. Despite this, it is possible to form quantum dots in MOS structures that can be controlled down to the single electron level with high tunability.

In this section we focus on quantum dots formed at the Si/SiO<sub>2</sub> interface via the use of multiple surface gates that provide electrostatic confinement in all three dimensions. In general an upper gate is used to induce an electron layer at the interface (as in a 'traditional' MOSFET), while two or more lower gates provide tunable tunnel barriers between the electron reservoirs and the dot. As already described in Section IV.A, one of the earliest such structures (Matsuoka *et al.*, 1994) exhibited Coulomb blockade oscillations, although these preliminary results were rather irregular.

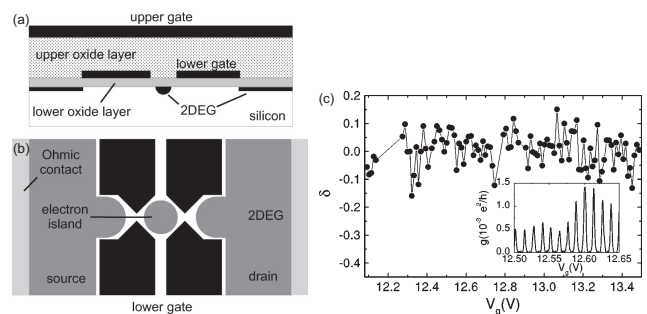


FIG. 24 **Si MOS quantum dot with large-area top gate.** (a) Cross-sectional schematic, showing two oxide and two gate layers, formed on a silicon substrate. The lower  $\text{SiO}_2$  layer is thermally grown, while the upper oxide layer is formed using plasma deposition. The large-area upper gate induces a 2DEG at the Si/SiO<sub>2</sub> interface, while the lower gates locally deplete the 2DEG to form a quantum dot. (b) Top-view schematic, showing lower depletion gates (black) and induced electron layer (grey). (c) Normalized spacings  $\delta$  between Coulomb peaks in dot conductance as a function of upper gate voltage. Inset: Raw Coulomb oscillations in dot conductance as a function of upper gate voltage. Data reproduced from Simmel *et al.* (1999)

One of the first well controlled MOS quantum dots was demonstrated by Simmel and co-workers (Simmel *et al.*, 1999), see Fig. 24. In this structure a continuous upper gate was used to induce a 2DEG over a large area, while four lower gates were used to confine the dot and form tunnel barriers. The resulting lower gate structure mimics those used to confine GaAs/AlGaAs quantum dots, although in the latter case the 2DEG is created by modulation doping. The resulting Coulomb oscillations in this MOS device were quite regular (Fig. 24c) and provided promise for future MOS quantum dot studies. The lower gates of the device in 24 were made using refractory metal, since a high-temperature process was used to deposit the upper oxide isolation layer (Fig. 24a).

This type of architecture, employing a large-area upper gate, has since been used by a number of groups to construct MOS quantum dots. A group at Sandia National Laboratory has demonstrated a range of quantum dot devices in which etched polycrystalline silicon (poly-Si) is used for the lower gates, and a large area upper metal gate is used to induce the 2DEG layer (Nordberg *et al.*, 2009a; Tracy *et al.*, 2010). The use of poly-Si gates is appealing from the perspective of future manufacturing, since it opens the way towards the use of CMOS process technologies. Similar MOS quantum dots also have been used to confine single electrons, enabling direct measurement of electron spin relaxation times (Xiao *et al.*, 2010a).

By reducing the upper MOSFET gate to nano-scale dimensions, a group at the University of New South Wales developed a highly compact multi-gate MOS architecture (Angus *et al.*, 2007) that has since been used to construct a wide range of single (Lim *et al.*, 2011, 2009b) and double (Lai *et al.*, 2011; Lim *et al.*, 2009a) quantum dot structures. This architecture uses aluminium (Al) upper and lower gates, with a thin (3-5 nm)  $\text{Al}_2\text{O}_3$  insulating layer between the gates, formed by thermally oxidizing the lower gates at the relatively low temperature of 150 C. Despite being very thin, the  $\text{Al}_2\text{O}_3$  insulator can maintain inter-gate voltage differentials of up to 4 volts, allowing for high gate tunability and the formation of very small (sub-50 nm) multi-dot structures. Figure 25 shows a quantum dot device based on this technology, in which a third layer of gate metal is used. This allows one upper gate to be used as a ‘plunger’, to control the dot’s electron occupancy, while separate upper gates are used to induce the source and drain electron reservoirs – see Fig. 25(b). In this way the dot occupancy can be reduced to the single electron level, as confirmed by the bias spectroscopy measurements in Fig. 25(c), while maintaining a high density of states in the reservoirs. Such independent tuning of the dot occupancy and the reservoir electron density is not possible when a large-area upper gate is employed.

The metal-oxide-semiconductor techniques just discussed can be applied to Si/SiGe heterostructures, yield-

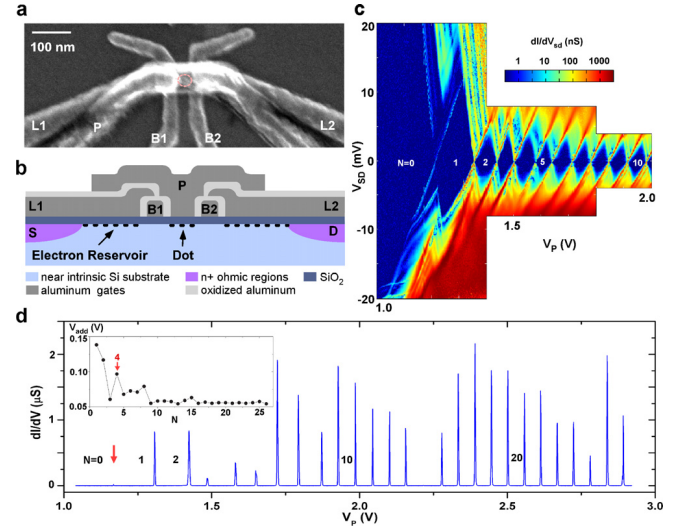


FIG. 25 **Si MOS quantum dot with compact multi-layer gate stack.** (a) Scanning electron microscope image of device. (b) Cross-sectional schematic, showing three oxide and three Al gate layers, formed on a silicon (light blue) substrate. The lower  $\text{SiO}_2$  layer (dark blue) is thermally grown in a high-temperature process, while the thin  $\text{Al}_2\text{O}_3$  layers between the gates are formed by low-temperature oxidation of the aluminium. (c) Stability map obtained by plotting differential current through the device as a function of source-drain bias  $V_{SD}$  and plunger (P) gate voltage  $V_P$ . The first diamond opens up completely, indicating that the dot has been fully depleted of electrons. (d) Coulomb oscillations as a function of plunger gate voltage  $V_P$  for the first 27 electrons in the dot. Data reproduced from Lim *et al.* (2011).

ing extremely stable and tunable quantum dots (Borselli *et al.*, 2011a; Hayes *et al.*, 2009). The device design, as shown in Fig. 26, uses a Si quantum well surrounded by epitaxial SiGe barriers to provide a clean environment for the electrons in the device. Those electrons are induced by an accumulation gate at the top of the structure. Depletion gates in between the accumulation gate and the heterostructure surface are used to control size and shape of the dot.

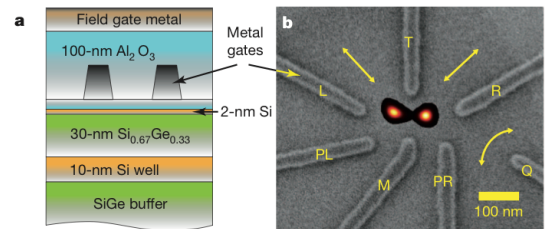


FIG. 26 **Gated quantum dot formed from a Si/SiGe heterostructure with a global accumulation gate.** (a) Cross-sectional view of the heterostructure and the two layers of gates. (b) Top-view SEM image of the gates with a numerical simulation of the electron density superimposed. Figure from Maune *et al.* (2012).

MOS-based quantum dots, using architectures like those in Figs. 24 and 25, have since been used in a range of advanced measurements, including single-spin measurement, and spin- and valley-state spectroscopy, as will be discussed in Sections IV.E and IV.F.

### 5. Quantum dots in etched silicon nanowires

As discussed in Section IV.A, some of the earliest silicon-based single-electron devices (e.g., Takahashi *et al.* (1994, 1995)) were based upon narrow nanowires, patterned using traditional top-down lithographic techniques, and etched from thin (typically  $< 50$  nm) silicon layers that form the upper layer of silicon-on-insulator (SOI) wafers. These early devices used the pattern-dependent oxidation (PADOX) technique to create additional confinement along the length of the nanowire, but in subsequent structures researchers have incorporated ‘wrap-around’ gates, positioned along the wire to provide additional confinement.

One of the first examples of this type of gated silicon nanowire was demonstrated by a group at NTT in Japan (Fujiwara *et al.*, 2006) – see Fig. 27. Here, confinement in the  $y$  and  $z$  directions was provided by the narrow wire, of width 20 nm and thickness 20 nm. Confinement along the wire was created by wrap-around lower gates, which in this case were made from poly-Si. Finally, a large-area poly-Si upper gate, isolated from the gates below using  $\text{SiO}_2$ , was patterned above the entire structure to induce carriers in the nominally un-doped nanowire. The resulting structure is entirely CMOS compatible, making it convenient for production using well established manufacturing processes, and also utilizing the high-quality thermally grown  $\text{SiO}_2$  insulator, which is known for having very low charge noise. In subsequent measurements on these devices it was found that they exhibited extremely high charge stability, with a drift of less than  $0.01e$  over several days (Zimmerman *et al.*, 2007).

As seen in Fig. 27(d), a quantum dot could be formed by using the outer gates LGS and LGD to create tunnel barriers, with the central gate LGC acting as a ‘plunger’ to control the dot occupancy. The Coulomb oscillations (Fig. 27d) were highly periodic over a large gate voltage range ( $-0.5V < V_{LGC} < 1.0V$ ), with a deviation of less than 1 percent, although the dot occupancy  $N_e$  in this case was relatively large, with  $N_e \sim 200$  electrons at  $V_{LGC} = 0V$ . The peak conductance could also be tuned over more than three orders of magnitude by varying the barrier gate voltages. For central gate voltages  $V_{LGC} < -1.0V$ , an additional tunnel barrier was formed, breaking the quantum dot into two dots in series. Using similar device structures this group could therefore operate double quantum dots, demonstrating effects such as Paul spin blockade (Liu *et al.*, 2008b) – discussed further in Section IV.F.2.

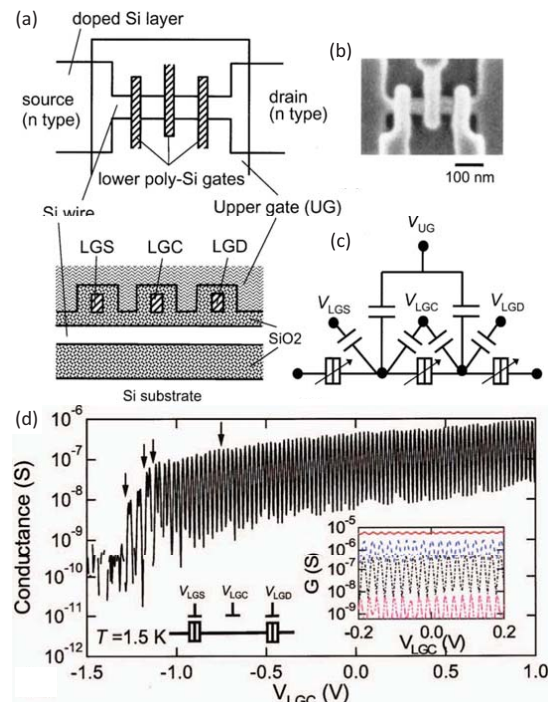


FIG. 27 **Multi-gated quantum dot in etched silicon nanowire.** (a) Schematic top-view and cross-sectional view of the device. Three lower ‘wrap-around’ gates (LGS, LGC, LGD) are used to form tunnel barriers in an etched silicon nanowire. (b) Top-view scanning electron microscope image of the device before the upper gate is deposited. (c) Equivalent circuit of the device. (d) Coulomb blockade oscillations in device conductance as a function of central gate voltage  $V_{LGC}$  when the two outer gates (LGS, LGD) are biased to set each tunnel barrier to  $G = 1 \mu\text{S}$ . Inset: Coulomb oscillations for a range of values of barrier conductance from 20 nS to 8  $\mu\text{S}$ . Data reproduced from Fujiwara *et al.* (2006)

It is also possible to form a quantum dot in a silicon nanowire using just a single gate, by making use of technology that has been developed for the manufacture of FinFET-type MOSFETs. FinFETs are considered likely replacements for planar CMOS technology, due to their ability to operate as FETs with good ON/OFF ratios at much shorter channel lengths. Figure 28(a,b) shows a FinFET structure, which is based upon a nanowire (the ‘fin’) that is etched from a SOI wafer, as previously described. A single wrap-around poly-Si gate is encapsulated on either side by an insulating ‘spacer’, made from either  $\text{SiO}_2$  or  $\text{Si}_3\text{N}_4$ . The gate and spacer act as a mask for subsequent ion implantation of the  $n+$  source and drain regions, which is a standard ‘self-aligned’ gate process used in CMOS production. By applying a positive voltage to the poly-Si gate electrons can be induced below, to form a quantum dot, isolated from the source and drain due to the natural barrier created by the spacer regions – see Fig. 28(b). Such quantum dots can be extremely stable in the many-electron



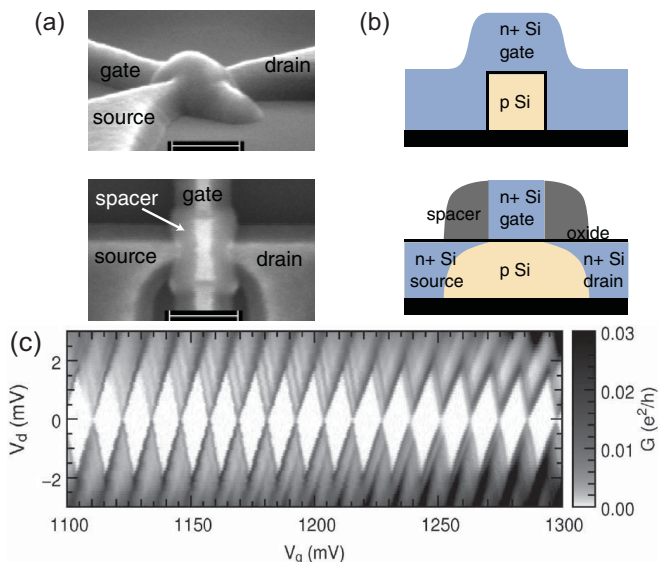


FIG. 28 **Single-gated quantum dot in etched silicon nanowire.** (a) SEM images and (b) cross-sectional schematics taken perpendicular to the nanowire (upper) and along the nanowire (lower). (c) Stability map (Coulomb diamonds) obtained by plotting differential current through the device as a function of source-drain bias  $V_d$  and wrap-gate voltage  $V_g$ . Data reproduced from Sellier *et al.* (2006) and from Hofheinz *et al.* (2006b).

regime, as shown in Fig. 28(c), which demonstrates bias spectroscopy (‘Coulomb diamonds’) taken over a wide range of electron occupancy, with high stability and almost constant charging energy (Hofheinz *et al.*, 2006b). Similar FinFET structures have also been used for single dopant tunneling studies – see Section V.B.2.

### C. Charge sensing techniques

The non-invasive sensing of charge displacements in quantum nanostructures was first demonstrated in a GaAs/AlGaAs heterostructure device (Field *et al.*, 1993), when a quantum point contact (QPC) was used to detect the change in occupancy of a quantum dot. Here, the QPC is biased close to pinch-off, where its transconductance  $dI/dV_G$  can be very large. Any small charge displacement in the vicinity of the QPC channel can then lead to a significant change in QPC current, via its capacitive coupling. This technique has since been applied widely, enabling the direct probing of single electron charges and the indirect probing of single spins in nanostructures based on a variety of materials systems, including silicon.

Sakr *et al.* (2005) fabricated a QPC adjacent to a quantum dot in a Si/SiGe heterostructure using a combination of isolation etching and metal gates aligned to the etched trenches. While this structure enabled sensing of the dot’s electron occupancy in the many-electron regime,

it did not have sufficient sensitivity to probe down to the last electron. Simmons *et al.* (2007) used Pd metal surface depletion gates on a Si/SiGe heterostructure to define a similar geometry – see Fig. 29a. By monitoring the differential conductance of the QPC sensor they were able to accurately probe the depopulation of electrons in the adjacent quantum dot, even when the transport current  $I_{\text{Dot}}$  through the dot had fallen below the noise level (Fig. 29b). In this way they were able to track the occupancy of the dot down to the final electron, as shown in Fig. 29(c).

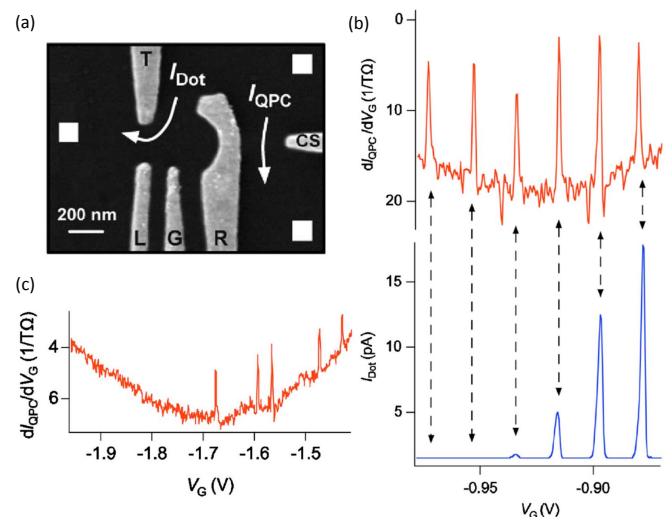


FIG. 29 **Non-invasive charge sensing of a Si/SiGe quantum dot using a quantum point contact (QPC) sensor.** (a) SEM device image. (b) (Top) Derivative of the QPC current  $dI_{\text{QPC}}/dV_G$  as a function of gate voltage  $V_G$ . The peaks correspond to changes in the number of electrons in the dot. (Bottom) Current  $I_{\text{Dot}}$  through the quantum dot as a function of  $V_G$ . (c) QPC sensor output in the few-electron limit. No further transitions occur for  $V_G < 1.68$  V, indicating that the quantum dot is empty of electrons. From Simmons *et al.* (2007).

More recently, QPC sensors have been used with great versatility in both Si/SiGe and Si MOS quantum dots systems for measurement of both charge (Nordberg *et al.*, 2009b) and spin (Hayes *et al.*, 2009; Simmons *et al.*, 2011; Xiao *et al.*, 2010a) states. A technique developed to measure the spin state of a single electron in a GaAs/AlGaAs quantum dot (Elzerman *et al.*, 2004) has been successfully applied to dots in silicon. This involves loading an electron (of indeterminate spin) into an empty quantum dot and positioning the Fermi level so that only a spin-up electron is able to tunnel out, with the charge displacement monitored by a QPC sensor. The technique has been used to measure the spin lifetime of single electrons loaded into Si/SiGe (Hayes *et al.*, 2009; Simmons *et al.*, 2011) and Si MOS (Xiao *et al.*, 2010a) quantum dots. These experiments are discussed in more detail in Section VI, which focuses on time-resolved spin measure-

ments.

Single electron transistors (SETs) can also be used as highly sensitive electrometers in nanostructure devices. The most sensitive such electrometers employ Al metal islands, with  $\text{Al}_2\text{O}_3$  tunnel barriers, which can be integrated with both MOS (Andresen *et al.*, 2007) and Si/SiGe-based quantum dots (Yuan *et al.*, 2011). Integrating such SETs into a radio-frequency (rf) tank circuit forms an rf-SET (Schoelkopf *et al.*, 1998), which can operate at frequencies above 100 MHz with charge sensitivities approaching  $\sim 10^{-6} e/\sqrt{\text{Hz}}$ . Andresen *et al.* (2007) fabricated such an Al- $\text{Al}_2\text{O}_3$  rf-SET on the surface of a phosphorus-doped silicon (Si:P) device to study the gate-controlled transfer of an electron between two implanted phosphorus donors, with a measurement bandwidth exceeding 1 MHz. They were able to study the charge relaxation rate as a function of gate-induced detuning between the two donor levels, measuring an oscillating relaxation rate consistent with acoustic phonon emission in silicon.

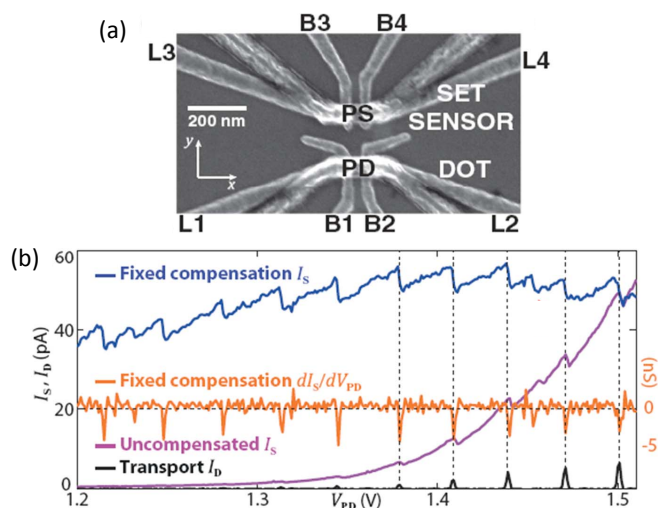


FIG. 30 **Non-invasive charge sensing of a Si MOS quantum dot using a single electron transistor (SET) sensor.** (a) SEM device image, showing a Si MOS SET sensor (upper device) that is capacitively coupled to a Si MOS quantum dot (lower device). (b) Transport current  $I_D$  through the quantum dot (black) shows Coulomb peaks as a function of dot plunger gate voltage  $V_{PD}$ . The changing potential on the dot is detected by monitoring the current  $I_S$  through the SET sensor, which shows charge transfer events superimposed on a rising background (purple trace), due to the coupling of the SET to  $V_{PD}$ . This background can be largely removed by adding a linear correction (compensation) to the SET gate voltage  $V_{PS}$ , leading to the blue trace, and then further enhanced by plotting the derivative  $dI_S/dV_{PD}$ . Data reproduced from Yang *et al.* (2011).

While Al- $\text{Al}_2\text{O}_3$  rf-SETs are well established as fast charge sensors, it is advantageous to integrate the SET sensor into the silicon device itself, as has been done with silicon-based QPC sensors, since this can improve the capacitive coupling to the system being measured and can

also simplify fabrication. Furthermore, the larger charging energies that can be obtained with silicon quantum dots, compared with Al metal islands, provides the potential for increased sensitivity and higher operating temperature. Figure 30 shows an example of a silicon SET integrated adjacent to a Si MOS quantum dot (Yang *et al.*, 2011). In this experiment, Yang and co-workers also employed a dynamic feedback technique to keep the SET sensor at a point of constant sensitivity, allowing for more robust measurements that can tolerate random charge displacement events. Podd and co-workers in Cambridge also demonstrated a capacitively coupled pair of Si MOS quantum dots, in which one of the dots could be used to sense the potential of the other (Podd *et al.*, 2010).

Angus *et al.* (2007) configured a silicon-based rf-SET by using a double-gate structure to induce a Si-MOS quantum dot and connecting this within a radiofrequency tank-circuit. They demonstrated a charge sensitivity of better than  $10^{-5} e/\sqrt{\text{Hz}}$  at a bandwidth up to 2 MHz, which compares well with metallic rf-SETs. In their device the bandwidth was limited by a high gate resistance, but there is no reason why such a structure could not be designed to operate at bandwidths above 100 MHz. One advantage of a Si-MOS SET compared with its Al- $\text{Al}_2\text{O}_3$  counterpart is that the tunnel barriers of the Si-MOS device are gate controlled, meaning that the resonant frequency of the tank circuit can be easily tuned to optimize its operation.

For studies of spin dynamics, which can be orders of magnitude slower than charge dynamics in silicon, the need for high-frequency sensing becomes less critical and standard low-frequency (sub-MHz) SET operation can be used (Hofheinz *et al.*, 2006a). Most notably, Morello *et al.* (2010) used a Si-MOS SET, similar to the structure used by Angus *et al.* (2007), to detect charge motion between the SET island and implanted phosphorus dopants, thus enabling single-shot spin readout of an electron bound to a phosphorus donor. This experiment is discussed further in Section VI.C.3.

#### D. Few-electron quantum dots

For many years it was difficult to achieve single-electron occupation in gated quantum dots, in spite of the tunability of such dots. The fundamental problem was the difficulty maintaining reasonably fast tunnel rates between a quantum and nearby charge reservoirs. A common gate design (see, e.g., Waugh *et al.* (1995)), is shown schematically in Fig. 31(a). As the quantum dot is made smaller, by making the gate voltages more negative, the tunnel barriers to one or both reservoirs must become wider.

Fig. 31(b) shows an alternative approach for the formation of few-electron quantum dots in GaAs, developed by the group in Ottawa (Ciorga *et al.*, 2000). The advan-

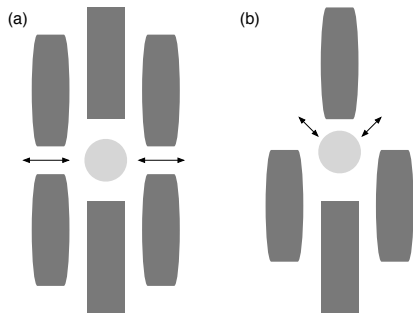


FIG. 31 **Gate design enabling few-electron occupation.** The gate design in (a) is a natural way to form a quantum dot tunnel-coupled to two reservoirs, as shown by the arrows. As the dot becomes smaller, however, it is very difficult to maintain a high tunnel rate to both reservoirs. The gate design in panel (b), based on Fig. 1 of Ciorga *et al.* (2000), enables a small dot to be coupled to both reservoirs.

tage of this gate design is that it enables strong tunnel coupling to both reservoirs even when the quantum dot is small. This gate design is equally useful for gated dots in Si, and it was first implemented in a Si/SiGe heterostructure in Sakr *et al.* (2005), enabling observation of both Coulomb blockade and charge sensing, but not single-electron occupation.

The challenge to achieving single electron occupation in both single and double one-electron dots in Si/SiGe has been to bring under control instability in the background offset charge of the quantum dots. In 2007 Simmons *et al.* (2007) demonstrated single-electron occupation in a top-gated, Si/SiGe quantum dot. In that work, care was taken to ensure that the doping of phosphorous in the modulation doping layer was not larger than necessary; limiting the doping in this layer appears to improve the stability of devices. The primary evidence for single-electron occupation was the absence of additional charge transitions, as shown in Fig. 29, for a change in gate voltage more than 3.5 times as large as that required to add the last observed electron.

Metal-oxide-semiconductor quantum dots can also approximate the few-electron regime (Prati *et al.*, 2011). In the approach of Xiao *et al.* (2010b), the depletion gates underneath a global accumulation gate form the quantum dot. Using an approach analogous to this type of MOS Si structure, Borselli and collaborators have shown that single-electron occupation can be achieved in very stable Si/SiGe quantum dots when the doping is removed from the structure (Borselli *et al.*, 2011a), see section IV.B.4.

A novel approach to achieving single-electron occupation was demonstrated by Borselli and colleagues at HRL Laboratories (Borselli *et al.*, 2011b). As shown in Fig. 32, the device structure uses two quantum wells, the lower of which is doped. An air bridge is used to apply a positive voltage to an isolated, circular surface gate, pulling electrons into the upper quantum well. Nearby surface

gates are negatively biased, enabling the formation of a charge-sensing channel in the lower electron layer. Such a device forms an extremely symmetric quantum dot that is easily tuned to the one-electron charge state.

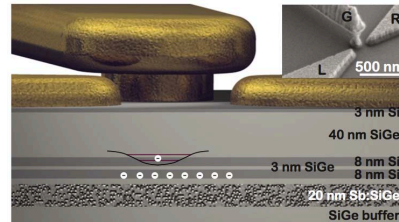


FIG. 32 Schematic diagram of a few-electron quantum dot formed from a Si/SiGe heterostructure with a double quantum well and an accumulation gate contacted by an air bridge. Inset: SEM micrograph of the gate region of a corresponding device. Figure from Borselli *et al.* (2011b).

Few-carrier occupation can be accomplished even in the absence of charge sensing, as demonstrated in nanowire-based hole quantum dots for which the Coulomb diamonds open to very large gate voltages at sufficiently positive gate voltage (Zhong *et al.*, 2005). Zwanenburg and collaborators have reached the one-hole state in a very small Si quantum dot in a nanowire, enabling them to perform spin spectroscopy (Zwanenburg *et al.*, 2009b). The device made use of NiSi contacts, in which a Schottky barrier defines the quantum dot, as shown in Fig. 33. The few-electron regime was also observed without charge sensing in planar MOS Si quantum dots, thanks to the high degree of tunability of these devices (Lim *et al.*, 2011, 2009b).

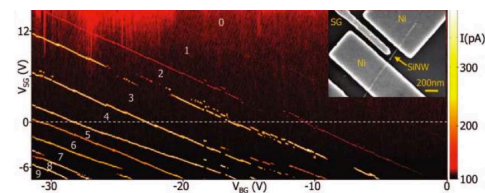


FIG. 33 Transport data showing the last hole in a Si nanowire based quantum dot. Inset: SEM image of the device showing the NiSi contacts and a Cr/Au side gate. device. Figure from Zwanenburg *et al.* (2009b).

## E. Spins in single quantum dots

In the previous sections we have established the evolution in recent years from the observation of simple localization and coulomb blockade to few-electron quantum dots in silicon. With the understanding and control of the charge side of electrons one can also probe their spins. In this section we first discuss experiments on ground-state and excited-state magnetospectroscopy in silicon quantum dots. The existence of valleys in silicon make the

spin filling non-trivial: the configuration and mixing of valleys and orbits determines how electrons will consecutively occupy the available spin-up or down states.

### 1. Spin-state spectroscopy

The most straightforward methods of measuring electron spin states in quantum dots are ground-state and excited-state magnetospectroscopy (Hanson *et al.*, 2007). Excited-state magnetospectroscopy allows observation of spin excited states at a fixed magnetic field (Cobden *et al.*, 1998), as long as the Zeeman energy can be resolved. Four experimental demonstrations in silicon systems are bottom-up Si and SiGe nanowires (Hu *et al.*, 2011; Roddaro *et al.*, 2008; Zwanenburg *et al.*, 2009b) and SiGe nanocrystals (Katsaros *et al.*, 2010), see Fig. 34. When the spin-excited state is measured at different magnetic fields, one can extract the g-factor by plotting the Zeeman energy versus magnetic field, see Fig. 34(b). The first two holes in a Si nanowire quantum dot were found to have a g-factor of  $2.3 \pm 0.2$  in perpendicular magnetic field. In SiGe nanocrystals and nanowires the g-factor is anisotropic: the results in Figure 34(c) show g-factors of  $g_{\parallel} = 1.21$  and  $g_{\perp} = 2.71$  for respectively parallel and perpendicular field.

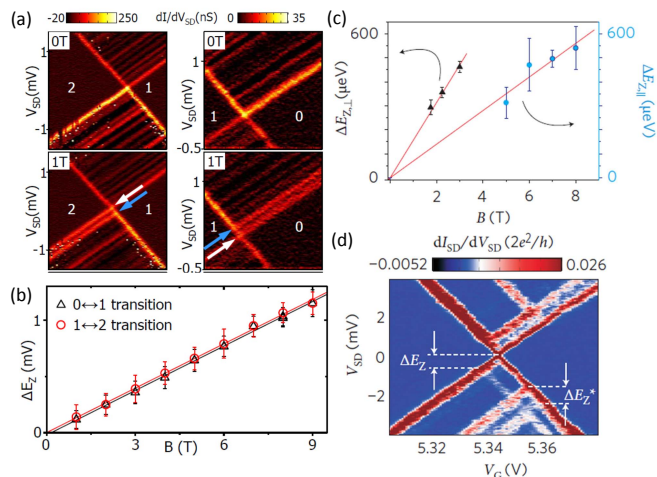


FIG. 34 **Excited-state magnetospectroscopy in Si quantum dots.** (a) Zeeman splitting at the 0-1 and 1-2 transition in a few-hole Si nanowire quantum dot and (b) the corresponding magnetic field dependence of the Zeeman energy, data from Zwanenburg *et al.* (2009b) (c), Anisotropic g-factors in SiGe nanocrystals, and (d) the corresponding excited-state magnetospectroscopy, data from Katsaros *et al.* (2010).

In case of ground-state magnetospectroscopy, the spin filling is investigated by measuring the magnetic field dependence of the electrochemical potential  $\mu_N$ , which is by definition the energy required for adding the  $N^{\text{th}}$  electron to the dot. The slope of  $\mu_N(B)$  is given by

$\frac{\partial \mu_N}{\partial B} = -g\mu_B \Delta S_{\text{tot}}(N)$ , where  $g$  is the g-factor, the Bohr magneton  $\mu_B = 58 \mu\text{eV/T}$  and  $\Delta S_{\text{tot}}(N)$  is the change in total spin of the dot when the  $N^{\text{th}}$  electron is added (Hada and Eto, 2003). The electrochemical potential has a slope of  $+g\mu_B/2$  when a spin-up electron is added, whereas addition of a spin-down electron results in a slope of  $-g\mu_B/2$ . The rate at which  $\mu_N$  changes with magnetic field thus reveals the sign of the added spin.

Rokhinson *et al.* (2000) were the first to observe the theoretically expected slopes in multiples of  $g\mu_B/2$  in an n-type Si quantum dot. They show the peak shift with magnetic field of 29 electrons entering the dot, and more detailed measurements on two sets of Coulomb peaks with slopes of  $\pm 1/2g\mu_B$  and  $\pm 3/2g\mu_B$ . The charge transitions display an unexpected large number of kinks at which the slope changes sign, and thus the spin state as well. They conclude that the spin filling is inconsistent with a simple picture of non-interacting electrons in four single-particle levels. Later reports are more straightforward to interpret and will be discussed below.

The spin filling of holes has been investigated in nanowire quantum dots. In 2005, Zhong *et al.* (2005) found alternating spin-up and spin-down holes in a many-hole quantum dot. The magnetic field evolution of the positions of eight consecutive Coulomb peaks in Figure 35(a) reveals alternating slopes of  $\pm g\mu_B/2$ , with an extracted g-factor of  $2 \pm 0.2$ . The few-hole regime displayed similar spin filling of the first four holes in an empty dot (Zwanenburg *et al.*, 2009b), see Fig. 35(b). The even-odd filling suggests that the degeneracy of heavy and light holes is lifted due to strain and confinement effects; see, for example, calculations based on density functional theory (Leu *et al.*, 2006; Sorokin *et al.*, 2008) and tight-binding models (Buin *et al.*, 2008; Niquet *et al.*, 2006). SiGe nanowires have been shown to exhibit the same spin filling, see (Roddaro *et al.*, 2008) and Figure 35(c).

### 2. Spin filling in valleys and orbits

The even-odd spin filling as observed in p-type silicon quantum dots (see Section IV.E.1) is not very different from similar devices in other material systems. However, the valleys in the silicon conduction band make the spin filling of *electrons* non-trivial. Valley physics in silicon has been studied extensively both theoretically (Culcer *et al.*, 2010a,b; Friesen and Coppersmith, 2010; Saraiva *et al.*, 2009, 2010) and experimentally (Fuechsle *et al.*, 2010; Goswami *et al.*, 2007; Koester *et al.*, 1997; Köhler and Roos, 1979; McGuire *et al.*, 2010; Nicholas *et al.*, 1980; Pudalov *et al.*, 1985; Takashina *et al.*, 2006).

As discussed in Section III.B.2 a 2-dimensional electron gas has two  $\Gamma$ -valleys, separated by the valley splitting  $E_V$ , see Fig. 7. A finite valley splitting influences the spin filling as observed in ground-state magnetospectroscopy (Hada and Eto, 2003): the first electron is al-

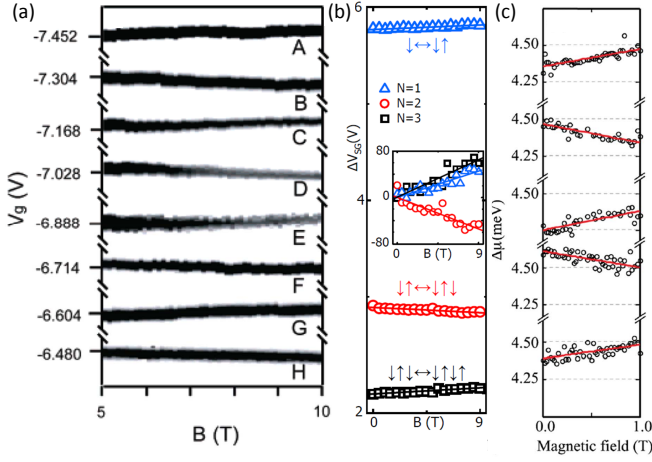


FIG. 35 **Ground-state magnetospectroscopy.** Three examples of even-odd hole spin filling in (a) a many-hole Si nanowire quantum dot (Zhong *et al.*, 2005) (b), a few-hole Si nanowire quantum dot (Zwanenburg *et al.*, 2009b) and (c), a many-hole Ge/Si nanowire quantum dot (Roddaro *et al.*, 2008).

ways a spin-down, yielding a slope of the corresponding Coulomb peak of  $-g\mu_B/2$ , see the experiment by Lim *et al.* (2011) in Fig. 36b. The kink in the second Coulomb peak (marked 2a) at  $\sim 0.86$  T is caused by a sign change of the  $N = 2$  ground-state spin: at low magnetic field (before the kink), the second electron fills the quantum dot with a spin-up. As the magnetic field is increased, the sign of the second electron spin changes from up to down at  $B \sim 0.86$  T.

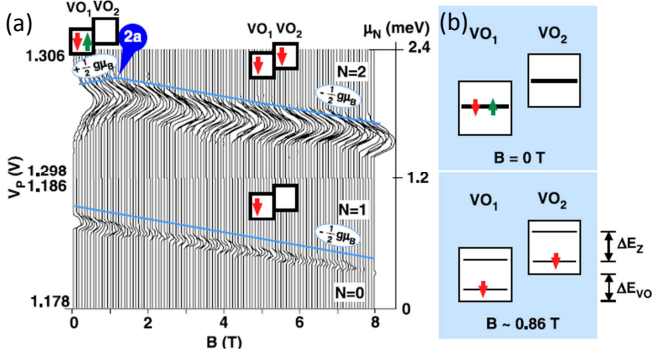


FIG. 36 **Spin filling in valleys in a planar MOS Si quantum dot.** (a) Magnetospectroscopy of the first two electrons entering the quantum dot. The circle 2a marks a kink in the second Coulomb peak at  $\sim 0.86$  T. The arrows in the boxes (VO<sub>1</sub> for valley-orbit 1 and VO<sub>2</sub> for valley-orbit 2) represent the spin filling of electrons in the quantum dot. (b) For  $B < 0.86$  T, the first two electrons fill with opposite spins in the same valley-orbit level (left panel). The Zeeman energy at the kink is equal to the valley-orbit splitting (0.10 meV). Data reproduced from Lim *et al.* (2011)

When the valleys and orbits are mixed (section III.B.2), there are no pure valleys or pure orbits, and

the lowest available levels are referred to as valley-orbits. The sign change can then be explained with a simple model where the two lowest valley-orbit levels are separated by the valley-orbit splitting  $\Delta E_{VO}$ , see Fig. 36(b). At zero magnetic field, the first two electrons fill with opposite spins in valley-orbit level 1. When a magnetic field is applied, the spin-down and spin-up states are split by the Zeeman energy  $E_Z$ . Above 0.86 T the spin-up state of valley-orbit level 1 (VO<sub>1</sub>) is higher in energy than the spin-down state of valley-orbit level 2 (VO<sub>2</sub>) and it becomes energetically favored for the second electron to occupy the latter, i.e. VO<sub>2</sub>. At the kink the valley-orbit splitting equals the Zeeman energy, which is 0.10 meV at 0.86 T. Comparable kinks were reported simultaneously in accumulation mode Si/SiGe quantum dots, yielding valley splittings of 0.12 and 0.27 meV (Borselli *et al.*, 2011b). In 2010, the absence of kinks in the ground-state magnetospectroscopy of a planar MOS Si quantum dot was explained as a result of a large exchange energy and an unusually large valley splitting of 0.77 meV (Xiao *et al.*, 2010b).

## F. Double quantum dots

Like their counterparts in the Ga-AlGaAs material system, double quantum dots in silicon represent the natural extension from a semiconductor ‘artificial atom’ to an ‘artificial molecule’. As outlined in the previous sections, it took until around 2006 for low-disorder silicon-based quantum dots to be produced with reasonable repeatability. Correspondingly, this is also when the first demonstrations of double quantum dots in silicon began to be reported.

### 1. Charge-state control

One of the earliest reports of silicon double dot operation was by Gorman *et al.* (2005), who formed an isolated double dot by etching a thin (35 nm) layer of bulk-phosphorus-doped silicon (Si:P) in a SOI substrate. They also integrated a nearby SET, again formed by etching the Si:P layer, which they used to monitor charge transfer in the double dot. By rapidly pulsing a nearby control gate they observed oscillations in the charge state of the double dot, as a function of pulse length, which they interpreted as coherent oscillations between the  $(n, m)$  and  $(n-1, m+1)$  charge states of the double dot. Because of the high electron numbers in the dots resulting from the degenerative doping, and the difficulty of controlling the dots size via the etching process, this type of dot structure has not progressed significantly since this time, and most studies of silicon quantum dots are now based on dots induced in undoped silicon layers.

The starting point for any experimental study of a dou-

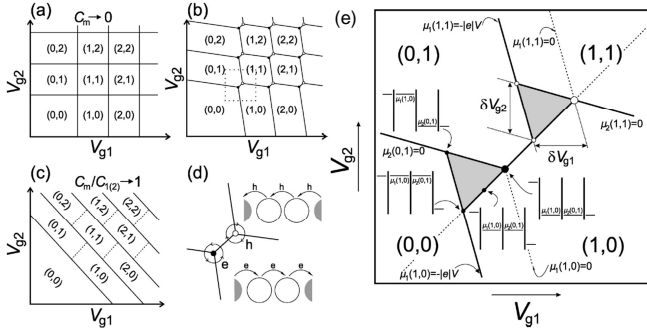


**FIG. 37 Schematic stability diagrams for a double dot system.** Maps are shown for (a) small, (b) intermediate, and (c) large inter-dot coupling. The equilibrium charge on each dot in each domain is denoted by  $(N_1, N_2)$ . (e) Region within the dotted square of (b), corresponding to the unit cell of the double dot stability diagram, at finite bias voltage. The solid lines separate the charge domains. Classically, the regions of the stability diagram where current flows are given by the gray triangles. Reproduced from Van der Wiel *et al.* (2003).

ble quantum dot is the determination of its charge state  $(N_1, N_2)$  as a function of at least two gate voltages  $V_{g1}$  and  $V_{g2}$  controlling the system. Here  $N_1, (N_2)$  is the electron occupancy of dot-1 (dot-2). By directly measuring the transport current  $I$  through the dot, or by measuring the local electrostatic potential of the system using a nearby QPC or SET charge sensor, one can plot a charge stability map as a function of  $V_{g1}$  and  $V_{g2}$ . Van der Wiel *et al.* (2003) provide an excellent review of semiconductor double quantum dots and Fig. 37(a-c) taken from this review depicts the charge stability maps expected for different inter-dot coupling strengths. Figure 37(b) shows a map at intermediate inter-dot coupling, where one observes a characteristic ‘honeycomb’ like structure. The points on the map where three different charge states are degenerate in energy are known as ‘triple points’ and it is only at these points where a transport current  $I$  can flow through the system, from source to drain (Fig. 37d). If we then apply a source-drain bias  $V_{SD}$  across the double dot these triple points expand to take on a triangular shape, as shown in Fig. 37(e). It should be noted that while in a transport measurement only the triple points (or bias triangles) can be observed, when charge sensing is employed one can also directly detect the transition lines between charge states. Das Sarma and co-workers have recently applied a Hubbard model approach to determine the charge stability diagrams for silicon double dots (Das Sarma *et al.*, 2011), showing excellent agreement with experiments (Lai *et al.*, 2011; Simmons *et al.*, 2009).

The first clear demonstration of a double quantum dot in nominally undoped silicon (Fujiwara *et al.*, 2006) used a double-gated silicon nanowire formed from a SOI substrate, with three independently controlled barrier gates. This device structure was previously described in Section

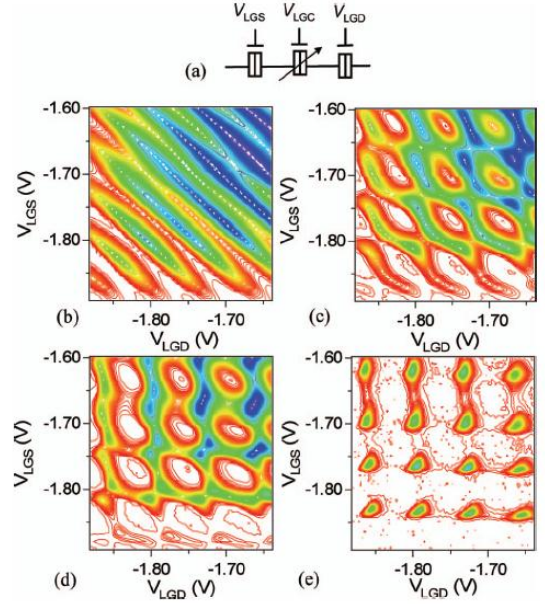


**FIG. 38 Evolution from a single dot to a double quantum dot in a gated silicon nanowire device.** (a) Equivalent circuit. (b-e) Contour plots of the drain current as a function of the outer barrier gate voltages  $V_{LGS}$  and  $V_{LGD}$ . The central barrier gate voltages used were  $V_{LGC} = -0.75$  (b),  $-1.13$  (c),  $-1.18$  (d), and  $-1.284$  V (e). Data reproduced from Fujiwara *et al.* (2006).

IV.B.5 and is depicted in Fig. 27(a,b). By varying the voltage  $V_{LGC}$  on the central barrier gate, Fujiwara and co-workers were able to gradually tune the system from one large dot to two well-isolated dots, as evidenced by the charge stability plots shown in Fig. 38(b-e). In Fig. 38(b) the central gate voltage  $V_{LGC}$  is tuned to minimize the tunnel barrier between the dots, forming one large dot. As the outer barrier gate voltages  $V_{LGS}$  and  $V_{LGD}$  are varied, the transport current  $I$  plotted in Fig. 38(b) shows Coulomb blockade oscillations as a function of the addition voltage  $(V_{LGS} + V_{LGD})$ , which can be compared with Fig. 37(c), indicating that one large dot is present. However, as the tunnel barrier height is increased by tuning  $V_{LGC}$ , two separate dots form, as revealed in Figs. 38(c-e) with the gradual formation of a honeycomb-shaped map of  $I(V_{LGS}, V_{LGD})$ , consistent with that in Fig. 37(b). Gate-tunable double quantum dots based on etched silicon nanowires have since also been reported by other groups (e.g. Pierre *et al.* (2010)).

Epitaxially grown nanowires have also been configured as double quantum dots. Hu and co-workers from Harvard (Hu *et al.*, 2007) used a Ge/Si core/shell nanowire, as described in Section IV.B.1, with a number of surface metal gates to demonstrate a highly-tunable double dot device, as shown in Fig. 39. Figs. 39(b, c) show the evolution of the charge stability map from a strongly coupled single dot to a double dot as the central barrier gate is

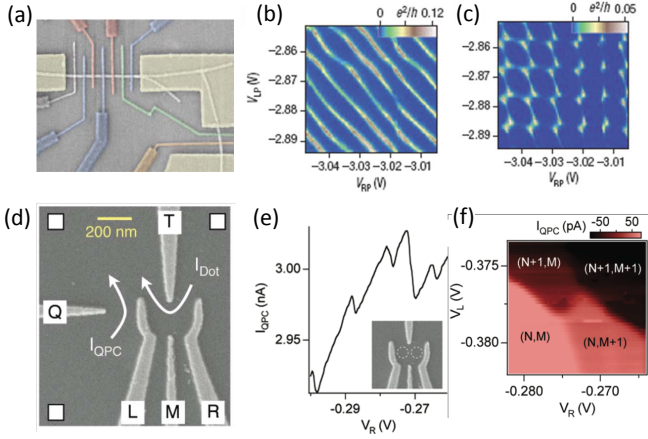


**FIG. 39 Gate tunable double quantum dots.** (a) SEM image of a Ge/Si nanowire-based hole quantum dot. The Ge/Si nanowire at top (white in image) is gated by metal gates to form a double dot. (b,c) Charge stability maps of the conductance as a function of plunger gate voltages. (d) SEM image of an electron quantum dot defined by electrostatic top gates in a Si/SiGe heterostructure. (e) Charge sensing measurement showing the difference in the charge detection signal from the dot furthest from the QPC (4 small steps in  $I_{QPC}$ ) and the dot closest to the QPC (single large step) as a function of gate voltage. (f) Two-dimensional plot of the charge sensing current showing the sequential addition of electrons to the left and right dots. Data in (a-c) reproduced from Hu *et al.* (2007); data in (d-f) reproduced from Simmons *et al.* (2009).

tuned.

Using a gated etched nanowire device, Liu *et al.* (2008a) were able to explore the excited state energy levels within a double quantum dot, which in this case was formed using two barrier gates and the presence of a third barrier created by local disorder. Figure 40(a) shows the charge stability diagram for this double dot in the presence of a source-drain bias, which transforms each triple point into a ‘bias triangle’, as described in Fig. 37(e). By mapping the bias triangle in more detail, Liu and co-workers were able to observe resonant tunnelling through excited states of the double dots. Using a planar MOS structure, similar to that in Fig. 25(a,b), Lim *et al.* (2009a) were also able to observe excited state transport through a double quantum dot, this time controlled using three independent barrier gates. Figure 40(b) shows a pair of bias triangles for two triple points, each showing structure in the source-drain current  $I_{SD}$ , that is further revealed in Fig. 40(c), which shows a line trace of  $I_{SD}$  along the detuning axis  $\epsilon$ .

Simmons *et al.* (2009) demonstrated one of the first highly tunable double quantum dots in a gated Si/SiGe device. The device structure shown in Fig. 39(d) also incorporated a QPC charge sensor, which enabled mapping of the double dot charge stability as a function of the gate voltages  $V_L$  and  $V_R$  controlling the two dots

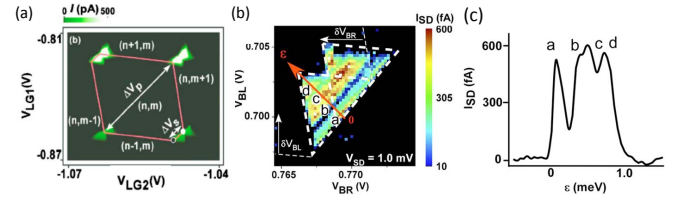


**FIG. 40 Bias spectroscopy of silicon double quantum dots.** (a) Stability map with a source-drain bias  $V_{SD} = 1$  mV for a silicon nanowire double dot, depicted in Fig. 27, obtained by plotting source-drain current  $I$  as a function of two barrier gate voltages. The triple points have clearly evolved into bias triangles. (b) Bias triangles for two triple points at  $V_{SD} = 1$  mV, obtained in a Si MOS double dot. (c) Line trace of  $I_{SD}$ , taken along red arrow in (b), showing resonances corresponding to excited states in the double dot. Data reproduced from Liu *et al.* (2008a) and Lim *et al.* (2009a).

(see Fig. 39(e,f)). They were able to tune the inter-dot coupling by control of the central gate voltage  $V_M$ . The same group were able to demonstrate depletion of a double quantum dot to the single electron level (Thalakulam *et al.*, 2010). The data in Fig. 41(b) shows a charge stability map of the double dot, measured using the QPC sensor. The lack of charge transitions in the lower left quadrant of this map demonstrates control of electron number down to the (0,0) charge state.

Occupation down to the (0,0) charge state in a double dot has also been recently demonstrated in an undoped Si/SiGe heterostructure device (Borselli *et al.*, 2011b), in which a two-layer gate structure analogous to that used for Si MOS dots (see Fig. Xa,b) was used, resulting in a very stable system. Very recently, a few-electron double dot has been demonstrated in an isotopically-enriched  $^{28}\text{Si}$  quantum well (Wild *et al.*, 2012).

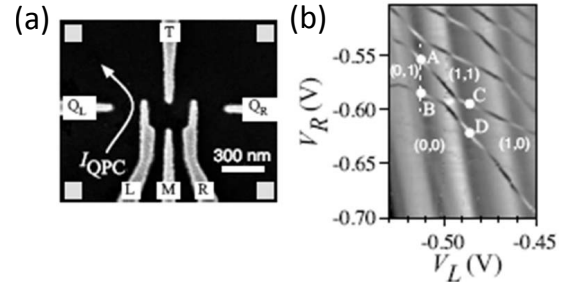


**FIG. 41 Single electron occupancy in a Si/SiGe double quantum dot.** (a) SEM of the device. (b) Charge stability map of the double dot, obtained by plotting the QPC charge sensor output as a function of the control gate voltages  $V_L$  and  $V_R$ . The charge configurations  $(n, m)$  are marked, showing depletion to the (0,0) state. Data reproduced from Thalakulam *et al.* (2010).

## 2. Spin transport in double quantum dots

As discussed in Section V.D, in tightly-confined quantum dots the singlet-triplet exchange energy for an electron pair can become appreciable. In a double quantum dot system this can lead to an effect known as Pauli spin blockade, where transport through the double dot is dependent upon the spin state of the electron. This phenomenon was first observed in 2002 in a GaAs/AlGaAs double quantum dot (Ono *et al.*, 2002). In 2008 Liu and co-workers observed Pauli blockade in a silicon nanowire device similar to that shown in Fig. 27(a,b), in which a double quantum dot was formed using two barrier gates and a third barrier created by local disorder (Liu *et al.*, 2008b).

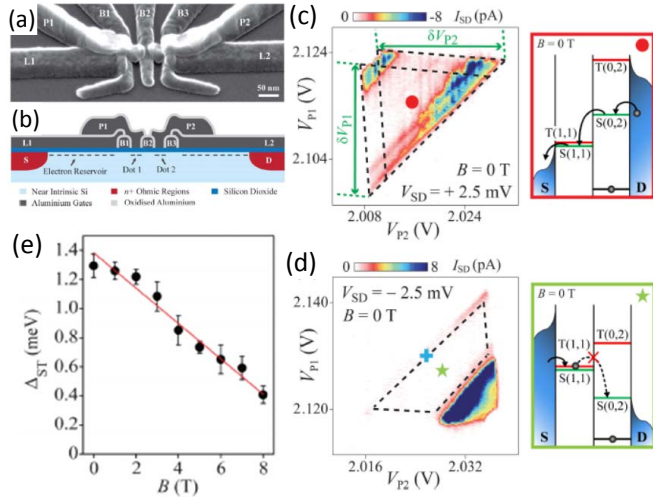


**FIG. 42 Pauli spin blockade in a silicon MOS double quantum dot.** (a) SEM image and (b) cross-sectional schematic of the Si MOS device. Gates L1 and L2 induce electron reservoirs at the Si/SiO<sub>2</sub> interface, while barrier gates B1-B3 define the double dot potential. Plunger gates P1 and P2 control the occupancy of each dot. (c,d) Current  $I_{SD}$  as a function of  $V_{P1}$  and  $V_{P2}$  for  $B = 0$  T. (c) For  $V_{SD} = +2.5$  mV, the ground state and excited states of a full bias triangle are observed. The current flows freely at the  $S(0,2)$ - $S(1,1)$  transition, as illustrated in the box marked by the red dot. (d) The same configuration at  $V_{SD} = -2.5$  mV. Here the current between the singlet and triplet states is fully suppressed by spin blockade (green box). (e) The measured singlet-triplet splitting  $\Delta_{ST}$ , plotted as a function of magnetic field  $B$ . Figure from Lai *et al.* (2011).

Lai *et al.* (2011) demonstrated Pauli blockade in a Si MOS double quantum dot formed using an Al-Al<sub>2</sub>O<sub>3</sub> multi-layer gate stack, similar to that discussed in Section IV.B.4. Their device structure, shown in Fig. 42(a,b), incorporated three barrier gates (B1, B2, B3) and two ‘plunger’ gates (P1, P2) which controlled the occupancy of the two dots. Pauli blockade occurs in one bias direction only, as depicted in Fig. 42. The phenomenon is revealed experimentally via the difference between the bias triangles for positive and negative source-drain bias

$V_{SD}$ , observed in the charge stability map as a function of the two plunger gate voltages.

For  $V_{SD} > 0$  (Fig. 42c) a pair of overlapping complete bias triangles are observed. Resonant transport through the ground and the excited states in the double dot occurs when the states within the dots are aligned, leading to current peaks that appear as lines parallel to the triangle base. The non-resonant background current in the triangle is due to inelastic tunneling. The non-zero current throughout the triangular region indicates that electrons from the reservoir can tunnel freely from the  $S(0,2)$  singlet state to the  $S(1,1)$  singlet state, as depicted in the cartoon (red box in Fig. 42). For  $V_{SD} < 0$  the current is suppressed in the region bounded by the dashed lines in Fig. 42(d). The suppression arises because the transition from  $T(1,1)$  to  $S(0,2)$  is forbidden by spin conservation during electron tunneling. Once the  $T(1,1)$  triplet state is occupied, further current flow is blocked until the electron spin on one dot reverses its orientation via a relaxation process (green box in Fig. 42).

In Fig. 42(d) it is possible to discern some non-zero current at the bottom of the bias triangle. This ‘leakage current’ in the spin-blockade regions has been identified as resulting from a spin-flip co-tunneling mechanism (Coish and Qassemi, 2011; Lai *et al.*, 2011; Qassemi *et al.*, 2009), where a spin-up electron from one of the reservoirs swaps with a spin-down electron in one of the dots. This effect has also been observed in a double dot formed from an etched silicon nanowire device (Yamahata *et al.*, 2011).

Note that in this experiment (Lai *et al.*, 2011), and also that performed in the nanowire device (Liu *et al.*, 2008b), the electron occupancy in each dot was of order 10 or more, and so the labels (1,1) and (0,2) refer to the effective electron occupancy, whereas the true electron occupancy is  $(m + m_0, n + n_0)$ . Pauli blockade for two-electron singlet and triplet states therefore occurs when the total electron spin of each dot is zero in the  $(m_0, n_0)$  state. More recently, Borselli *et al.* (2011a) have demonstrated a Si/SiGe double dot that exhibits Pauli blockade in the true (1,1)-(0,2) limit. The same group have since used this structure to demonstrate coherent oscillations between singlet and triplet states of the double dot system (Maune *et al.*, 2012), as discussed further in Section VI.C.4.

By applying a magnetic field  $B$ , it is possible to modify the singlet-triplet splitting  $\Delta_{ST}$ , defined as the energy difference between the blocked ground state  $S(0,2)$  and the excited state  $T_-(0,2)$ . In a magnetic field there are four accessible spin states: the singlet  $S$ ; and three triplets  $T_-, T_0$  and  $T_+$ , corresponding to  $S_z = -1, 0, +1$ . Lai *et al.* (2011) studied the singlet-triplet splitting by mapping the bias triangles in the spin blockade regime at increasing magnetic fields  $B = 0 - 8T$ . They found that the splitting  $\Delta_{ST}$  decreased linearly with increasing  $B$  [Fig. 42(e)], as expected, since the triplet states split linearly by the Zeeman energy,  $E_Z = \pm S_z g \mu_B B$ , where



$\mu_B$  is the Bohr magneton and  $S_Z$  is  $-1, 0, +1$ . Here, a linear fit through  $\Delta_{ST}(B)$  yielded a Landé g-factor of  $2.1 \pm 0.2$ , consistent with electrons in silicon.

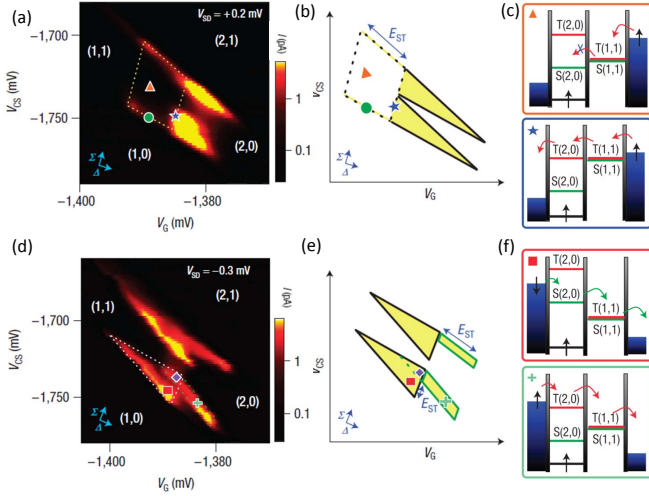


FIG. 43 **Spin blockade and lifetime enhanced transport in a Si/SiGe double quantum dot.** (a) Measured, and (b) schematic, charge stability map of current  $I$  through the double dot, with a source-drain bias of  $V_{SD} = +0.2$  mV. The dotted trapezoids in (a) and (b) mark the zero current regions due to spin blockade, as depicted in the schematics in (c). (d) Measured, and (e) schematic, charge stability map of current  $I$  with a source-drain bias of  $V_{SD} = -0.3$  mV. In this bias direction there is no blockade and current flows throughout the entire bias triangle, however, additional tails are observed due to lifetime enhanced transport, as depicted schematically in (f) and described in the text. Figure from Shaji *et al.* (2008).

Spin transport in silicon double quantum dots can also be strongly affected by the relative values of the spin lifetimes and the various tunnel rates of the system. For example, it is sometimes possible to observe transport through a double dot in gate-space regions where current would normally be blocked, a phenomenon that has been termed lifetime enhanced transport (LET), observed in a Si/SiGe quantum dot structure (Shaji *et al.*, 2008). Shaji and co-workers observed this effect in a device similar to that depicted in Fig. 29, which was originally configured to operate as a single quantum dot. Under certain gate bias conditions a double quantum dot could be formed that exhibited a charge stability map consistent with occupancies down to the single electron level, in particular providing access to the  $(1, 1)$  and  $(0, 2)$  states. In the vicinity of the  $(1, 1) - (0, 2)$  charge transition, a positive source-drain bias ( $V_{SD} = +0.2$  mV) led to bias triangles that exhibited a zero current region due to Pauli blockade (see Figs. 43(a,b)), similar to that observed in Fig. 42.

Under negative bias ( $V_{SD} = -0.3$  mV) the entire bias triangle exhibited a transport current, as expected, but outside the bias triangles additional “tail” regions of non-

zero current were also observed (see Figs. 43(d,e)). These can be understood with reference to the green box in the schematic diagram in Fig. 43(f) and by considering the tunnel rates to the relevant states in the double dot (Simmons *et al.*, 2010). Typically, once the  $S(2, 0)$  state is loaded from the source reservoir (with rate  $\Gamma_{LS}$ ), it would remain locked in position due to Coulomb blockade, and an electron could only pass to the drain via a co-tunneling process (with unloading rate  $\Gamma_S$ ). If, however, the  $S(2, 0)$  loading rate is much slower than the unloading rate ( $\Gamma_{LS} \ll \Gamma_S$ ) and the triplet-singlet relaxation rate  $\Gamma_{TS}$  from  $T(2, 0)$  to  $S(2, 0)$  is also much slower than  $\Gamma_S$ , then the most likely transport pathway is via the  $T(2, 0)$  and  $T(1, 1)$  triplets, as shown in Fig. 43(f), leading to a non-zero current. The upper triangle in the data and schematic diagram, known as the hole triangle, also shows LET behavior. The direction of the “tail” in gate voltage space for the hole triangle is different than that for the electron triangle, a phenomenon that can be explained by a spin-flip co-tunneling process (Koh *et al.*, 2011). This type of spin-lifetime enhanced transport can occur in silicon quantum dots in part because of the very long spin lifetimes present, as discussed further in Section VI.A.

## V. DOPANTS IN SILICON

### A. Dopants in silicon transistors

#### 1. Early work: mesoscopic silicon transistors

Low temperature transport experiments in silicon transistors have been used since the 1980’s to perform spectroscopic measurements of dopants and defect states. Devices reached a sufficiently small length scale about 25 years ago to observe mesoscopic transport phenomenon, see the review by Fowler *et al.* (1988). In these devices the conductance,  $G$ , was found to fluctuate as a function of the gate voltage,  $V_G$  around the threshold, as shown in Fig. 44a. The strongly fluctuating pattern, reproducible within the same cooling cycle, did not originate from electrical noise but from the presence of a finite number of dopant or defect states in the channel. The important length scales needed to understand this phenomenon are the localization length,  $\zeta$  and the device dimensions (channel length  $L$  and channel width  $W$ ). As device dimensions approached  $\sim 100$  nm in size, comparable or less than the localization length, only a limited number of defect or dopant states contributed to the current in contrast to the much larger device dimensions before the 1980’s where these fluctuations were always averaged out.

Three major conduction processes are known to contribute to the conductance of such small transistors, as shown in Fig. 44b. Firstly, there is thermally activated

hopping conduction, where the transported electrons hop via several dopant states from source to drain. This type of transport decreases exponentially with temperature  $T$ , i.e.  $G \propto \exp(-\Delta E/k_B T)$ , where  $\Delta E$  is the energy difference between the localized states of the dominant (most resistant) hop and  $k_B$  is the Boltzmann constant. The second process is direct tunneling, which scales with the barrier height  $E_B$  and  $L$  roughly as  $G \propto \exp(-\sqrt{2m^*}E_B L/\hbar^2)$ . Although typically irrelevant in the early 1980's, his conduction mechanism is playing an increasingly important role in today's nano-scale transistor operation. The last and increasingly important conduction mechanism is tunneling through a single defect. Due to the large number of conductance fluctuations, as depicted in Fig. 44a, the identification of each state with a particular defect or dopants in the channel region was not possible. It should be noted that dopants are not the only sources of disorder that cause localized states in MOSFETs as discussed in Peters *et al.* (1998) and Sanquer *et al.* (2000). However, these early measurements represent the first observation of mesoscopic physics in silicon MOSFET devices, and show how low temperature transport data offer a tool to electrically access dopant states in the channel region.

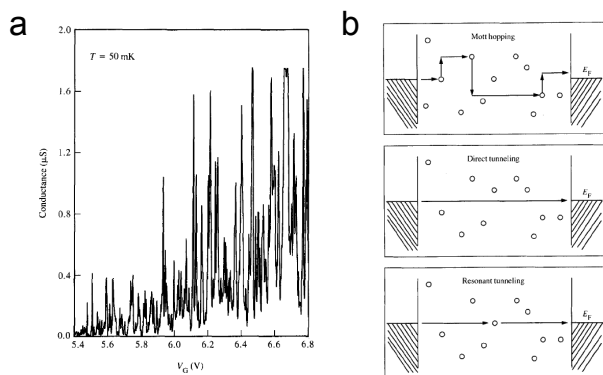


FIG. 44 **Conductance in micron-scale silicon MOSFETs:** (a) Typical low-temperature conductance pattern of a 1980's generation MOSFET around the threshold regime. The strongly oscillating but chaotic pattern that appears at low temperature is associated with localized states in the channel region. (b) Schematic representation of the three major conduction mechanisms through the channel. From Fowler *et al.*, 1988.

## 2. Nano-scale transistors

Following this early work the purity of silicon MOSFETs steadily continued to improve with a concomitant decrease in device size, until the point where discrete impurities clearly started to show up in device transport properties as they reached the nano-scale (Mizuno *et al.*, 1994). Here, fluctuations in the threshold voltage were observed, caused by the statistical fluctuation

in the number of dopants in the channel as a result of the random Poisson distribution during doping. These results challenged the conventional understanding and modeling of micron-silicon devices where continuous ionized dopant charge with smooth boundaries and interfaces had previously been assumed. Now the granularity of the electric charge and the atomicity of matter introduced substantial variation in individual device characteristics, as shown in Fig. 45 (Asenov *et al.*, 2003). In particular the variation in number *and* position of the individual dopant atoms in the active region of MOSFETs were found to make each transistor microscopically different, introducing significant variations from device to device.

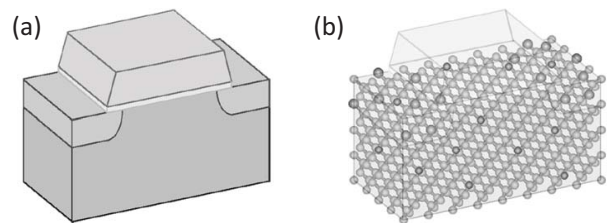


FIG. 45 **The importance of discrete dopants in nano-scale MOSFETs:** (a) The transition from continuously ionized dopant charge and smooth boundaries and interfaces to (b) a 4-nm MOSFET where there are less than 10 Si atoms along the channel. From Asenov *et al.*, 2003.

Recent advances in single ion implantation using a focussed ion beam source have shown that device to device fluctuations can be suppressed by ordering the dopants within the channel. (Shinada *et al.*, 2005). The benefit of ordering the dopants was to create a homogeneous potential distribution in the channel resulting in the formation of a uniform current path. The uniformity in the channel lowers the voltage required to open the channel from the source to the drain allowing for an earlier turn on and reduction of the threshold voltage. This contrasted to devices with a random distribution of dopants where the non-homogeneous potential could lead to a block in the current path. The importance of deterministic doping has recently been highlighted in the 2011 ITRS Emerging Research Materials chapter, where a key challenge for scaling CMOS devices towards 10 nm remains in the ability to control the dopant positions within the channel (ITRS, 2011).

## B. Single dopant transistors

### 1. The demand for single dopant architectures

In parallel with the increasingly important role of individual dopants in classical silicon CMOS devices has been the advent of their importance in quantum computation. In 1998 Bruce Kane introduced the concept

of using the nuclear spins of individual donor atoms in doped silicon electronic devices as quantum bits or qubits (Kane, 1998). Originally Kane envisioned that the quantum information could be stored in the state of the  $^{31}\text{P}$  nuclear spin and accessed by the electron-nuclear hyperfine coupling. Figure 46a shows the basic two qubit unit cell of the Kane proposal based on an arrays of P donors beneath the silicon surface. The addition of a group V phosphorus donor to the silicon crystal results in electron states close in energy to the conduction band but weakly bound to the donor site at low temperatures. The electron has spin  $S = 1/2$ , whilst the host silicon has stable  $I = 0$  isotopes. It is important to isolate the qubits from any degrees of freedom that may lead to decoherence. Recent results have shown that  $^{28}\text{Si}$  can be isotopically refined to a level of 99.98% (Tezuka *et al.*, 2010) making it a good choice for the host material.

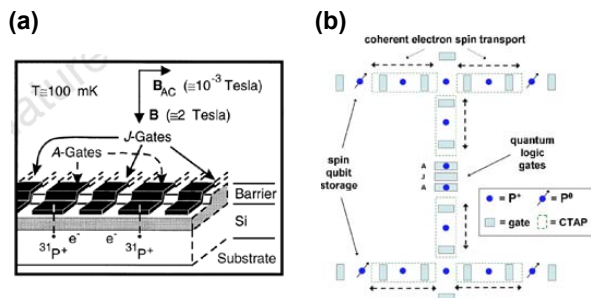


FIG. 46 **Single dopant quantum computing architectures:** (a) Schematic of Kane's proposal for a scalable quantum computer in silicon using a linear array of  $^{31}\text{P}$  donors in a silicon host. From Kane, 1998 (b) A schematic of a 2D donor electron spin quantum computer architecture incorporating distinct storage and interaction region (A-J-A) and ionized  $\text{P}^+$  pathways for coherent transport by adiabatic passage (CTAP). From Hollenberg *et al.*, 2006.

Any proposal for a quantum computer must meet the so-called DiVincenzo criteria (DiVincenzo, 2000), including the ability to operate on individual qubits, couple qubits into quantum logic gates, read-out the information encoded on the qubit, and to be free of environmental effects that destroy qubit entanglement. In Kane's architecture control of the qubit states is achieved by a combination of gates and globally applied a.c. magnetic field. The gates above the donors, labeled *A* gates control the strength of the hyperfine interaction and therefore the resonance frequency of the nuclear spins beneath them. The *J* gates are used to turn on and off the electron-mediated coupling between the nuclear spins. Finally the nuclear spins can be flipped by a resonant globally applied a.c. magnetic field. Read-out of the final spin state is achieved by spin-to-charge conversion and detection through spin-dependent tunneling to a doubly occupied donor state. This donor state is a singlet with a second electron binding energy of 1.7 meV (Larsen, 1981;

Larsen and McCann, 1992). Consequently by applying a differential voltage between the *A* gates charge motion between the donors can only occur if the electrons are in a singlet state. This charge motion can then be detected using a sensitive electrometer nearby, such as a single-electron transistor (SET).

Subsequently a number of proposals for encoding and manipulating quantum information based on donor spin (De Sousa *et al.*, 2004; Hill *et al.*, 2005; Hollenberg *et al.*, 2006; Larionov *et al.*, 2001; Skinner *et al.*, 2003; Stoneham *et al.*, 2003; Vrijen *et al.*, 2000) or charge degrees of freedom (Hollenberg *et al.*, 2004) have been put forward. Electron spins bound to donor nuclei are particularly attractive since they have exceptionally long coherence times and relaxation times relative to the time scales for the control of the quantum state (Hill *et al.*, 2005). The electron spin coherence time of a P donor is  $T_2 > 60$  ms at  $T = 6.9$  K in isotopically pure  $^{28}\text{Si}$  (Tyryshkin *et al.*, 2003). These times are currently limited by the presence of  $^{29}\text{Si}$  which causes spectral diffusion due to the dipolar fluctuations of nuclear spins (Witzel *et al.*, 2005). Dipolar fluctuations in the nuclear spins give rise to a temporally random effective magnetic field at the localized electron spin leading to irreversible decoherence (i.e a  $T_2$  process). Isotopic purification in silicon systems can in principle overcome this limiting process.

These developments have led to the proposal of a complete 2D donor-based architecture, incorporating transport, for a truly scalable design in silicon (Hollenberg *et al.*, 2006). This design has considered the limitations and constraints posed by the sensitivity of the exchange interaction due to donor placement (Koiller *et al.*, 2002a), high gate densities required (Copsey *et al.*, 2003), spin read-out based on spin-charge conversion (Kane, 1998) and the communication bottleneck for linear nearest neighbor qubit arrays. A buried array of ionized donors provide pathways for coherent transport of electron spins for in-plane horizontal and vertical shuttling (dashed border sections) of qubit states into and out of the interaction zones. The overall gate density is low compared to the original Kane version since coherent spin transport is achieved adiabatically, lowering the barriers between donors in a well defined sequence to effect coherent transport by adiabatic passage (CTAP) without populating the intervening donors (Greentree *et al.*, 2004; Rahman *et al.*, 2010). Logic gates are carried out in interaction zones with the *A* and *J* gates for electron spin qubit control and these are distinct from the qubit storage regions. The design allows space for local B-field antennae and SET read-out devices. The introduction of coherent spin transport to donor quantum computing provides a means to consider scalable, fault tolerant architectures.

The use of single donor atoms in silicon as qubits has demanded tremendous advances in single atom fabrication and engineering. Donor separations of order

$\sim 10 - 20$  nm are required to ensure significant coupling between neighboring spins. Currently this is at the limit of what is technologically achievable. Indeed in the original critique of Kane’s paper by DiVincenzo (1998) he recognized that the fundamental and engineering obstacles to implementing the scheme were vast stating “At the time no existing materials-preparation technology will place an array of individual phosphorus atoms at desired spots in the interior of a perfect crystal, let alone systems free from defects in the semiconductor and the overlying oxide layer”. Despite these concerns there have been concentrated efforts internationally to realize a donor-based qubit architecture resulting in a plethora of experiments of transport in nano-scale doped quantum dots and donors. Significant to these results has been the different technologies developed to fabricate donor-based devices.

## 2. Single dopants in MOS-based architectures

In this sub-section we discuss single dopant transport in ultra-scaled MOSFET structures based on randomly and deterministically doped devices. The Kane (1998) proposal sparked the interest in single dopants and small MOSFETs were quickly identified as devices that should easily allow observation of single dopant transport. Tabe *et al.* (2010) confirmed the impact of dopants on the potential landscape of a FET and discussed the evolution from many dopant to single dopant transport. In the newer generation of CMOS devices the issue of random device fluctuations is circumvented in a more straightforward approach, namely by the use of undoped channel FETs. However even in these newest generation of prototype FETs, fluctuations in device characteristics are still evident due to the presence of only a few down to a single *unintentional* dopant(s) in the channel region (Colinge *et al.*, 2007). By now, several groups have reported transport through a random, single dopant in a three terminal configuration (Calvet *et al.*, 2007a,b; Pierre *et al.*, 2010; Sellier *et al.*, 2006). Recently this work has been extended to double gate structures and  $^{28}\text{Si}$  devices (Lo *et al.*, 2009; Roche *et al.*, 2012). Roche *et al.*, 2012 even demonstrated controlled sequential tunneling through two donors. In all these experiments, the number of electrons bound to the dopant atom could be controlled by the gate electrode. Such spectroscopic transport experiments reveal vital information on the orbital levels, the charging energy and the binding energy of the dopant atom and the spin configuration of the bound electron(s) (Lansbergen *et al.*, 2011, 2008). They thus form a powerful characterization tool in the development of single-dopant structures in parallel with the development of precision controlled single dopant devices (Fuechsle *et al.*, 2011).

These experiments all relied on the in-diffusion of

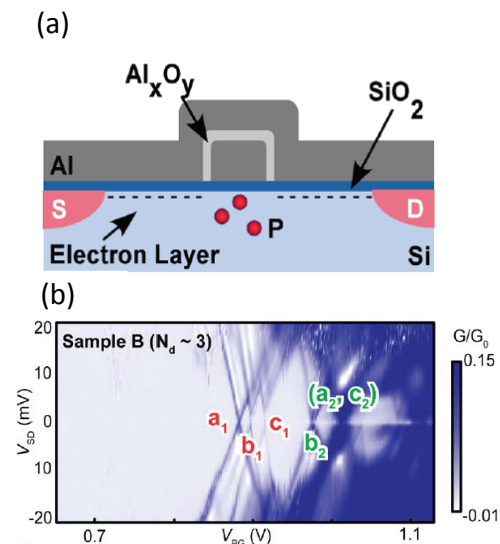


FIG. 47 **Transport through dopants ion-implanted in a nanoFET:** (a) Schematic of a nanoFET where roughly 3 donors have been implanted into the  $50 \times 30$  nm active area of the device. (b) The stability diagram showing the differential conductance as a function of the barrier gate and dc source-drain (SD) bias, highlighting the resonant tunneling peaks  $a_1$ ,  $b_1$  and  $c_1$  of the three donors. From Tan *et al.*, 2010.

dopant atoms into nano-scale transistors from the source and drain regions. However several groups have concentrated on adapting the industry standard technique of ion implantation to implant single dopants into a silicon device in a controlled manner (Batra *et al.*, 2007; Bielejec *et al.*, 2010; Jamieson *et al.*, 2005; Schenkel *et al.*, 2003; Seamons *et al.*, 2008; Shinada *et al.*, 2008; Weis *et al.*, 2008). There are three main limitations to applying the technique to scalable single atom architectures: the ability to register individual ion strikes, the overall spatial registration of the ion implant site and subsequent straggling of the ion due to the statistical nature of the stopping process. Once the dopants are implanted a rapid thermal anneal at high temperature is needed to repair the damage and activate the donors, causing diffusion and segregation of dopants (Park *et al.*, 2004). Despite these concerns silicon nanoscale transistors have been fabricated with a low density of local area implants where it has been possible to tune individual dopants into resonance and observe transport spectroscopy through a single dopant, such as a P donor in Fig. 47 (Tan *et al.*, 2010). More recently single dopant implantation has been demonstrated into the channel of a silicon nanoscale metal-oxide-semiconductor field-effect-transistor (Johnson *et al.*, 2010; Shinada *et al.*, 2011). In the work by Johnson *et al.* (2010) FinFET devices were fabricated using SOI with 20nm of Si on a 145nm thick buried oxide, giving nominal channel dimensions of  $25 \times 70 \times 20$  nm. Using 14 keV there was a 57% chance of a  $P^+$  ion stopping within the channel region. The im-

plant resulted in an increase in charge in the buried oxide, causing a shift in threshold voltage and an increase in series resistance consistent with the introduction of Frenkel pairs in the channel. In the more recent work of Shinada *et al.* (2011) donors were placed in a 1D array allowing the regime between single electron tunneling and Hubbard band formation due to inter-dot coupling to be investigated.

There are 3 different regimes for single dopant transport experiments. In the first the channel current is influenced by the presence of a neutral or charged dopant. Ono *et al.* (2007) identified a single acceptor that modified the current through a FET depending on its charge state and refined this technique with a dual gate device to realize acceptor mapping (Khalafalla *et al.*, 2009; Ono *et al.*, 2008). In the second regime there is direct transport through a dopant in the access region to a FET channel (Calvet *et al.*, 2007a,b; Hofheinz *et al.*, 2006a). This allowed the study of electric field and strain effects on the acceptor (Calvet *et al.*, 2007a,b) and the Zeeman splitting (Hofheinz *et al.*, 2006a) of the donor ground state. The third regime, representing the most direct way to access information about the properties of a dopant and its environment, is direct transport through the dopant states in the sub-threshold extreme of a transistor. Due to the progress in device scaling this was recently realized in ultra-scaled MOSFET devices by (Pierre *et al.*, 2010; Sellier *et al.*, 2006; Tan *et al.*, 2010). All three transport regimes are illustrated in Fig. 48 and will be discussed in more detail in the remaining part of the sub-section.

Sellier *et al.* (2006) demonstrated transport through a donor in a nano-FET and identified excited states as well as the doubly occupied  $D^-$  state confirmed by magneto transport (regime 3). The ionization energy observed in this work was consistent with As as expected from indiffusion from the source and drain region. In contrast to the ionization energy of the  $D^0$  state, which was similar to bulk, the ionization energy of the  $D^-$  state was enhanced. This reduction in the charging energy, i.e. an increase in  $D^-$  ionization energy at an unchanged  $D^0$  ionization energy, is discussed in comparison to several experiments in Sec. V.C.2. Lansbergen *et al.* (2008) analyzed the orbital spectrum based on nonlinear transport and studied the impact of the electric field and gate interface on the donor state. They analyzed the data in comparison to a large scale atomistic model and found good agreement even though the spectrum is strongly altered from the bulk. Tan *et al.* (2010) demonstrated transport spectroscopy on a transistor that was implanted with 3 donors based on a timed exposure, thus the first experiment on an intentionally placed group of donors. The intentional placement is confirmed by a sample that was not implanted and did not show any resonances. As expected the donor peaks show a paramagnetic Zeeman shift of the  $D^0$  state and the opposite for the  $D^-$  state.

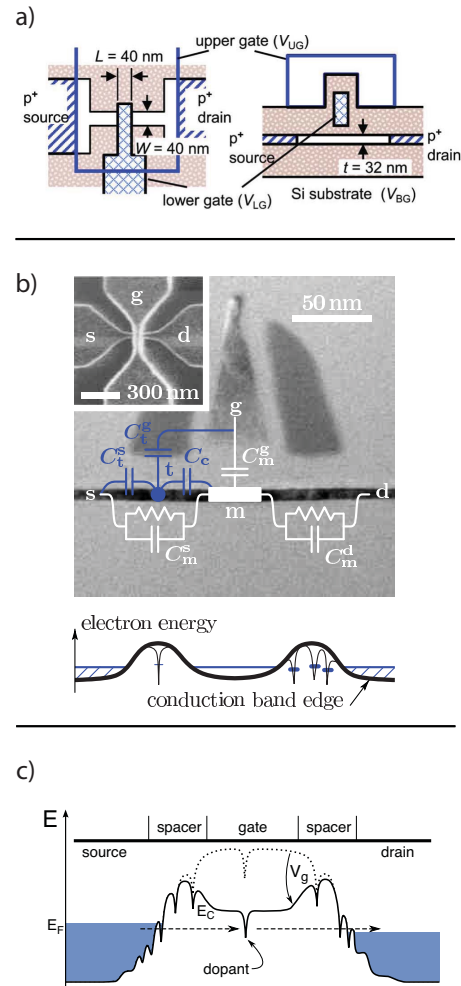


FIG. 48 Three examples of device layouts that illustrate different transport regimes for the detection of a single dopant: (a) Capacitive coupling to the channel which leads to a modification of the channel current due to the charge state of a dopant. (b) Tunneling through a dopant in the access region in series with transport through the channel. (c) Direct tunneling through a dopant in the channel in the sub-threshold regime. From (a) Ono *et al.*, 2007, (b) Hofheinz *et al.*, 2006a, (c) Sellier *et al.*, 2006.

Spectroscopic measurements combined with device based modeling led to a detailed understanding of the valley-orbit coupling of donor or dot states (Rahman *et al.*, 2011c) and the two electron state of a donor (Lansbergen *et al.*, 2011; Rahman *et al.*, 2011a) which are discussed in detail in the next section. Recently, Pierre *et al.* (2010) linked low temperature resonant transport through donor states to the room temperature performance of a MOSFET. They performed a statistical analysis of the threshold voltage of ultra-short channel FinFETs (less than 20 nm). Transistors with a threshold voltage far below the average display resonant transport at low temperature due to a donor in the middle of the channel, as shown in Fig. 50. This direct link between

the room temperature variability and the low temperature spectroscopy represents an important contribution to device engineering (Wacquez *et al.*, 2010).

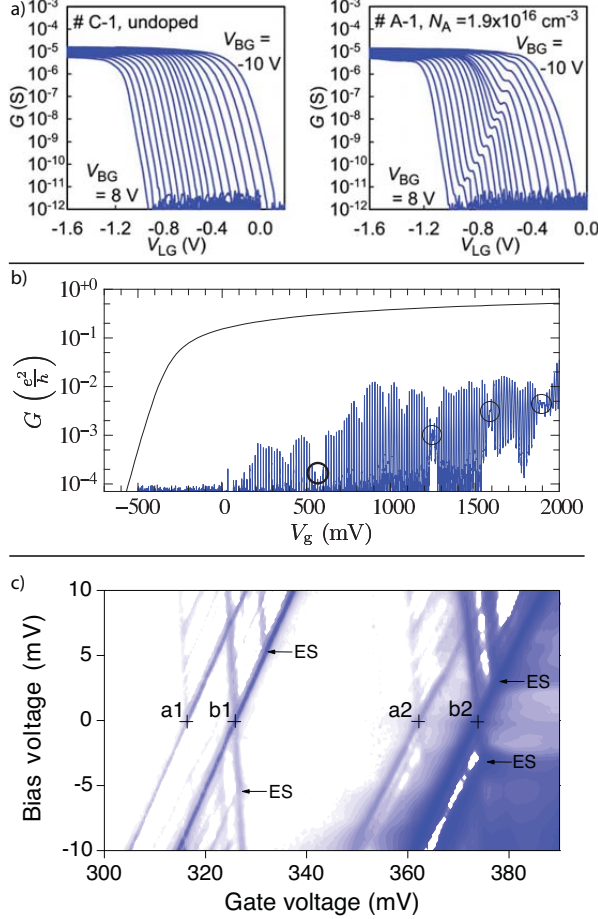


FIG. 49 **Three-dopant transport regimes in a transistor geometry:** An example of the dopant detection regime based on the capacitive coupling the the channel is shown in (a) for an undoped (left) and doped (right) double gate sample. The signature of a single acceptor charging event is evident in the doped sample (Ono *et al.*, 2007). An example of the access region where the dopant is in the barrier of the access region in series with a quantum dot is shown in (b) Hofheinz *et al.*, 2006a (thick black line represents to room temperature FET characteristics and the line below the low temperature Coulomb blockade). The third regime with direct transport through a dopant in the sub-threshold limit is shown in (c) (Sellier *et al.*, 2006). From (a) Ono *et al.*, 2007, (b) Hofheinz *et al.*, 2006a, Sellier *et al.*, 2006.

Hofheinz *et al.* (2006a) reported transport through a donor in the access region of a small MOSFET (regime 2). The access region is part of the channel that has a weaker coupling to the gate which leads to a barrier in the band structure, as shown in Fig. 48b. They observed sequential transport through the donor and through a localized state between the two barriers of the access region which has a much lower charging energy. Magnetotransport revealed a Zeeman shift of the resonance consistent

with a paramagnetic trap. The complex interaction between a single electron transistor and a dopant was only recently explained in detail (Golovach *et al.*, 2011). Calvet *et al.* investigated acceptors in the barrier of a Schottky FET. They observed a Zeeman shift of the acceptor and analyzed the impact of the electric field on the acceptor (Calvet *et al.*, 2007b) and the effect of local strain (Calvet *et al.*, 2007a).

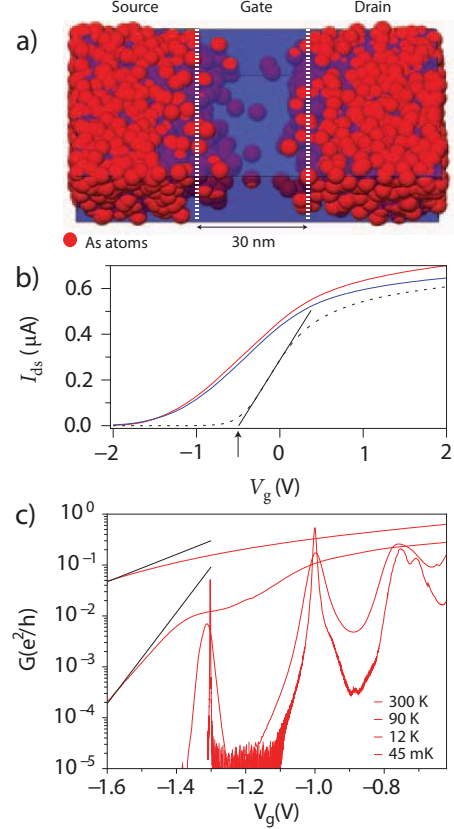


FIG. 50 **Direct tunneling through a dopant in a short channel FET:** The illustration (a) shows a Monte Carlo simulation of the doping profile in a 20nm channel where some dopants diffused into the channel region from the source and drain. (b) The dashed curve shows the current averaged over many devices where the black line indicates the threshold. Two devices show a drastically lower threshold that is linked to a resonant transport at low temperature as indicated in (c) for the device with the lowest  $V_{th}$ . From Pierre *et al.*, 2010. This data shows the clear connection between the low threshold of these devices at room temperature and the resonant transport at low temperature, both mediated by a single dopant.

As mentioned before, single dopants can not only be detected by passing current through them but also by their electrostatic coupling to free electrons in the channel (regime 1). Khalafalla *et al.* (2009) developed earlier single gate experiments (Ono *et al.*, 2007) to a multi-gate configuration. Two overlapping top-gates allowed the modulation of the channel potential profile. This made it possible to define the position of a donor along

the length of the channel which led to the observation that an acceptor close to the source has the largest impact on transport. This device geometry has been further developed to allow for charge pumping based on a small number of dopants which is attractive due to the large charging energy of the dopant and its potential for high accuracy as current standard (Lansbergen *et al.*, 2012). A double gate study of n-type channels revealed a clear difference between doped and undoped devices. In undoped devices the back gate simply shifts the threshold voltage of the device. Devices of the same geometry with  $2 \times 10^{18} \text{P cm}^{-3}$  show many sub-threshold resonances with a large charging energy and a different coupling to the top gate Verduijn *et al.* (2012). Furthermore, coupling between some of these is observed. These observations close the loop between the randomly- and deterministically-doped devices.

Until recently single donor transport was focused on sequential tunneling to probe the spectrum of a donor. Recently, several coherent transport experiments with single donor and double donor systems have been reported. Strong coupling to the contacts leads to the formation of a Kondo ground state where the parametric donor state is screened leading to transport in the traditional Coulomb blocked one electron region (Lansbergen *et al.*, 2010). The valleys play a key role in Si Kondo physics as theoretically predicted (Shiau and Joynt, 2007; Shiau *et al.*, 2007) and experimentally confirmed for donors by the presence of spin and orbital Kondo and their combination (Lansbergen *et al.*, 2010; Tettamanzi *et al.*, 2012). Furthermore, quantum interference between two tunneling paths has been discussed by (Calvet *et al.*, 2011; Verduijn *et al.*, 2010) in the context of a Fano resonance. Dopants present an ideal platform to investigate the crossover from scale-less mesoscopic effects to atomistic transport.

### 3. Single dopants in crystalline silicon

An alternative technology has been developed to place dopants in silicon with atomic precision using a scanning probe microscope. Ever since its invention in 1981 by Binnig and Rohrer, the STM has gained international recognition by not only its capability to image surfaces with unprecedented resolution but also by its potential to modify and pattern crystalline surfaces at the atomic scale. Amongst the most notable examples are the formation of the letters IBM with individual xenon atoms on a nickel surface by Eigler's group (Eigler and Schweizer, 1990).

The translation of this technology to manipulate atoms in silicon was, however, not simple due to the strong, covalent nature of silicon bonds. To position atoms in silicon it was necessary to use a lithographic process, analogous to conventional optical/e-beam lithography. Here a

monolayer of hydrogen resist is patterned using the tip of the STM to create an atomic-scale template. In the early 1990s Lyo and Avouris (1990) and Lyding *et al.* (1994) proposed the use of such a template to create a pattern of highly reactive dangling bonds sites on the silicon surface which could subsequently be functionalized with various atomic and molecular species.

The process of STM hydrogen lithography has since been adapted to realize a complete fabrication strategy for atomic-scale silicon device fabrication (Ruess *et al.*, 2005, 2004; Simmons *et al.*, 2005). Here dopants are placed in the silicon crystal with atomic precision laterally using scanning probe techniques and atomic precision vertically with molecular beam epitaxy (MBE). The important feature of these devices is that, in contrast to modern CMOS devices and almost all quantum semiconductor devices, which use many materials and have heterogeneous interfaces, STM-patterned devices are formed in single crystal silicon. Confinement of electrons is thus achieved by atomically abrupt changes in the density of dopant atoms within the silicon crystal. The doped regions can have very high planar electron densities in the range  $n_{2D} \approx 2.5 \times 10^{14} \text{ cm}^{-2}$ . In three dimensions this density corresponds to a value  $\approx 10^{21} \text{ cm}^{-3}$ , three orders of magnitude above the Mott metal-insulator transition. At these high carrier densities one in every four silicon atoms is substituted with a phosphorus atom, so that the average separation of phosphorus atoms is  $< 1 \text{ nm}$ , much smaller than the single dopant Bohr radii ( $a_B \approx 2.5 \text{ nm}$ ). As a consequence the doped regions are highly conducting and behave like a disordered metal. Electron transport has been studied in these highly doped single crystal donor-based quantum wires (Ruess *et al.*, 2008, 2007a,b) and recently this technique has been used to realize conducting wires in silicon with Ohmic behavior down to the atomic-scale (Weber *et al.*, 2012).

It is also possible to pattern more complex devices, such as atomically abrupt, epitaxial quantum dots with 1D source and drain leads (Fuechsle *et al.*, 2010; Fuhrer *et al.*, 2009). These studies have allowed the impact of vertical and lateral confinement on silicon quantum dots to be investigated. In such abruptly confined quantum dots very small energy level splittings of  $\approx 100 \mu\text{eV}$  have been observed in electron transport and attributed to transport through the valley states of a few-electron quantum dot, as shown in Fig. 51 (Fuechsle *et al.*, 2010). STM images of the device in Fig. 51(a,b) show the central region of the device into which  $6 \pm 3 \text{ P}$  atoms are laterally confined with the STM. These dopants are also strongly vertically confined by low temperature silicon molecular beam epitaxy. The corresponding stability diagram shown in Fig. 51(c,d) reveals spacing in the energy spectrum of order  $\approx 100 \mu\text{eV}$ . This very small energy level splitting was surprising given the ultra-small size ( $\sim 4 \text{ nm}^2$ ) of the quantum dot. However it is well known that strong lateral and vertical confinement breaks the degen-

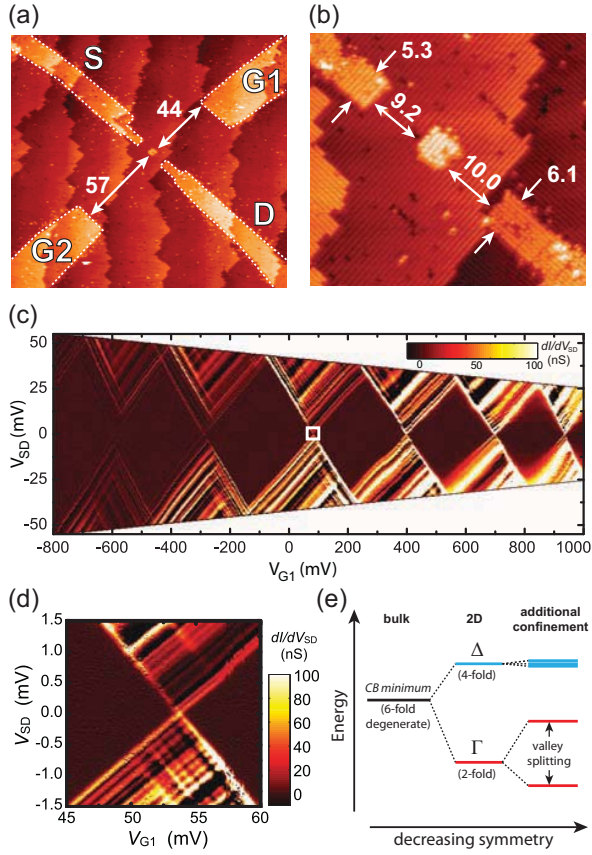


FIG. 51 **Few-electron quantum dot:** (a) An STM image of the central device region of a few-electron single crystal quantum dot acquired during hydrogen lithography, showing a four terminal device with source (S), drain (D) and two in-plane gates (G1,G2). The bright regions correspond to areas where phosphorus donors will be incorporated. (b) A close-up showing the central quantum dot which contains  $6 \pm 3$  donors. (c) The stability diagram showing the conductance,  $dI/dV_{SD}$  through the dot as a function of gate voltage,  $V_G$  and bias voltage  $V_{SD}$ . (d) A close-up of the transition (white square in Fig. 51c) revealed a high density of conduction resonances with an average energy spacing of  $\approx 100\mu\text{eV}$ . (e) The 6-fold degeneracy of the conduction band minima of bulk silicon is lifted by confining the electrons vertically to two dimensions and is then split again by abrupt, lateral confinement. From Fuechsle *et al.*, 2010.

eracy of silicon valley states.

This is illustrated in Fig. 51(e) where electrons strongly confined in a two-dimensional plane result in splitting of the 6 bulk valleys into 4 degenerate  $\Delta$ -pockets as well as two  $\Gamma$ -pockets at  $k = 0$ . The remaining degeneracies can be broken in the presence of sharp lateral or vertical confinement. In these highly doped  $\delta$ -layers strong, abrupt quantum confinement in  $z$ -direction splits the degeneracy of the out-of-plane  $\Gamma$ -bands to give the lower energy  $\Gamma_1$  and  $\Gamma_2$  bands. In addition, there are four  $\Delta$ -valleys, two each in the  $x$  and  $y$  directions, which are usually degenerate in 2D devices. However, since the quantum dot device

is also confined laterally on the nm-scale valley splitting of these states is also observed. It is this valley splitting that gives rise to the  $\approx 100\mu\text{eV}$  energy level separation observed experimentally in STM-patterned few-electron quantum dots. This contrasts to studies of other few-electron quantum dot systems, where it is the large size of the dot itself that gives rise to  $\approx 100\mu\text{eV}$  (Beenakker, 1991).

It should be noted also that now the source and drain leads to these abrupt quantum dots are not 2D reservoirs but 1D leads. This also results in the formation of resonant tunneling features due to the presence of 1D subbands. The energy separation of these subbands depends on the width of the 1D leads and for this device was found to be  $\sim 10$  meV. Such 1D states have also been observed in other silicon-based quantum dots (Lim *et al.*, 2009b; Möttönen *et al.*, 2010) and a recent review discusses how to distinguish these in electron transport (Escott *et al.*, 2010).

Using such a technology it is also possible to pattern individual dopants in silicon with atomic precision (Schofield *et al.*, 2003; Wilson *et al.*, 2004) to realize single dopant atom transistors, as shown in Fig. 52(a) (Fuechsle *et al.*, 2011). The critical features of this device are that the dopant, the source-drain leads and the control gates are crystalline and all exist within one plane of the silicon crystal, as shown in Fig. 52(b). The encapsulation of this device in epitaxial silicon removes the confined dopant states away from the influence of surfaces and interfaces. However transport devices by definition also contain electrodes, and these electrodes are known to have profound effects on the energetics of the single dopant atom. In these epitaxial architectures the electrostatic potential at the dopant could be tuned using two in-plane gates G1 and G2 patterned either side of the transport channel defined by the S and D leads.

Fig. 52(c) presents the measured stability diagram of the single donor, in which the three charge states of the donor can easily be identified: the ionized  $D^+$  state, the neutral  $D^0$  state and the negatively charged  $D^-$  state. The diamond below  $V_G \approx 0.45\text{V}$  does not close, as expected for the ionized  $D^+$  state, because a donor cannot lose more than its one valence electrons. The conductance remains high (on the order of microsiemens) down to the lower end of the gating range, making the possibility of additional charge transitions unlikely. The  $D^+ \rightarrow D^0$  charge transition occurred reproducibly at  $V_G \sim 0.45 \pm 0.03\text{V}$ , as shown in Fig. 52(d) for multiple cool-downs and is attributed to the high stability of the device and the inherent influence of the nearby electrodes on the position of the donor eigenstates relative to the Fermi level of the leads.

To understand quantitatively how the nearby transport electrodes affected the electronic properties of the donor, the electrostatic potential landscape of the innermost part of the device was calculated, treating the



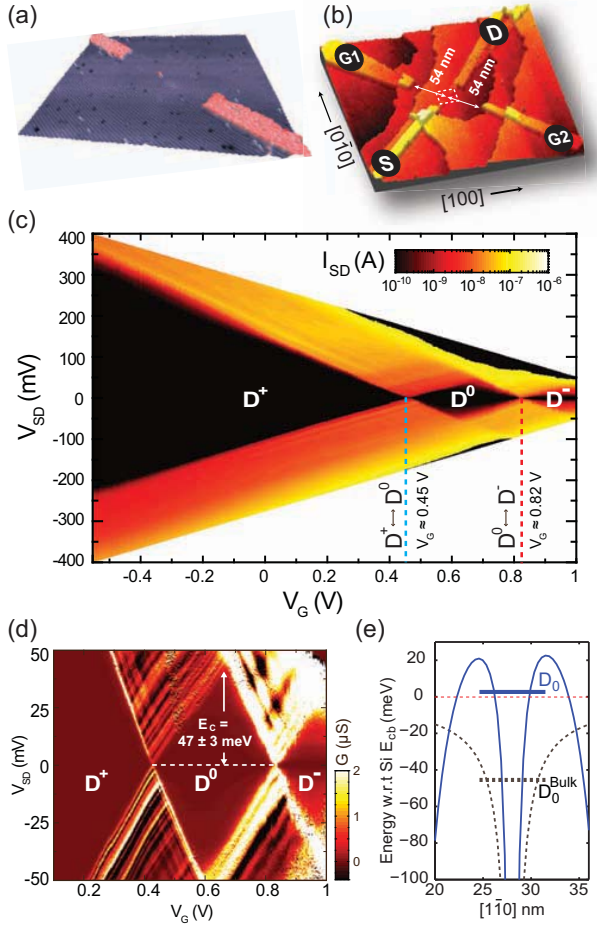


FIG. 52 **A single-atom transistor.** (a) 3D perspective scanning tunnelling microscope (STM) image of a hydro-gated silicon surface. Phosphorus will incorporate in the red shaded regions selectively desorbed with a STM tip to form electrical leads to a single phosphorus atom patterned precisely in the centre. (b) the source (S), drain (D) and two gate leads (G1, G2) to the central donor, which is incorporated into the dotted square region. (c) The electronic spectrum of the single-atom transistor, showing the stability diagram with the drain current  $I_{SD}$  (on a logarithmic scale) as a function of source-drain bias  $V_{SD}$  and gate voltage  $V_G$  (applied to both gates). (d) The differential conductance  $dI_{SD}/dV_{SD}$  (on a linear scale) as a function of  $V_{SD}$  and  $V_G$  in the region of the  $D^0$  diamond shown in (c). (e) A comparison of the potential profile between the source and drain electrodes in this device (blue line) to an isolated bulk phosphorus donor (dashed grey line), where the  $D^0$  state resides 45.6 meV below  $E_{cb}$ . In contrast, the  $D^0$  state in the single-atom transistor resides closer to the top of the potential barrier. From Fuechsle *et al.*, 2011.

heavily doped gate regions in a self-consistent atomistic approach using a Thomas-Fermi approximation. Having established the electrostatic potential of the device, the donor electronic states were then calculated using a tight-binding approach (Lansbergen *et al.*, 2008). The position of the resulting one-electron ground state  $D^0$  for the solitary phosphorus dopant is depicted in Fig. 52(e)

(blue line). As expected, due to the electrostatic environment, the energy levels of the device are raised significantly from the bulk case (dashed grey line), where the unperturbed Coulombic donor potential asymptotically approaches the silicon conduction band minimum  $E_{cb}$  (red dashed line) and  $D^0$  has a binding energy of  $E_B \approx -45.6$  meV. In contrast,  $D^0$  in the effective donor potential of the single donor transport device resides much closer to the top of the barrier (solid line) along the S-D transport direction. Despite this, the charging energy  $E_C$  could be extracted from the transport data and was found to be  $47 \pm 3$  meV, remarkably similar to the value expected for isolated phosphorus donors in bulk silicon ( $\approx 44$  meV) (Ramdas and Rodriguez, 1981).

These results are in sharp contrast to previous experiments on single dopant in silicon transport devices, which have reported charging energies that significantly differ from the bulk case (Lansbergen *et al.*, 2008; Pierre *et al.*, 2010; Rahman *et al.*, 2011a). There, the difference was attributed either to screening effects resulting from strong capacitive coupling to a nearby gate (Lansbergen *et al.*, 2008) or strong electric fields (Rahman *et al.*, 2011a), or to an enhanced donor ionization energy in the proximity of a dielectric interface (Pierre *et al.*, 2010). Importantly, these effects are small for a single phosphorus dopant, which is symmetrically positioned between two gates, encapsulated deep within an epitaxial silicon environment.

### C. Discussion

A dopant in a semiconductor represents the ultimate limit of a quantum dot. In contrast to a quantum dot the confinement potential is given by the three dimensional Coulomb potential of the dopant ion (see section II) and not by external gates. In quantum dots the orbital energy is small and mainly probed as the energy difference between the triplet and single states in the two electron problem. The dopant has hydrogenic level spectrum with splittings in excess of 10 meV. The valleys in Si lead to interesting corrections due to the restricted momentum space of these states. Again in strong contrast to a quantum dot, the confinement potential of a dopant is strongly altered by the amount of charge on the dopant. A shallow impurity can only bind two electrons where the 2nd charging energy for the 2nd electron is almost the ionization energy of the first, i.e.  $H^-$  like the two electron state is very close in energy to the continuum. Here we compare the physical properties of the dopant confined states for the different devices. The orbital spectrum of a gated donor is illustrated followed by a discussion of the charging energy between the one and two electron state. Finally, we look at the interaction between the donor and the leads and the interaction between two donors.

## 1. Orbital structure of a dopant in a nanostructure

In section III.C the spectrum and orbital structure of a bulk dopant were discussed. A dopant in a nanostructure possesses not necessarily these properties as already calculated by Macmillan and Landman (1984). The environment in a nanodevice has a large impact on the orbital spectrum of a donor. An electric field will lift degeneracies (Friesen, 2005; Smit *et al.*, 2004) and a triangular well, e.g. due to a gate, lowers the excited states of the dopant due to the interaction with the interface well (Calderón *et al.*, 2007; Martins *et al.*, 2004). These theoretical predictions have been experimentally confirmed in the interface (Lansbergen *et al.*, 2008) as well as the bulk regime (Fuechsle *et al.*, 2011). Critically important for the ability to model the devices and obtain metrology data with respect to impurity type and depth, was the ability to compute the excited state spectra as well as the ground state spectra in NEMO3D, see Appendix C. The earlier cited effective mass models offer key physical insight into the problem and go hand in hand with the tight-binding work which generates accurate predictions to interpret the experimental data.

The environment, i.e. the leads, an interface to a gate, or an electrical field, can drastically alter the orbitals of a dopant in comparison to the unperturbed bulk condition. Lansbergen *et al.* (2008) measured the energy spectrum of single donors, located in the channel of FinFETs by transport spectroscopy, Figure 53(a). They were not bulk like but agreed well with a multimillion atom simulations of the complete system. In conjunction with the data, the theoretical analysis allowed the authors to identify the species of the donors (As) and furthermore provided an explicit determination of the degree of gate-controlled quantum confinement in each device. Figure 53(b) shows the 3 confinement regimes that can be distinguished: Coulomb, hybridized, and interfacial confinement with the charge density and schematic potential landscape for these three regimes. At low electric fields the electron is located at the donor site and its ground state corresponds to a donor in bulk (thus full lattice symmetry). At high electric fields the electron is pulled inside the triangular potential well at the interface reducing the symmetry of the system. The electron is still localized near the donor site in the lateral directions though, in correspondence with the results of Calderón *et al.* (2007). At the crossover between these regimes, the electron is delocalized over the donor- and well-sites.

Donors in devices fabricated with the STM, as discussed in sub-section V.B.3, exhibit a more bulk like orbital spectrum (Fuechsle *et al.*, 2011). This is due to the fact that in these devices the donor is far away from a dielectric interface and the gate does not create large fields in comparison with MOSFET structures (Lansbergen *et al.*, 2008). Fuechsle *et al.* (2011) also showed that the charging energy of a dopant in an STM fabricated

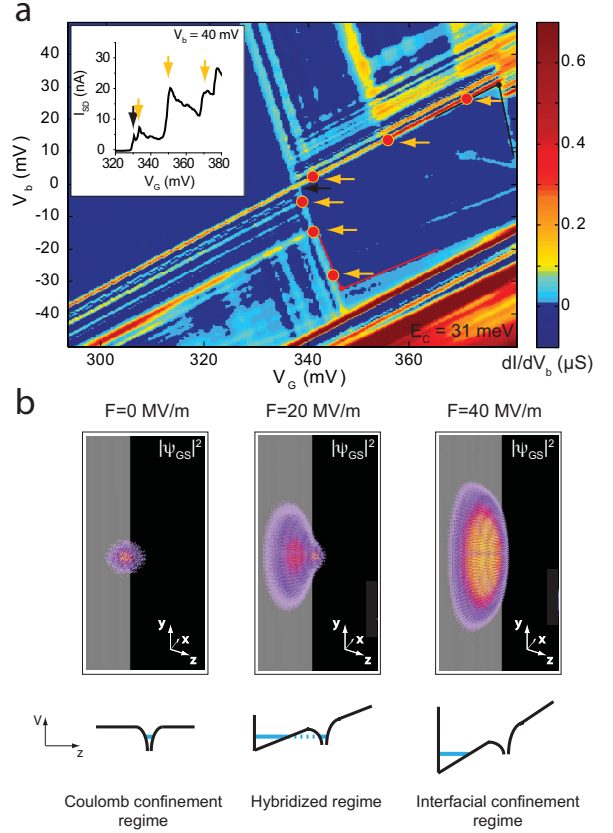


FIG. 53 **Excited-state spectroscopy data of single gated donors based on transport spectroscopy:** (a) Source/drain differential conductance of a dopant in a FET. Excited states are indicated by the red dots and yellow arrows. Inset in (a) shows source/drain current as a function of gate voltage at  $V_b = 40$  mV where each plateau indicates an addition quantum channel due to an orbital. (b) Simulations of the gated donors eigenstates: wave function density of the  $D^0$ -ground state ( $|\Psi_{GS}|^2$ ) located 4.3 nm below the interface in the three different electric field regimes; Coulomb confinement regime,  $0 \text{ MV m}^{-1}$  (left), hybridized regime,  $20 \text{ MV m}^{-1}$  (middle) and interfacial confinement regime,  $40 \text{ MV m}^{-1}$  (right). The grey plane indicates the Si/SiO<sub>2</sub> interface. From Lansbergen *et al.*, 2008.

device is comparable to the bulk value. This is to be expected for an environment that is close to bulk besides the source and drain electrodes with a cross-section of only a few square nanometers.

## 2. Charging energy of a dopant in a nanostructure

In the constant-interaction model (Beenakker, 1991) the charging energy of a Coulomb island is independent of the number of electrons localized on the charge island ( $N$ ). This assumption is valid as long as the confinement potential is not affected by  $N$  which is not at all the case for isolated donors. For shallow donors, only a

single charge transition ( $N = 1 \rightarrow N = 2$ ) plays a role since it is not possible to bind a 3rd electron. The addition of a single electron to an ionized donor site will screen the positive nucleus and thus strongly alter the confinement potential for an additional electron. The Coulomb interaction between an electron on the donor and all other electrons in its environment can still be parameterized by a single capacitance  $C$ , which is specific to  $N$  and the environment of the donor. The charging energy, represented by  $e^2/2C$ , of donors close to a gate interface is modified due to the screening at the interface as well as the applied electric field which was experimentally demonstrated by Lansbergen *et al.* (2008). Fuechsle *et al.* (2011) showed that a STM fabricated single dopant device displays an unaltered charging energy consistent with the bulk-like environment. Recent theoretical work addresses this problem and progress has been made using effective mass (Calderón *et al.*, 2010b; Fang *et al.*, 2002; Hao *et al.*, 2011; Hollenberg *et al.*, 2004) as well as self-consistent field tight-binding (Rahman *et al.*, 2011a) treatments.

### 3. Interactions between donors

The interaction between donors plays a central role in quantum information science. The goal is to achieve tunable interaction that preserves coherence (Kane, 1998). This has not been achieved yet but it is within reach. Initial experiments have focused on the study of capacitive coupling as well as the coherent coupling between dopants. A detailed understanding of tunnel coupling as well as capacitive coupling between a donor and a SET is a key issue since this is the central read-out mechanism for qubits (Morello *et al.*, 2009). This complex coupling between a dopant and a quantum dot, i.e. a semiconductor SET, has been analyzed in detail in an experimental and theoretical effort by Golovach *et al.* (2011). Coherent coupling between dopants has been achieved in the limit of weakly coupled dopants (Verduijn *et al.*, 2010) and strongly coupled dopants (Calvet *et al.*, 2011). Both rely on the interference between two coherent transport channels which leads to a specific line shape (Fano, 1961) that is sensitive to the phase difference between the two transport paths. This phase difference can be modified by changing the magnetic flux that is enclosed in the loop of the transport paths. Verduijn *et al.* (2010) studied two As atoms in a nano MOSFET and showed that the distance between the dopants is about 30 nm based on the magnetic field dependence. Calvet *et al.* (2011) studied acceptors in a Schottky FET and also observed a Fano resonance which proves coherent exchange of electrons. The lack of magnetic field dependence confirms their expectation that the acceptors studied are strongly coupled in these devices.

### D. Double dopant quantum dots

The study of transport and interactions in donor-based double quantum dots has been motivated by their potential for solid state quantum computing applications (Loss and DiVincenzo, 1998; Taylor *et al.*, 2005). Initial studies concentrated on ion-implanted devices, where both independent gate control (Hudson *et al.*, 2008) on the dot occupancies and charge detection using surface aluminum SETs were demonstrated (Mitic *et al.*, 2008) in multi-donor devices which contained hundreds of dopants in each dot. Characteristic honeycomb structures (see section IV.F) were observed in the charge stability maps. However difficulty was encountered going to smaller dot sizes due to the inherent straggling in the ion implantation process. Non the less, sequential transport through a stochastically doped FinFET structure has been demonstrated by (Roche *et al.*, 2012). They used a split gate geometry to independently control the chemical potential of two dopants and probe the excited states by tunneling spectroscopy in a similar manner to a double quantum dot, as shown in Fig. 54.

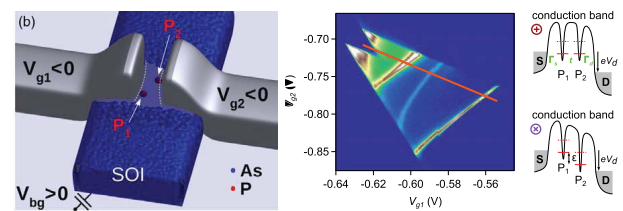
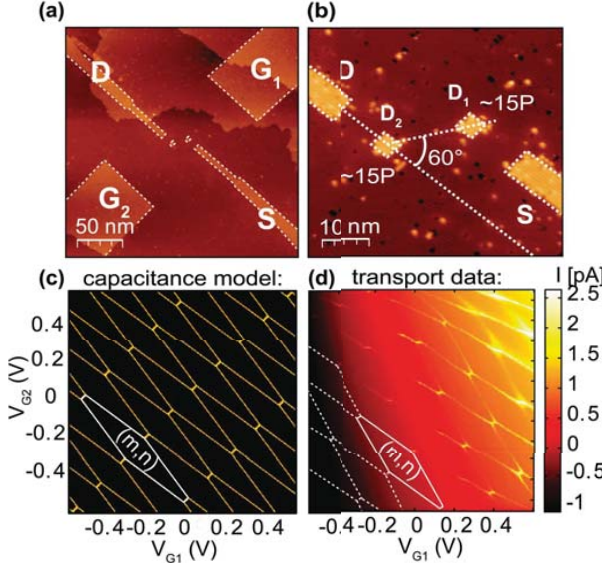


FIG. 54 **Sequential transport through a double donor device with independent gate control.** The left panel shows the two opposing gates similar to a conventional FinFET geometry but with a split gate. The channel received a background doping of  $10^{18}$  P /  $\text{cm}^{-3}$  and this device demonstrates independent gate control of two dopants. The right panel shows a finite bias dual gate stability diagram revealing bulk-like excited states of the dopant. From Roche *et al.*, 2012.

Few-electron single-crystal quantum dots have recently been realized using STM-patterned devices, as shown in Fig. 55. Here independent electrostatic control of the ultra-small dots was achieved by careful modeling and optimization using the capacitance modeling tool FASTCAP (Nabors and White, 1991) and a single-electronics modeling tool (SIMON) (Wasshuber *et al.*, 1997). This is quite remarkable given the small physical size of the dots ( $\sim 4$ nm in diameter) and their close spacing ( $\sim 10$  nm). At such small dimensions cross-capacitances between the quantum dots become considerable and the dots need to be positioned at an angle,  $\alpha \sim 60^\circ$  with respect to one another to achieve independent electrostatic control. One of the advantages with donor-based quantum dots is that this combination of device modeling and precision lithography using scanning probe microscopy allows reliable predictive device design, an important tool as

devices scale to the single donor level.



**FIG. 55 A donor-based double quantum dot in silicon:** (a) An overview STM-image of the device showing the two quantum dots, tunnel-coupled to the source and drain (S/D) leads and capacitively coupled to the gates G1(2). (b) Close-up of the two quantum dots, 4nm in diameter. The DQD angle  $\alpha = (60 \pm 3)$  has been optimized for maximum electrostatic control whilst suppressing parallel leakage through the dots. The modeled (c) and measured (d) charge stability diagrams show excellent agreement, demonstrating independent electrostatic control of the individual dots. From Weber, 2012.

### E. Charge sensing in few-electron dopants

Following the principal work by Field *et al.* (1993) on remote sensing of charge using a quantum point contact in a AlGaAs/GaAs system, Elzerman *et al.* (2004) adapted this technique to perform single shot detection of spin dependent single electron tunneling events in a single electron quantum dot. Real time sensing of single electron tunneling is fundamental to electrical read-out of qubit states in spin quantum computing. In these experiments (Elzerman *et al.*, 2004) a quantum point contact was capacitively coupled to the qubit. However the visibility, and therefore fidelity of spin read-out, of these charge detectors is greatly enhanced when a single electron transistor rather than quantum point contact is used as a charge detector (Morello *et al.*, 2009). Here the SET is additionally tunnel-coupled to the qubit and electrons can be loaded from the SET-island itself, thus eliminating the need for a separate electron reservoir.

High-fidelity spin read-out of a P-donor-bound electron in Si has recently been demonstrated within this architecture (Morello *et al.*, 2010) by implanting a small number of P donors in the vicinity of an electrostatically in-

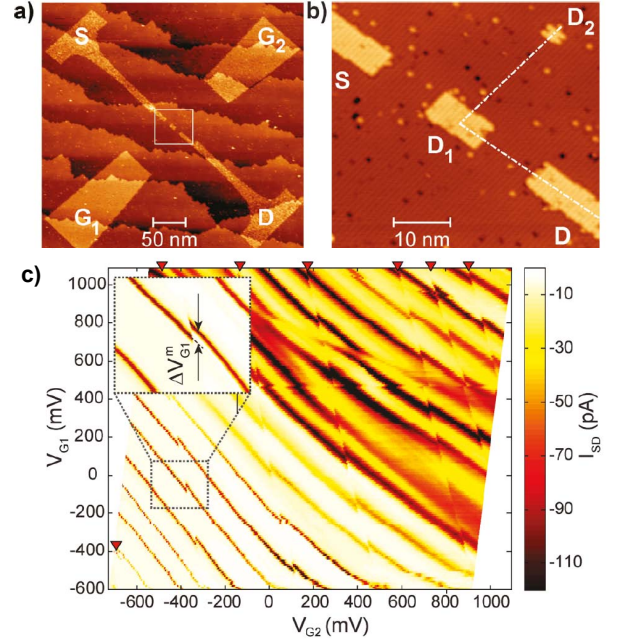


**FIG. 56 Charge sensing using a donor-based single electron transistor coupled to a small donor dot:** (a) Filled-state STM image of the overall device pattern, showing (in lighter contrast) the regions where the hydrogen resist monolayer has been desorbed to create the source (S) and drain (D) contacts of the single electron transistor, and the two gates (G1, G2). (b) High resolution image of the device pattern within the white box in (a), showing the SET-island (D1) and the quantum dot (D2) (c) Charge stability plot showing the dependence of  $I_{SD}$  on the gate voltages ( $V_{G1}$ ,  $V_{G2}$ ), for a constant  $V_{SD} = -50 \mu\text{V}$ . The high current lines correspond to the Coulomb peaks of the SET. Inset: High resolution map of a small section of (c) showing discontinuity of a current line, due to a particular charge transition of D2. The red triangles in the main map indicate a total of 7 such transitions of D2. From Mahapatra *et al.*, 2011.

duced SET, at the Si-SiO<sub>2</sub> interface. This has established the feasibility of fiducial detection of P-donor-based spins qubits, however the uncertainty in the number and position of the donors relative to the SET is of concern for scaling up to a practical 2D Si:P quantum computer with multiple donor arrays. To reproducibly achieve sufficient charge sensitivity and electron tunnel rates, it is important to precisely situate the SET with respect to deterministically positioned array of Si:P qubits. Towards this end STM-lithography has recently developed a charge detection device lay-out, wherein a SET charge sensor and an ultra-small quantum dot are both patterned on the same plane of a Si crystal, at an atomically-precise separation. In this way two of the key design parameters, i.e., the sensitivity of charge detection and electron tunnel rates can be made sufficiently high to enable projective spin readout of individual P donors in Si. Since the fabrication technique is essentially identical to the established approach for deterministic placement of P donors in Si,

this charge sensing layout can be readily integrated in scalable Si:P spin quantum computing architectures. Recent results demonstrated that single electron tunneling between the quantum dot and the SET island occurred on a time-scale ( $\tau \sim \text{ms}$ ) two-orders-of-magnitude faster than the spin-lattice relaxation time of a P donor in Si and suitable for projective readout of Si:P spin qubits (Mahapatra *et al.*, 2011). Single spin sensitivity is discussed in more detail in section VI.A.

## VI. OUTLOOK: RELAXATION, COHERENCE AND MEASUREMENTS

In the previous sections we have reviewed the quantum electronic properties of silicon, and how such properties can be harnessed in nanoscale structures. That field of research is fairly mature, partly thanks to its technological links with classical silicon nanoelectronics.

Once the confinement of a single electron in silicon has been achieved, it becomes possible to start exploring the properties of the spin of the electron. An exciting possible application is quantum computing (Ladd *et al.*, 2010), where the electron spin is used as a quantum bit (qubit) (Morton *et al.*, 2011). Another vast field of research is spin transport (Appelbaum *et al.*, 2007; Dash *et al.*, 2009) and spintronics (Awschalom and Flatté, 2007; Jansen, 2012; Žutić *et al.*, 2004), which we will not discuss in this review.

In this section we present a theoretical introduction to the behavior of electron spins confined in silicon, and a snapshot of the current state of experimental progress. The discussion below is meant to provide the reader with an outlook on the future direction of the field. A thorough review of spin control in silicon will only be possible several years from now.

### A. Spin relaxation and decoherence

The suitability of a physical system to encode and preserve quantum information is quantified by parameters such as the relaxation and coherence times. The first, called  $T_1$ , describes the timescale over which an energy-excited state decays to the ground state. The second, called  $T_2$ , describes the timescale over which the phase coherence between different branches of a quantum superposition can be preserved.

A spin  $S = 1/2$ , such as an electron spin confined in a Si structure by a natural or artificial potential, can be described by a  $2 \times 2$  density matrix  $\rho = |\psi\rangle\langle\psi|$ . The state vector  $|\psi\rangle$  belongs to a 2-dimensional Hilbert space with basis vectors  $|\downarrow\rangle, |\uparrow\rangle$ , normally chosen as the eigenstates of the spin operator  $S_z$  if a static magnetic field  $B_0 \parallel \hat{z}$  is applied. At thermal equilibrium, the diagonal elements of the density matrix are related by a Boltzmann fac-

tor  $\rho_{11}^{th} = \exp(-E_Z/k_B T)\rho_{22}^{th}$ , where  $E_Z = g\mu_B B_0$  is the Zeeman splitting. Therefore, the diagonal elements of  $\rho$  are related to the degree of spin polarization. After a perturbation involving exchange of energy with an external field or reservoir, the spin returns to equilibrium in a typical time scale  $T_1$ , e.g.  $\rho_{11}(t) - \rho_{11}^{th} \propto \exp(-t/T_1)$ .  $T_1^{-1}$  represents the spin-lattice relaxation rate.  $T_1$  measurements in bulk samples are performed by observing the timescale over which the thermal equilibrium is recovered after either an ‘inversion pulse’, which swaps the populations of the ground and excited spin states, or a ‘saturation comb’, which equalizes the populations. Section VI.C.3 discusses how to obtain the  $T_1$  of a single spin in a nanostructure from a measurement of the probability of detecting the spin excited state as a function of the waiting time after the excited state preparation.

A coherent superposition of the  $|\uparrow\rangle, |\downarrow\rangle$  basis states results in nonzero off-diagonal elements (‘coherences’)  $\rho_{12} = \rho_{21}^*$ . The preparation and manipulation of such coherent superpositions is at the heart of quantum information technology (Nielsen and Chuang, 2000), and relies on well-established techniques that belong to the vast field of magnetic resonance (Slichter, 1990). Even in the absence of energy exchange with the environment, the coherence may decay in time like  $\rho_{12}(t) \propto \exp[-(t/T_2)^\alpha]$ , where  $T_2^{-1}$  is the decoherence rate, and  $\alpha$  is an exponent that depends on the details and the dynamics of the environment coupled to the spin. For electron spins in solid state, a major contribution to decoherence is given by the hyperfine coupling between the electron and the surrounding nuclear spins. The nuclear spins exhibit complex dynamics, driven by the interplay of their mutual interactions and the coupling with the electron. The time fluctuations of the hyperfine field randomize the electron spin precession frequency and destroy its coherence.

Even in the presence of a perfectly static nuclear spin bath, a macroscopic ensemble of spins would exhibit a spread of precession frequencies as a consequence of inhomogeneity in the local magnetic field, caused e.g. by the difference in the instantaneous value of the local hyperfine field at every electron site. The resulting dephasing time  $T_2^*$  represents the timescale over which a free induction decay occurs, i.e. the vector sum of all the spins in the ensemble averages to zero. For a single spin, the free precession cannot be observed in a single experiment, and must be obtained through repetition averaging. Therefore, a  $T_2^*$ -process arises when the quasi-static value of the local magnetic field changes from one repetition to the next. The ‘true’ decoherence time  $T_2$  is obtained in the experiments by ‘refocusing’ the quasi-static inhomogeneity (in space, for a spin ensemble, or in time, for a single spin) of the magnetic field through a Hahn echo technique (Slichter, 1990).

The definitions and discussion above can be readapted to the case where a two-level system is obtained from the truncation of the Hilbert space of two exchange-coupled

spins (Levy, 2002; Petta *et al.*, 2005). The basis states then become the singlet and triplet states,  $|S\rangle = (|\uparrow\downarrow\rangle - |\downarrow\uparrow\rangle)/\sqrt{2}$  and  $|T_0\rangle = (|\uparrow\downarrow\rangle + |\downarrow\uparrow\rangle)/\sqrt{2}$ , and the energy splitting caused by the exchange interaction  $J$  replaces  $E_Z$  in the expressions above. This way to define spin-based two-level systems has been proposed to allow the control of the qubit purely by electrical means, i.e. without resorting to magnetic resonance techniques.

Relaxation and decoherence of spins in semiconductors has been the subject of intense research, and an accessible review is given in (Hanson *et al.*, 2007). Here we highlight the specific phenomena that arise in silicon, in particular due to the valley degeneracy of the conduction band.

The spin-lattice relaxation, i.e. the return of the diagonal elements of the spin density matrix to their equilibrium value, requires the coupling of the spin to a phonon reservoir. Silicon lacks piezoelectric effect, which is often the dominant source of spin-phonon coupling in III-V materials. The only type of phonons present in Si is the “deformation potential”, i.e. a local change in lattice spacing which propagates with wave vector  $q$ . A deformation potential phonon alters the band gap in an inhomogeneous and time-dependent way, with repercussions on the exact mixture of spin, valley and orbital nature of the electronic wave functions.

The relaxation rate  $T_1^{-1}$  is obtained in a ‘Fermi golden rule’ approach as:

$$T_1^{-1} \approx \frac{2\pi}{\hbar} |\langle \uparrow | \mathcal{H}_{e-ph;SO} | \downarrow \rangle|^2 N(E_Z) \quad (12)$$

where  $N(E_Z) \propto E_Z^2$  is the density of phonon states at the energy splitting  $E_Z$ , and  $\mathcal{H}_{e-ph;SO}$  is a Hamiltonian term that includes the electron-phonon interaction and the spin-orbit coupling. It should be noted that the electron-phonon interaction does not directly couple Zeeman-split *pure* spin states. However, a nonzero coupling is obtained if the true eigenstates contain admixtures of other orbital or valley states, mixed in by the spin-orbit interaction.

Another way to look at the problem – more familiar to the spin resonance community – is to think of the spin as being subject to an effective magnetic field, whose magnitude and direction can be modulated by a lattice phonon. Then  $T_1^{-1}$  is proportional to the spectral density, at frequency  $\omega_e = E_Z/\hbar$ , of the component of the phonon-induced fluctuating local field perpendicular to the spin quantization axis.

Let us recall a simple expression for the electron  $g$ -factor in a semiconductor (Kittel, 1963; Roth, 1960):

$$g \approx 2 - \frac{m}{m^*} \left( \frac{2\Delta_{SO,VB}}{3E_g + 2\Delta_{SO,VB}} \right), \quad (13)$$

where  $\Delta_{SO,VB}$  is the spin-orbit splitting of the valence band,  $E_g$  is the band gap,  $m$  and  $m^*$  are the free electron and the effective mass, respectively. In Si,  $\Delta_{SO,VB} \sim 40$  meV is relatively small, due to the small atomic number. The large band gap  $E_g = 1.12$  eV results in electron

$g$ -factors very close to 2. Accordingly, spin relaxation in Si is relatively slow, since the modulation of the  $g$ -factor due to phonon scattering is very small.

There are four main differences in the spin relaxation behavior between Si and III-V semiconductors such as GaAs (Blakemore, 1982): (i) Si has no piezoelectric effect, therefore only deformation potential phonons are present; (ii) Si has no bulk inversion asymmetry, therefore is immune from Dresselhaus spin-orbit coupling effects (Dresselhaus, 1955; Hanson *et al.*, 2007); (iii) The small atomic number and large band gap of Si produce a weak spin-orbit coupling; (iv) The physical mechanism and the magnetic field dependence of  $T_1^{-1}$  depends on the nature (valley or orbital) and the details of the excited states above the valley-orbit ground state.

### 1. Electron spin relaxation in donors

Let us consider first the case of a shallow donor such as P, As or Sb, where doublet and triplet valley-orbit excited states (see section III.B.2) lie  $\sim 10 - 15$  meV above the singlet (spin-degenerate) ground state. All of these 6 states share the same hydrogenic  $1s$  orbital nature, and lie well below the  $2p$  orbital states. In this situation, the dominant contribution to spin relaxation arises from valley effects, which can take two forms: (i) “valley repopulation” or (ii) “one-valley” mechanisms.

(i) “*Valley repopulation*”: within one valley, the  $g$ -factor of an electron is slightly different (anisotropic) for magnetic field parallel ( $g_{\parallel}$ ) or perpendicular ( $g_{\perp}$ ) to the valley axis. In the unperturbed  $1s$  singlet ground state of a donor, all 6 valleys contribute equally, and the overall  $g$ -factor of the donor-bound electron is isotropic. However, the local strain produced by a phonon has the effect of disrupting the symmetry of the 6 valleys, lowering certain valleys with respect to others. Now the  $g$ -factor may assume an anisotropic character, which can be interpreted as a phonon-induced modulation of the effective local field, with a component perpendicular to the spin quantization axis. The resulting relaxation rate becomes (Hasegawa, 1960):

$$T_1^{-1}(B, T) = f_{Si}(\theta, \phi) \frac{6}{5\pi} \left( \frac{g'\Xi}{3gE_{vo}} \right)^2 \times \left( \frac{1}{\rho\nu_t^5} + \frac{2}{3\rho\nu_l^5} \right) \left( \frac{g\mu_B B}{\hbar} \right)^4 k_B T, \quad (14)$$

$$= K_4 B^4 T. \quad (15)$$

Here  $\Xi$  is the deformation potential parameter (Bardeen and Shockley, 1950; Herring and Vogt, 1956), representing the energy shift of the valleys due to a deformation of the crystal lattice.  $g' = (g_l - g_t)/3$  describes the anisotropy of the  $g$ -factor along the principal axes of the effective mass tensor for each valley,  $E_{vo}$  is the energy difference between the first excited valley-orbit state and

the ground state,  $\rho = 2330 \text{ kg/m}^3$  is the density of Si, and  $\nu_t = 5860 \text{ m/s}$  and  $\nu_l = 8480 \text{ m/s}$  are the transverse and longitudinal sound velocities, respectively.  $f_{\text{Si}}(\theta, \phi)$  is an angular factor that goes to zero for  $\theta = 0$  ( $B \parallel [001]$ ), and is maximum for  $B \parallel [111]$ .

Eq. 14 was derived in the high- $T$  limit, appropriate for typical X-band ( $\sim 10 \text{ GHz}$ ) ESR experiments at  $T > 1 \text{ K}$  (Feher and Gere, 1959). The full expression contains the term  $(1 + n_{ph}) \approx k_B T / g\mu_B B$ , where  $n_{ph} = (\exp(g\mu_B B / k_B T) - 1)^{-1}$  is the Bose occupation factor of the phonon mode at the Zeeman energy. For this reason,  $T_1^{-1} \propto T$  in the high- $T$  limit. Conversely, single-spin experiments in nanostructures (Morello *et al.*, 2010) are conducted in the low- $T$  limit, where  $(1 + n_{ph}) \approx 1$ . This indicates that only spontaneous emission of phonons can take place. Eq. (15) becomes:

$$T_1^{-1}(B)|_{\text{low-}T} = K_4 \frac{g\mu_B B}{k_B T} B^4 T = K_5 B^5. \quad (16)$$

The  $T_1^{-1} \propto B^5$  dependence arises from the following factors: (i) The density of phonon states  $N(E_Z)$  is proportional to  $B^2$ ; (ii) In the matrix element  $\langle \uparrow | \mathcal{H}_{e-ph;SO} | \downarrow \rangle$ , a factor proportional to  $B$  accounts for the need to break time-reversal symmetry, while another factor proportional to  $\sqrt{B}$  arises from the  $\sqrt{q}$  dependence of the strain caused by a deformation potential phonon, where  $q \propto g\mu_B B$  is the wave number. Therefore,  $|\langle \uparrow | \mathcal{H}_{e-ph;SO} | \downarrow \rangle|^2$  is proportional to  $B^3$ .

(ii) “One-valley” mechanism: A phonon-induced strain introduces a coupling between the  $\Gamma$  band and the nearest  $\Delta$  band (see section III.B.2). This yields an anisotropic modulation of the  $g$ -factor even for an electron confined to a single valley. This one-valley mechanism also yields  $T_1^{-1} \propto B^5$  in the low- $T$  limit, but has a different angular dependence, with fastest relaxation for  $B \parallel [001]$  and slowest along  $[111]$ . Unlike the valley repopulation, the one-valley mechanism always produces a nonzero relaxation rate.

A detailed discussion and experimental study of these relaxation channels for Si:P was given by Wilson and Feher (1961), in the high- $T$  limit [Fig. 57(a)]. Since both the valley repopulation and the one-valley mechanism are generally active at the same time and have a comparable strength, Wilson and Feher (1961) included the analysis of the angular dependence of  $T_1^{-1}$  to unravel the different contributions. The low- $T$  limit has been investigated in the single-shot spin readout experiments of Morello *et al.* (2010), where the  $T_1^{-1} \propto B^5$  law was verified, and the experimental values of  $T_1^{-1}$  were found to be in quantitative agreement with the prediction of Eq. 16 to within factors  $\sim 2$  [Fig. 57(b)]. The longest observed relaxation time for a single spin was  $T_1 \approx 6 \text{ s}$  at  $B = 1.5 \text{ T}$ . Because of the very strong field dependence of  $T_1$ , Feher and Gere (1959) were able to observe  $T_1 \approx 5000 \text{ s}$  at  $T = 1.25 \text{ K}$  and  $B = 0.32 \text{ T}$  in a bulk sample.

	Donors	Quantum dots
Valley Repopulation	$T_1^{-1} \propto B^5$ max $\parallel [111]$ 0 $\parallel [001]$	negligible
One-valley	$T_1^{-1} \propto B^5$ max $\parallel [001]$ min $\parallel [111]$	$T_1^{-1} \propto B^5$ max $\parallel [100], [010]$ 0 $\parallel [001]$
Rashba spin-orbit coupling	negligible	$T_1^{-1} \propto B^7$ max $\parallel [100], [010]$ min $\parallel [001]$

TABLE I Summary of the magnetic field dependence of the spin relaxation rates  $T_1^{-1}(B)$ , for different mechanisms applicable to donors and quantum dots in Si. It is assumed that the dots are formed from  $[001]$  quantum wells.

## 2. Electron spin relaxation in quantum dots

The spin relaxation mechanisms for an electron confined to a quantum dot obtained differ slightly from those in a donor, due to the different valley and orbital nature of the electron states (see section III.B and Fig. 7). The ground and first excited electron wave functions are symmetric or antisymmetric combination of the  $\pm z$  valleys, because of the strong vertical confinement in the quantum well from which the dot is formed. It can be shown that, under this circumstance, the “valley repopulation” mechanism does not contribute to spin relaxation (Glavin and Kim, 2003; Tahan, 2007).

The “one-valley” mechanism, on the contrary, is active and yields a relaxation rate  $T_1^{-1} \propto B^5$  (Glavin and Kim, 2003). Notice that, unlike in the donor case, the one-valley mechanism in dots obtained from a  $[001]$  quantum well gives vanishing relaxation for  $B \parallel [001]$  and  $[110]$  (Tahan, 2007).

An additional mechanism for spin relaxation in quantum dots arises from the structural inversion asymmetry of the quantum well in which the dot is confined, known as Rashba spin-orbit coupling (SOC) (Hanson *et al.*, 2007; Khaetskii and Nazarov, 2000; Rashba, 1960; Tahan and Joynt, 2005). Spin relaxation due to Rashba SOC can become dominant in Si quantum dots if the dot geometry gives rise to low-lying excited states of different orbital symmetry as compared to the ground state, or when the “one-valley” mechanism vanishes due to  $B \parallel [001]$  or  $[110]$ . The magnetic field dependence of the Rashba-SOC spin relaxation channel is  $T_1^{-1} \propto B^7$  for deformation potential phonons (Hanson *et al.*, 2007; Raith *et al.*, 2011; Tahan, 2007), the only ones present in Si. The additional factor  $B^2$  as compared to the valley-related mechanisms, arises from the linear dependence on  $q$  of the matrix element for deformation potential phonons to couple states of different orbital nature. Two experiments (Hayes *et al.*, 2009; Xiao *et al.*, 2010a) have indeed found a behavior consistent with  $T_1^{-1} \propto B^7$  in

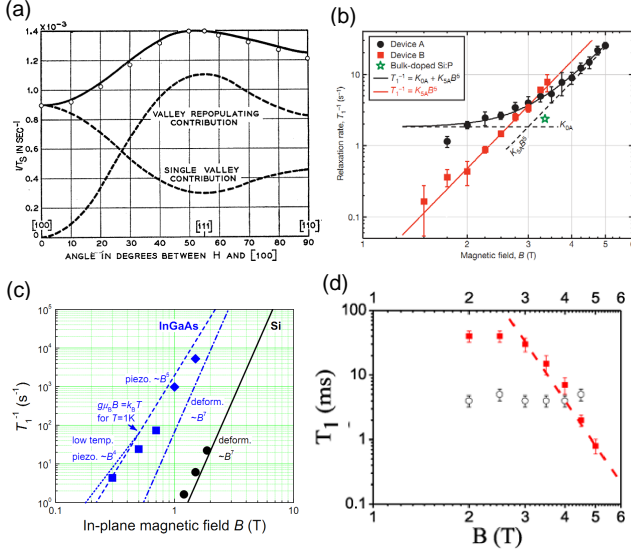


FIG. 57 (a) Spin-lattice relaxation rate  $T_1^{-1}$  of P donors in bulk Si, at  $B \approx 0.3$  T and  $T = 1.2$  K, as a function of the field orientation. The angular dependence allows the separation of “valley repopulating” and “single valley” contributions (Wilson and Feher, 1961). (b)  $T_1^{-1}(B)$  for single P donors in two different devices. Both show a  $T_1^{-1} \propto B^5$  contribution, but Device A also exhibits a  $B$ -independent plateau, attributed to dipolar flip-flops with nearby donors. Also shown is  $T_1^{-1}(3.3T)$  in bulk Si:P (Morello *et al.*, 2010). (c)  $T_1^{-1}(B)$  in a gate-defined Si/SiGe dot (black dots), compared to data for an InGaAs dot (blue squares and diamonds) (Hayes *et al.*, 2009).  $T_1(B)$  in a gate-defined Si MOS dot, for the 1-electron (filled squares) and 2-electron (open circles) states (Xiao *et al.*, 2010a).

gate-defined Si dots [Fig.57(c,d)]. Relaxation times as long as  $T_1 \approx 2.8$  s at  $B = 1.85$  T have been measured in a Si/SiGe dot (Simmons *et al.*, 2011). The relaxation rate depends on the size and shape of the dot, and is inversely proportional to the square of the orbital level spacing, producing longer  $T_1$  for smaller dots. Importantly, the Rashba SOC relaxation channel gives nonzero contribution for any magnetic field direction. A summary of the magnetic field dependencies of the spin relaxation mechanism for donors and dots in Si is given in Table I.

### 3. Singlet-triplet relaxation

The Zeeman-split states of a single electron bound to a donor or a dot constitute a natural qubit. An alternative scheme has been proposed, where the logical qubit is obtained from the two-electron singlet and triplet (S/T) spin states of a double quantum dot (Levy, 2002). Coherent manipulation of S/T qubits has been pioneered in GaAs double dots (Petta *et al.*, 2005), and has recently been demonstrated in Si/SiGe double dots as well (Maune *et al.*, 2012). A ‘digital’ scheme applicable to

donors in Si has also been proposed (Skinner *et al.*, 2003). The first measurement of S/T relaxation in a Si double quantum dot (Prance *et al.*, 2012), discussed in Section VI.C.4, gave a value of  $T_{1,S/T} \sim 10$  ms at  $B = 0$ , two orders of magnitude longer than in GaAs dots (Johnson *et al.*, 2005b). In an applied magnetic field, the spin lifetime of the  $T_-$  state grows up to values of order 3 s at  $B = 1$  T. The theory of S/T spin relaxation in the (1,1) charge configuration of double dots in Si/SiGe was discussed in (Raith *et al.*, 2011; Wang and Wu, 2011), while two groups (Prada *et al.*, 2008; Wang *et al.*, 2010) have analyzed the relaxation mechanisms in a two-electron single dot, which is relevant for the understanding of lifetime-enhanced transport (Shaji *et al.*, 2008) or the direct measurement of spin relaxation in a 2-electron dot (Xiao *et al.*, 2010a).

A theory for exchange-coupled donor pairs exists (Borhani and Hu, 2010), and predicts a complicated dependence of the triplet  $\rightarrow$  singlet relaxation rate on the exchange interaction  $J$ , ranging from  $\propto J$  to  $\propto J^3$ . Valley interference plays a crucial role, since  $J$  can vary over orders of magnitude by simply changing the direction of the axis joining two donors.

### 4. Spin decoherence

The attractiveness of silicon for quantum computing applications arises in large part because of the predicted weakness of the decoherence mechanisms (De Sousa and Das Sarma, 2003; Tahan *et al.*, 2002; Tahan and Joynt, 2005). The main source of decoherence for electron spins in solid state is the coupling to the bath of nuclear spins in the host material. In the spin resonance literature this goes under the name of “spectral diffusion”, to indicate that the time evolution of the state of a bath of nuclear spins coupled to an electron spin causes the electron spin resonance frequency (the “spectrum”) to “diffuse” over a certain range (Klauder and Anderson, 1962). Natural silicon has only a 4.7% concentration of spin-carrying ( $I = 1/2$ )  $^{29}\text{Si}$  isotope, greatly reducing the effects of nuclear fields compared to GaAs devices (Witzel and Das Sarma, 2006). The isotopic purification to silicon consisting of only spinless  $^{28}\text{Si}$  has been demonstrated for some time (Ager *et al.*, 2005), and further pursued to extreme levels in the context of the Avogadro project (Andreas *et al.*, 2011), where a  $^{28}\text{Si}$  sphere with less than  $5 \times 10^{-5}$   $^{29}\text{Si}$  concentration has been produced with the goal of redefining the kilogram. Purified material originating from the Avogadro project has been used to demonstrate exceptional electron spin coherence times  $T_2 > 10$  s (Tyryshkin *et al.*, 2011). Natural germanium contains 7.7%  $^{73}\text{Ge}$  ( $I = 9/2$ ), all other isotopes being spinless. An isotopically purified Si/SiGe heterostructure has been demonstrated (Sailer *et al.*, 2009). Even with unenriched Ge, the effects of the Ge nuclear spins



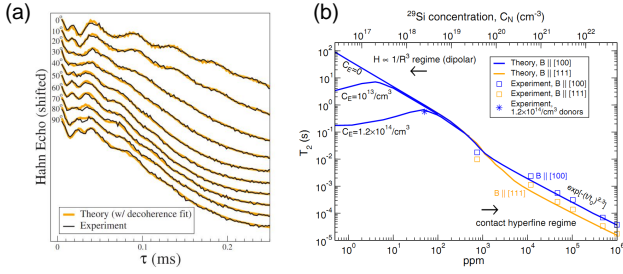


FIG. 58 (a) Experimental echo decay (black) and cluster expansion theory (orange) for  $^{\text{nat}}\text{Si:P}$  at different angles of the magnetic field with respect to the crystallographic [001] axis. Notice the echo envelope modulation arising from anisotropic hyperfine coupling between donor electron and  $^{29}\text{Si}$  nuclei. From (Witzel *et al.*, 2007). (b) Decoherence time  $T_2$  for Si:P as a function of  $^{29}\text{Si}$  concentration,  $C_N$ , for different dopant concentrations,  $C_E$ . The symbols are experimental data points. From (Witzel *et al.*, 2010).

are greatly suppressed because in the typical heterostructures used for Si/SiGe qubits, only about 0.6% of the electron density resides in the SiGe barrier (Shi *et al.*, 2012).

The theory of electron spin decoherence arising from nuclear spins in Si is well understood. The correct order of magnitude of the decoherence time  $T_2$  was already predicted by early studies, where the dynamics of the nuclear spin bath was approximated as Markovian, i.e. neglecting time correlations (De Sousa and Das Sarma, 2003). Full agreement with experimental data in bulk Si:P (Tyryshkin *et al.*, 2003) requires a more sophisticated treatment of the spin bath dynamics, where non-Markovian time correlations are taken into account. Quantum-mechanical solutions of the dynamics of electron spins in a nuclear bath included nuclear spin pair correlations (Yao *et al.*, 2006), all the way to higher-order cluster-expansion techniques (Witzel and Das Sarma, 2006; Witzel *et al.*, 2005). The echo decay takes the form:

$$V(2\tau) \propto \exp(-2\tau/T_R \times \exp[-(2\tau/T_{SD})^\alpha]) \quad (17)$$

where  $\tau$  is the time interval before and after the refocusing  $\pi$ -pulse in the Hahn-echo sequence (Slichter, 1990),  $T_R$  is a relaxation time that accounts for both instantaneous diffusion and  $T_1$  processes,  $T_{SD}$  is the spectral diffusion time, which depends on the internal dynamics of the nuclear bath, and the exponent  $\alpha$  takes the value 2.3 (Witzel *et al.*, 2007). Full matching between cluster expansion theory and experimental data (Tyryshkin *et al.*, 2003) [Fig. 58(a)] was obtained by including the Electron Spin Echo Envelope Modulation (ESEEM) effect (Rowan *et al.*, 1965), which arises from the anisotropic component of the hyperfine coupling to the  $^{29}\text{Si}$  nuclei (Ivey and Mieher, 1975b; Park *et al.*, 2009; Saikin and Fedichkin, 2003).

The cluster expansion technique has been extended to the study of decoherence upon isotopic purification (Witzel *et al.*, 2010) [Fig. 58(b)]. An interesting phenomenon that must be taken into account to match Si:P bulk data is the interplay between  $^{29}\text{Si}$  spectral diffusion and dipole-dipole coupling among electron spins. The latter gives an additional contribution to decoherence, which is always present because any realistic Si crystal contains some level of background doping. The dipolar coupling between donor electron spins contains terms of the form  $S_1^+ S_2^- + S_1^- S_2^+$ , which allow the excitation of spin 1 and de-excitation of spin 2 (“flip-flop” process) or vice-versa, while conserving total energy to within the strength of the coupling term. This process produces additional magnetic noise on a spin qubit. However the presence of some  $^{29}\text{Si}$  nuclei may actually be beneficial in this context. When the inhomogeneity of the local hyperfine fields is stronger than the electron dipole-dipole coupling, flip-flop processes are suppressed by energy conservation. The concept can be extended to any source of local field inhomogeneity, and the field inhomogeneity does not degrade the potential implementation of exchange gates (De Sousa *et al.*, 2001; Hu *et al.*, 2001). On this basis, Tyryshkin *et al.* (2011) have measured  $T_2 > 10$  s by using a highly purified  $^{28}\text{Si:P}$  crystal, and deliberately introducing a magnetic field gradient across the sample to prevent neighboring spins from undergoing energy-conserving flip-flop processes. Another way to suppress flip-flop is lowering the temperature such that  $g\mu_B B \gg k_B T$ , thereby polarizing the electron spins. This would lead to an exponential suppression of the dipolar decoherence channel (Morello *et al.*, 2006; Witzel *et al.*, 2010) because of the scarcity of spins in an excited state.

Once the nuclear spin and dipole-dipole decoherence mechanisms have been thoroughly suppressed, one may expect the remaining dominant decoherence channel to be charge noise, particularly in the case where exchange coupling is used to implement quantum logic gates (Culcer *et al.*, 2009b; Gamble *et al.*, 2012). Dephasing from charge noise is expected to be more pronounced in quantum dot qubits than in donor qubits, but less pronounced than in superconducting qubits, because the characteristic size of quantum dot qubits is intermediate between the sizes of impurity qubits and superconducting qubits.

## B. Orbital and valley relaxation

So far we have discussed the relaxation processes for the electron spin confined to a donor or a gate-defined dot, with the intention of describing the lifetime of an excited qubit state encoded in the spin Hilbert space. Excited orbital or valley states then act as intermediate states for perturbations involving lattice phonons and spin-orbit coupling to cause spin relaxation.

However, the orbital and valley excited states can also

be used actively, for instance to mediate strong interaction between nearby donors. An early proposal suggested the use of the excited  $2p$  orbital states of a deep donor to induce a superexchange interaction between pairs of shallow donors placed on either sides of the central one (Stoneham *et al.*, 2003). This involves the coherent manipulation of hydrogenic Rydberg states, a well established practice in atomic physics. The  $2p$  Rydberg state lifetime for P donors in Si was found to be  $T_1 \approx 200$  ps, attributed to the spontaneous emission of phonons (Vinh *et al.*, 2008). Coherent control of the Rydberg states has also been achieved, with an orbital coherence time  $T_2 \approx 28$  ps (Greenland *et al.*, 2010).

Valley states are expected to have much longer lifetimes and coherence, due to the unlikelihood of processes that cause inter-valley transitions. A recent proposal describes the use of singlet and triplet valley states of a double quantum dot to encode and manipulate quantum information with reduced sensitivity to noise (Culcer *et al.*, 2012). Recent experiments have shed light on the valley physics and its effect on electronic states. Through transport spectroscopy measurements of donor states in FinFETs, Lansbergen *et al.* (2011) showed that under certain conditions relaxation of excited states into lower manifolds is suppressed due to a combination of both spin and valley blockade. This enhanced lifetime results in an additional transport path through the excited state, and appears as a current step in the stability diagram. The phenomena dubbed as ‘lifetime enhanced transport’ (LET) was first observed in a silicon double quantum dot (Shaji *et al.*, 2008) due to a blocked relaxation of a spin triplet into a ground state spin singlet, arising from the long spin relaxation times in silicon (see section IV.F.2). In the experiment, LET enabled Lansbergen *et al.* (2011) to identify a blocked transition between states that have different valley symmetries. They confirm this observation (i) by extracting the tunnel rates in and out of the donor states through a temperature dependent measurement and analysis, and (ii) by computing the low-energy two-electron spectrum of the system from a multimillion atom tight-binding method to compare and identify the measured excited manifolds.

### C. Control and readout of spins in silicon

#### 1. Bulk spin resonance

The dynamics of spins in bulk materials has been traditionally studied by electron spin resonance (ESR) and nuclear magnetic resonance (NMR) techniques. The pioneering experiments on ESR of donors in Si were performed by Feher and Gere (1959). Exceptionally long electron spin-lattice relaxation times were observed at low temperature, with a longest measured  $T_{1e} \approx 1.4$  hours at 1.25 K and 0.3 T. These experiments were

crucial in the development of the general theory of spin relaxation in semiconductors, as well as for the understanding of the electronic structure of donors (Feher, 1959).

Bulk spin resonance has also been used to study electron gases in modulation-doped Si/SiGe quantum wells (Jantsch *et al.*, 1998; Tyryshkin *et al.*, 2005), or the paramagnetic defects that occur at Si/SiO<sub>2</sub> interfaces (Brower, 1989; Poindexter and Caplan, 1983) and in amorphous silicon (Askew *et al.*, 1984; Stutzmann and Biegelsen, 1983). The temperature dependence of  $T_1$  in paramagnetic dangling bonds points to a relaxation mechanism where the electron spin is coupled to the charge fluctuations of the defect, which acts as a tunneling 2-level system (Askew *et al.*, 1984; De Sousa, 2007). Therefore, ESR can be used as a non-invasive diagnostic tool to extract information such as the distribution of tunneling energies of defects in or near amorphous interfaces.

The possibility of enhancing the electron spin coherence of donors in Si by reducing the concentration of the spin-1/2  $^{29}\text{Si}$  isotope (Abe *et al.*, 2010) was demonstrated as early as 1958 (Gordon and Bowers, 1958). In more recent times, the quality of isotopic purification has been further improved (Ager *et al.*, 2005) and reached a pinnacle with the Avogadro project (Becker *et al.*, 2010), to redefine the kilogram as a sphere of pure  $^{28}\text{Si}$ . Tyryshkin *et al.* (2003) showed that a  $^{28}\text{Si}:\text{P}$  sample with P doping concentration  $n \approx 10^{15} \text{ cm}^{-3}$  exhibits a coherence time  $T_{2e} = 60$  ms, by using a conventional Hahn-echo technique (Slichter, 1990), but accounting for the effect of instantaneous diffusion. In bulk experiments, the dipole-dipole coupling between the spins introduces an artefact whereby the refocusing pulse has the effect of flipping the coupled spins, therefore instantaneously changing the local magnetic field and artificially suppressing the echo. The ‘‘true’’  $T_2$  must be obtained by extrapolating the echo decay time constant in the limit  $\theta_2 \rightarrow 0$ . This extrapolation method, however, does not eliminate the dynamical effect of dipole-dipole coupling (Witzel *et al.*, 2010) during the wait time  $\tau$ . The decoherence due to dipolar interaction can be suppressed by introducing a magnetic field gradient across the sample, of magnitude larger than the spin-spin coupling strength. With this method, and using a bulk sample with extreme isotopic purity ( $< 50$  ppm  $^{29}\text{Si}$ ) and low doping ( $n \sim 10^{14} \text{ cm}^{-3}$ ), Tyryshkin *et al.* (2011) obtained a record value of  $T_{2e} \approx 10$  s. The combination of narrow ESR absorption lines, very long spin coherence and the presence of a nuclear spin with  $I = 1/2$ , make the  $^{28}\text{Si}:\text{P}$  system an ideal candidate to explore sophisticated techniques to encode, retrieve and manipulate non-trivial quantum states. Morton *et al.* (2008) demonstrated the ability to store and retrieve an arbitrary quantum state of the P electron onto the  $^{31}\text{P}$  nucleus, obtaining a quantum memory with coherence time  $T_{2n} > 1$  s.

## 2. Electrically-detected magnetic resonance

In a bulk spin resonance experiment, the precession of a spin ensemble is detected through the electromotive force induced in a cavity or pick-up coil. In this way, one can only detect a macroscopic number of spins, typically  $> 10^{15}$ . In semiconductors, however, it is possible to make localized spins and mobile electrons coexist. This allows the detection of spin resonance by electrical means, and yields a significant improvement in detection sensitivity. Electrically-detected magnetic resonance (EDMR) exploits spin-dependent scattering between free carriers and localized spins. A change in the current (or the conductance) of a suitably designed nanostructure is observed when a resonant oscillating magnetic field alters the equilibrium magnetization of localized spins onto which the free carriers are made to scatter (De Sousa *et al.*, 2009). The free carriers can be generated either by illumination (Boehme and Lips, 2003) or by electrostatically inducing an electron layer in a MOSFET structure (van Beveren *et al.*, 2008; Ghosh and Silsbee, 1992; Lo *et al.*, 2007). EDMR has been successfully applied to the detection of spin resonance and coherent control of  $^{31}\text{P}$  dopant spins in Si (Huebl *et al.*, 2008; Lu *et al.*, 2011; Stegner *et al.*, 2006) (Fig. 59), and to demonstrate a very long-lived classical spin memory (McCamey *et al.*, 2010). The detection sensitivity has been pushed to the level of 100 donors in ion-implanted nanostructures (McCamey *et al.*, 2006), and it has been proposed that reaching the single-spin limit is possible, and would yield a quantum nondemolition measurement of the donor nuclear spin (Sarovar *et al.*, 2008).

## 3. Single-shot readout of a single electron spin

To reach single-spin sensitivity, it is necessary to integrate single-charge detection with a spin-dependent displacement of the charge. This idea was already incorporated in the Kane proposal for a Si:P quantum computer (Kane, 1998), where the readout of the electron spin state would take place by detecting the transfer of an electron from the  $D^0$  state of a donor to the  $D^-$  state on its neighbor. This transfer is only allowed if the two electrons form a spin singlet state. The detection of the spin-dependent charge transfer would occur via a single-electron transistor (SET) on the surface of the device. Subsequent proposals pointed out that it is possible to detect the displacement of a single charge through the change in conductance of a small transistor (Vrijen *et al.*, 2000). In addition to the spin-dependent addition of a second electron to an already occupied donor, Martin *et al.* (2003) pointed out that, in the presence of a large magnetic field, a charge center (not necessarily a donor) can change its occupancy state when the excited spin state lies above the Fermi level of a nearby elec-

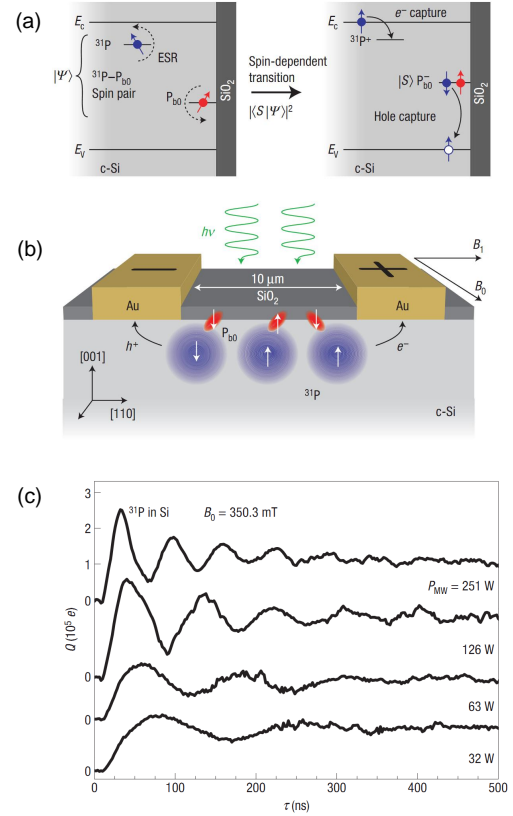


FIG. 59 (a) Sketch of the spin-dependent transition between a donor-bound electron and an interface trap, following the creation of free carriers through illumination. (b) Schematics of an EDMR device. P donors close to charge traps at the Si/SiO<sub>2</sub> interface contribute a spin-dependent scattering mechanism for the electrons traveling between the Au contacts. A resonant microwave excitation alters the polarization of the donor-bound electrons, causing a measurable change of the overall device resistance (c) Electrically detected Rabi oscillations of P-donor electrons, at different values of the driving power. From Stegner *et al.* (2006).

tron reservoir (e.g. the channel of a transistor), while the ground spin state lies below. This process corresponds to an energy-dependent spin-to-charge conversion. If a resonant magnetic field is applied to drive transitions between the spin states, one expects to observe a switching behavior in the current through the transistor, as the system goes through the cycle: excite spin-up state  $\rightarrow$  ionize  $\rightarrow$  load spin-down electron. This method was employed by Xiao *et al.* (2004) to detect the spin resonance of a single charge trap coupled to a small Si transistor (Fig. 60). The same type of spin-to-charge conversion lies at the heart of the single-shot readout of a single electron confined to a GaAs quantum dot (Elzerman *et al.*, 2004). In that case, the spin state of the single electron was detected in a single-shot manner, i.e., with no need for repetition averaging, thanks to the large electrical signal obtained by monitoring the change in conductance of a

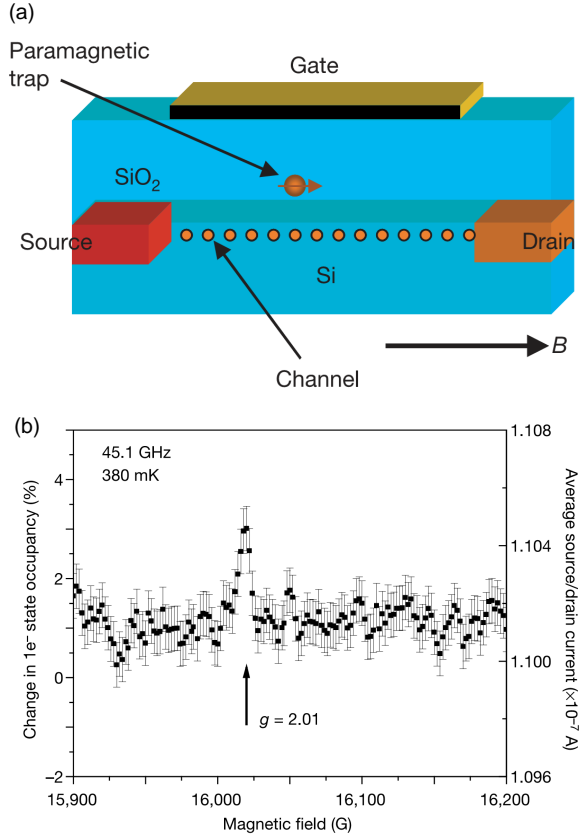


FIG. 60 (a) Schematics of the single charge trap coupled to the channel of a Si transistor. (b) Single-electron spin resonance measurement, obtained by monitoring the average current through the transistor as a function of magnetic field, while applying a microwave excitation at 45 GHz. The excess current at the resonance frequency arises from the change in charge occupancy of the trap, made possible by the driven flipping of its electron spin. From Xiao *et al.* (2004).

quantum point contact with strong electrostatic coupling to the quantum dot.

The spin-to-charge conversion, and therefore the single-shot spin readout, is considerably more challenging in Si than e.g. in GaAs quantum dots. This is because the large effective mass requires tighter electron confinement, and decreases the transparency of tunnel barriers. Averaged spin readout experiments were performed in Si/SiGe (Hayes *et al.*, 2009) and Si MOS (Xiao *et al.*, 2010a) quantum dots, yielding the spin relaxation time  $T_1$ . The first successful single-shot electron spin readout in Si was obtained by Morello *et al.* (Morello *et al.*, 2010), where the electron was bound to a <sup>31</sup>P donor and tunnel-coupled to the island of an induced Si-SET. The readout scheme is a modification of the energy-dependent spin-to-charge conversion used by Elzerman *et al.* (2004). The donor and the SET island effectively form a hybrid double quantum dot (Huebl *et al.*, 2010) connected “in parallel” (Hofmann *et al.*, 1995), where one dot is cou-

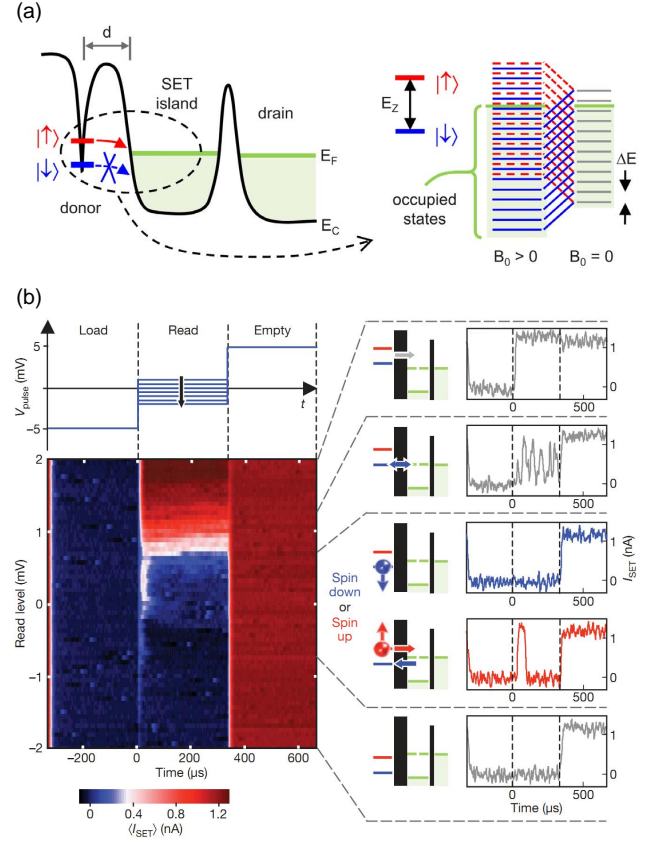


FIG. 61 (a) Spin-to-charge conversion scheme for a single donor tunnel-coupled to the island of a SET. The presence of quantized states inside the SET island can be ignored if the single-particle energy level spacing is smaller than the thermal broadening. From Morello *et al.* (2009). (b) Single-shot readout of a donor electron spin. The individual traces show the evolution of the readout signal as a function of the donor electrochemical potential with respect to the Fermi level. From Morello *et al.* (2010).

pled to source and drain leads, and the other (the donor in this case) is only coupled to the main dot (Morello *et al.*, 2009). This results in a very compact structure and charge transfer signals large enough to completely switch the SET from Coulomb blockade ( $I_{SET} = 0$ ) to the top of a Coulomb peak ( $I_{SET} \sim 2$  nA), resulting in single-shot readout of the donor spin with  $> 90\%$  visibility (Fig. 60). Single-shot spin readout has also been achieved in a gate-defined Si quantum dot (Simmons *et al.*, 2011), using a QPC as charge sensor and the 2DEG in a Si/SiGe heterostructure as the charge reservoir. There, the weaker (purely capacitive) coupling between sensor and dot lead to a current signal  $\sim 20$  pA upon spin-dependent displacement of a single electron charge.

#### 4. Readout and control of singlet-triplet states in double quantum dots

Some of the most successful implementations of spin-based qubits in semiconductors have made use of two-electron systems (Levy, 2002), where quantum information can be encoded into the singlet and triplet (S/T) states of exchange-coupled electrons, instead of the Zeeman split spin states of a single electron. Coherent control (Petta *et al.*, 2005), single-shot readout (Barthel *et al.*, 2009) and dynamical decoupling methods (Bluhm *et al.*, 2010) for S/T qubits have been demonstrated in GaAs double quantum dots. In the quest to implement S/T qubits in Si, the large effective mass plays again a role in requiring very tight electron confinement and reducing the tunnel couplings, which in this case also have the essential role of determining the spin exchange coupling  $J$ . In addition, most S/T qubit implementations in GaAs have made use of a gradient of hyperfine field,  $\Delta B_z$ , between the two dots to be able to control the qubit along two orthogonal axes in the S/T basis (Foletti *et al.*, 2009). Because of the much smaller hyperfine interaction in Si (Assali *et al.*, 2011) as compared to GaAs, the two-axis control of a S/T qubit through  $J$  and  $\Delta B_z$  becomes more challenging. On the other hand, the weak coupling to the nuclear spin bath allows for substantially longer coherence times.

As long as the valley degeneracy of the Si conduction band (Section III.B.2) is completely lifted, the singlet/triplet spin states in Si double quantum dots can be detected and manipulated in the same way as in GaAs dots. The readout mechanism involves Pauli spin blockade (Section IV.F.2). Figure 62 shows the single-shot readout of the singlet and triplet states of a Si/SiGe double quantum dot (Prance *et al.*, 2012). The state of the two-electron system is detected by the detuning  $\epsilon$  from negative – where the (1,1) charge state is stable – to positive – where the electrons can occupy the (0,2) state, provided their spin state is a singlet. Switching between the (1,1) and the (0,2) state produces a signal on the QPC current which can be measured in single-shot. This experiment also yields the triplet spin relaxation time  $T_1$ , which is found to be  $\sim 10$  ms for all triplets at  $B = 0$ , but extends up to  $\sim 3$  s at  $B = 1$  T for the  $T_-$  state, whose splitting from the singlet state is reduced by the applied field.

The coherent control of singlet/triplet states has been achieved in an accumulation-mode Si/SiGe (Section IV.B.3) double quantum dot (Maune *et al.*, 2012). In the S/T qubit basis, one can represent the singlet and triplet states as the poles of a Bloch sphere, with the  $|\uparrow\downarrow\rangle, |\downarrow\uparrow\rangle$  states on the equator (Petta *et al.*, 2005). The exchange interaction  $J$  acts equivalently to an effective field along  $\hat{z}$ , while a gradient of hyperfine field  $\Delta B_z$  between the two dots acts as an effective field along  $\hat{x}$ . Figure 63 shows the measurement of Rabi oscillations in

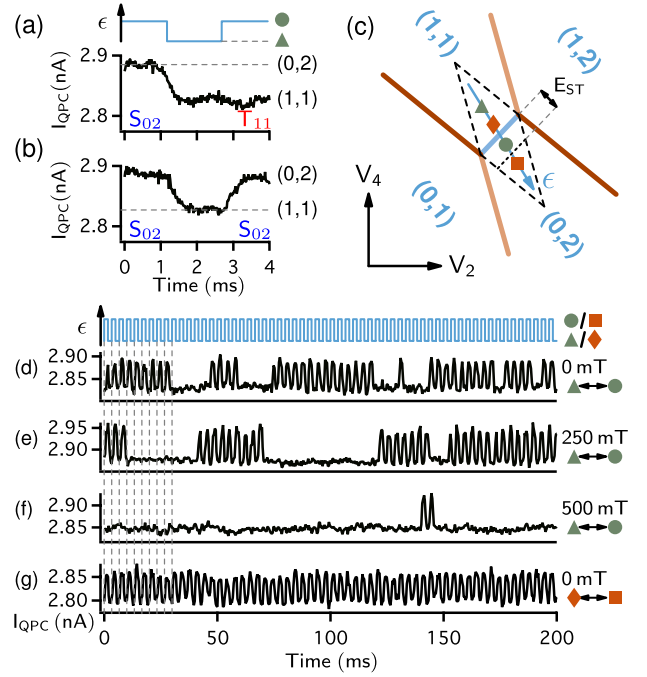


FIG. 62 Single-shot readout of singlet-triplet states in a Si/SiGe double quantum dot. (a,b) QPC current traces,  $I_{QPC}$ , while pulsing the detuning with a square wave. Singlet states are identified when  $I_{QPC}$  returns to a high value, as in (b). (c) Charge stability diagram and pulsing levels. (d – f) Time traces of  $I_{QPC}$  at different magnetic fields, as indicated. Increasing  $B$  extends the lifetime of the  $T_{11}$  (constant current) state. (g) Control sequence, pulsing outside the spin blockade region. From Ref. Prance *et al.* (2012).

the S/T basis of a Si/SiGe DQD. The system is prepared in the (0,2) singlet state by exchange with the leads. A subsequent adiabatic pulse (i.e., slow with respect to the interdot tunnel rate, fast with respect to the S/T mixing time arising from hyperfine interactions) prepares a state close to the equator of the Bloch sphere. The exchange oscillations are then initiated by pulsing closer to the zero detuning line, causing  $J$  to increase and the spin state to undergo a rotation around an axis that depends on the instantaneous value of  $J$  and  $\Delta B_z$ . A final adiabatic pulse brings the state back to  $\epsilon > 0$ , where the electrons occupy the same dot if they returned to a singlet state. The oscillations of the singlet return probability constitute a demonstration of coherent control of the two-electron spin states. The dephasing introduced by the randomness of the hyperfine field can be measured with a modified pulse sequence, where the electrons prepared in the (0,2) singlet state are rapidly separated and left to dephase at  $J \approx 0$  before being brought back to the (0,2) region for readout. The measured dephasing time  $T_2^* \approx 360$  ns (Maune *et al.*, 2012) represents an improvement by nearly two orders of magnitude over the value observed in GaAs dots (Petta *et al.*, 2005), as expected

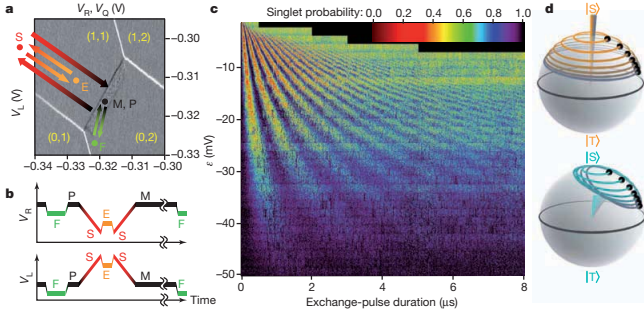


FIG. 63 Coherent manipulation of singlet-triplet states in a Si/SiGe double quantum dot. (a) Charge stability diagram of the double dot system. Colored arrows describe the trajectory in gate space during the pulsing sequence shown in panel (b). The (0,2) singlet state is prepared at point F. Adiabatically moving to point S, where the exchange coupling is very weak, brings the system to the (1,1) singlet. Pulsing to point E turns on the exchange and causes the two-spin state to oscillate between the (1,1) singlet and triplet. M is the measurement point where the electron recombine in the (0,2) state if in singlet state. (c) Rabi oscillations of the singlet probability, as a function of the exchange pulse duration (time spent at point E) and (0,2) - (1,1) detuning. (d) Bloch sphere representation of the trajectories of the two-spin states, for different initial values of the hyperfine fields. From Maune *et al.* (2012).

from the much weaker hyperfine coupling in Si as compared to GaAs (Assali *et al.*, 2011). It should be noted, however, that the smallness of the hyperfine field poses a challenge when attempting to reach the regime where  $J < \Delta B_z$  [Fig. 63(d)].

## ACKNOWLEDGMENTS

We thank Malcom Carroll, Akira Fujiwara, Mark Gyure, Xuedong Hu, Marc Sanquer, Sankar Das Sarma, Andre Saraiva, and Charles Tahan for commenting on the manuscript, Mark Friesen for useful discussions, and Gabri Lansbergen for sharing his thesis work on transport regimes.

FAZ, AM, ASD, MYS, LCLH, GK and SR acknowledge support from the Australian Research Council Centre of Excellence for Quantum Computation and Communication Technology (project number CE110001027) and the US Army Research Office under contract number W911NF-08-1-0527.

GK, SNC and MAE acknowledge support by the U.S. Army Research Office (W911NF-08-1-0482).

GK acknowledges the technical support by Zhengping Jiang in the preparation of the NEMO figures and editorial aspects. GK also acknowledges the long time collaborations with Dr. Timothy B. Boykin and his former student Dr. Neerav Kharche. nanoHUB.org computational resources operated by the network for computational nanotechnology funded by the National Science Foundation have been used in this work.

FAZ acknowledges support from the Foundation for Fundamental Research on Matter (FOM), which is part of the Netherlands Organization for Scientific Research (NWO).

## Appendix A: One-dimensional tight-binding model with valley degeneracy

Appendices A-C present details of different theoretical treatments of the properties of valley splitting relevant to silicon heterostructures. In this appendix we examine an extremely simple one-dimensional tight-binding model (studied in (Boykin *et al.*, 2004a,c)) to illustrate fundamental properties of valley splitting. The model we examine was motivated in terms of the physics of silicon in (Boykin *et al.*, 2004a,c); here, we construct the simplest possible model that exhibits the essential physics.

Tight-binding models are particularly well-suited for exhibiting the physics of valley degeneracy. The simplest possible one-dimensional tight-binding incorporates a single hopping matrix element that describes the amplitude of a particle to hop to a nearest neighbor site. Choosing a position basis in which  $|n\rangle$  denotes the  $n^{\text{th}}$  atom, the wave function  $|\psi\rangle$  is written as

$$|\psi\rangle = \sum_n C_n |n\rangle, \quad (\text{A1})$$

where the sum is over the sites in the lattice. The Hamiltonian  $H$  describing nearest-neighbor hopping is defined by its action on  $|\psi\rangle$ :

$$H|\psi\rangle = \sum_n C_n (t_1 |n+1\rangle + t_1 |n-1\rangle). \quad (\text{A2})$$

We first describe the bulk behavior by imposing a periodic boundary condition. We assume that the chain has  $2N+1$  atoms, with the spatial index  $j$  taking on the values  $-N, -(N-1), -(N-2), \dots, (N-2), (N-1), N$ , with the periodic boundary condition  $\psi(j) = \psi(j+2N+1)$ . For this case, the system has translational symmetry, and the eigenvectors  $|q\rangle = \sum_{j=-N}^N e^{iqaj}$ , with  $a$  the lattice constant, satisfy

$$\begin{aligned} H|q\rangle &= \epsilon|q\rangle \\ \Rightarrow t_1 (e^{iqa} + e^{-iqa}) |q\rangle &= \epsilon_q |q\rangle, \end{aligned} \quad (\text{A3})$$

so the energy eigenvalues  $\epsilon_q$  are

$$\epsilon_q = 2t_1 \cos(qa). \quad (\text{A4})$$

This dispersion relation has its minimum at  $q=0$  when  $t_1 < 0$  and at  $q=\pi/a$  when  $t_1 > 0$ . In either case, there is one value of  $q$  at which the energy is minimized, so there is no valley degeneracy.

To find a model that has nontrivial valley degeneracy, we consider the second-simplest model, in which there are

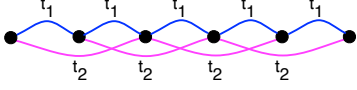


FIG. 64 Sketch of one-dimensional tight-binding model with nearest-neighbor and second-neighbor hoppings that can exhibit nontrivial valley structure.

both nearest-neighbor and second-neighbor couplings, as shown in Fig. 64. Using the same position basis  $|n\rangle$ , the Hamiltonian  $H$  for the model with second-neighbor hopping (shown in Fig. 64) acts on  $|\psi\rangle = \sum_n C_n |n\rangle$  as:

$$H|\psi\rangle = \sum_n C_n (t_1|n+1\rangle + t_1|n-1\rangle + t_2|n+2\rangle + t_2|n-2\rangle) \quad (A5)$$

Again, we first consider the behavior when periodic boundary conditions are imposed ( $\psi(j) = \psi(j+2N+1)$ ), and find that the  $C_n$  satisfy

$$t_2 C_{n-2} + t_1 C_{n-1} + [\epsilon - E]C_n + t_1 C_{n+1} + t_2 C_{n+2} = 0, \quad (A6)$$

with periodic boundary conditions:  $C_{N+j} = C_j$  for all  $j$ . One finds that  $\tilde{C}_q = \frac{1}{N} \sum_{j=1}^N e^{iqj} C_j$  satisfies Eq. A6 when the energy eigenvalue  $E_q$  satisfies

$$E_q = \epsilon + 2t_2 \cos(2q) + 2t_1 \cos(q). \quad (A7)$$

Based on a comparison of this model to actual silicon, it is useful to interpret this model not as a single chain of identical atoms, but rather as a lattice with a two-atom basis (Boykin *et al.*, 2004a). With this interpretation, the unit cell is doubled, and in terms of this larger unit cell there are two bands, with energies  $E_q^{(1)} = 2t_1 \cos(q/2) + 2t_2 \cos(2\pi - q)$  and  $E_q^{(2)} = 2t_1 \cos(\pi - q/2) + 2t_2 \cos(2\pi - q)$  Fig. 65 shows the dispersion relation ( $E_q$  versus  $q$ ) using this interpretation for the parameter values  $t_1 = 0.683eV$  and  $t_2 = 0.612eV$ . These values of  $t_1$  and  $t_2$  are set so that the lower band has a minimum at the observed wave vector,  $q_0 = 0.82(2\pi/a)$ , and that the curvature at the minimum yields the observed longitudinal effective mass of silicon,  $m_{eff} = 0.91m_e$ , where  $m_e$  is the bare electron mass. For this simple one-dimensional model, there are two degenerate valley minima at  $\pm q_0$ , as shown in Fig. 65.

Several physical effects can break the valley degeneracy that is exhibited by the model with periodic boundary conditions, including the effects of electron confinement and electric fields (Ando, 1979; Ando *et al.*, 1982; Ohkawa and Uemura, 1977a,b; Pantelides, 1978; Pantelides and Sah, 1974; Sham and Nakayama, 1979). Here we illustrate how valley splitting emerges for perhaps the simplest model that exhibits valley splitting (Boykin *et al.*, 2004c), in which confinement is introduced by implementing hard-wall boundary conditions instead of periodic boundary conditions. For this case, the  $C_n$  satisfy

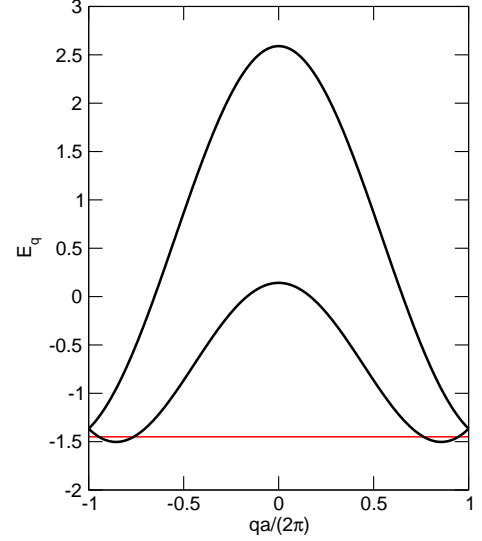


FIG. 65 The dispersion relation (plot of energy  $E_q$  versus wave vector  $q$  of the energy eigenstates), of the one-dimensional tight-binding model defined in Eq. A5, interpreted as a model with two atoms per unit cell, when the parameter governing hopping between nearest neighbors  $t_1 = 0.683eV$  and the parameter governing hopping between second-nearest neighbors  $t_2 = 0.612eV$ . For these values of  $t_1$  and  $t_2$ , the minimum energy for the lower band is at  $q_0 = 0.82(2\pi/a)$ , as is found in bulk silicon, and the curvature at the minimum is consistent with the longitudinal effective mass of electrons in silicon,  $m_{eff} = 0.91m_e$ , where  $m_e$  is the electron mass. The horizontal line in the figure intersects the dispersion relation at four points; the energy eigenvector for a square well with hard wall boundary conditions is a linear superposition of these four eigenstates of the problem with periodic boundary conditions. For a flat square well, the eigenstates have definite parity (a given eigenstate is either symmetric and antisymmetric) with the form given in Eq. A9 or in Eq. A10.

Eq. (A6) when  $|n| \leq N - 2$ , but now with boundary conditions

$$C_{-(N+2)} = C_{-(N+1)} = C_{N+1} = C_{N+2} = 0. \quad (A8)$$

Because the on-site potential energy  $\epsilon$  in Eq. A6 is the same for all sites in the chain, the energy eigenvectors in the energy region where the energy-momentum dispersion relation is fourfold degenerate are sums of four terms, each with the form  $e^{ijq_i a}$ , where the  $q_i$  satisfy the condition that their  $E_{q_i}$  are identical. We denote the four values of  $q$  with the same energy eigenvalue  $E$  as  $q_+$ ,  $q_-$ ,  $-q_+$ , and  $-q_-$ , and write  $\psi_E = A_{-+} e^{iq_- j a} + A_{--} e^{-iq_- j a} + A_{++} e^{iq_+ j a} + A_{+-} e^{-iq_+ j a}$ . The values of  $E$  and of the  $A$ 's are determined by requiring that the boundary conditions, Eq. A8, be satisfied, as described in ((Boykin *et al.*, 2004a,c)). For a system with reflection symmetry, the eigenstates are either symmetric or antisymmetric. The lowest energy symmetric eigenstate

has the form

$$\begin{aligned}\psi_{sym} &= A [\cos(q_+ja) - \cos(q_-ja)] \\ &= -2A \sin\left(\frac{q_+ja + q_-ja}{2}\right) \sin\left(\frac{q_+ja - q_-ja}{2}\right),\end{aligned}\quad (\text{A9})$$

with  $A$  a normalization constant, while the lowest energy antisymmetric eigenstate has the form

$$\begin{aligned}\psi_{antisym} &= A [\sin(q_+ja) + \sin(q_-ja)] \\ &= 2A \sin\left(\frac{q_+ja + q_-ja}{2}\right) \cos\left(\frac{q_+ja - q_-ja}{2}\right).\end{aligned}\quad (\text{A10})$$

Since  $q_+$  and  $q_-$  are both very close to  $q_0$ , the wave vector at the band minimum, the quantity  $q_+ - q_-$  is much smaller than  $q_+ + q_-$ . Therefore, the lowest energy symmetric and antisymmetric wave functions both have a symmetric envelope, and the different behavior under inversion arises because of the differences in the fast oscillations, as shown in Fig. 8 in the main text. The energies of the two lowest eigenstates can be calculated within perturbation theory in powers of  $1/S$ , where  $S$  is the number of atoms in the quantum well (Boykin *et al.*, 2004c); to leading order, the valley splitting  $\Delta_V$ , which is the magnitude of the difference of the energies of the two lowest-energy states, is

$$\Delta_V \simeq \frac{16\pi^2 t_2}{(S+2)^3} \left| \sin[(S+2)\phi_0] \right| \sin(\phi_0), \quad (\text{A11})$$

where  $\phi_0 = q_0 a/2$  and  $\sin(\phi_0) = \sqrt{1 - (t_1/4t_2)^2}$ . The energy difference between the symmetric and antisymmetric states oscillates as a function of well width, and for some widths the antisymmetric state has lower energy than the symmetric state. Thus, the valley splitting is highly sensitive to the details of the boundaries of the quantum well. This sensitivity to details of the interface more than one dimension the valley splitting to disorder at the interfaces. As one considers systems in more than one dimension, and if the interface is not perfectly flat, then it is nontrivial to determine the energy eigenstates and the valley splitting. Methods for understanding the valley splitting in more realistic and complicated geometries are presented in Appendices B and C.

## Appendix B: Effective mass theory for quantum wells

In this appendix we examine effective mass theory (EMT) for electrons in quantum wells and describe the relationships between EMT results and those obtained using tight-binding methods. We first discuss how the coupling between valleys can be incorporated in EMT using a single coupling parameter (following Refs. (Friesen *et al.*, 2007) and (Friesen and Coppersmith, 2010)), and then we discuss how EMT can be applied to address the effects of interface disorder.

In bulk silicon, one writes the wave function  $\psi(\vec{r})$  for an electron bound to a donor as the sum of contributions from each of the six degenerate valleys (Friesen, 2005),

$$\psi(\vec{r}) = \sum_{j=1}^6 \alpha_j \phi_j(\vec{r}) F_j(\vec{r}), \quad (\text{B1})$$

where  $\alpha_i$  are valley composition parameters that specify the contribution to the wave function from each of the six valleys that satisfy the normalization condition  $\sum_{i=1}^6 |\alpha_i|^2 = 1$ . The Bloch functions that describe the variations on short length scales are  $\phi_i(\vec{r}) = u_i(\vec{r}) e^{i\vec{k}_i \cdot \vec{r}}$ , where  $\vec{k}_i = k_0 \hat{i}$  is the wave vector that specifies the minimum of the  $i^{\text{th}}$  conduction valley, and  $u_i$  has the periodicity of the crystal lattice. The  $F_i$  are the envelope functions for the six valleys that specify that variation on long length scales.

In strained quantum wells, the in-plane valleys have substantially larger energies than the z-valleys (Schäffler *et al.*, 1992), so the only valleys that are relevant for the low energy electronic wave functions are those along  $\pm z$ , so the effective mass (EM) wave function  $\Psi(\vec{r})$  for strained silicon can be written

$$\psi(\vec{r}) = \sum_{j=\pm z} \alpha_j e^{ik_j z} u_{\vec{k}_j}(\vec{r}) F_j(\vec{r}). \quad (\text{B2})$$

The constants  $\alpha_j$  both satisfy  $|\alpha_j| = 1/\sqrt{2}$  and thus describe the relative phase between the two  $z$  valleys. Once again, the Bloch functions  $u_{\vec{k}_j}(\vec{r})$  describe the variations that are periodic with the lattice constant period, and  $\vec{k}_0 = \pm k_0 \hat{z}$  are the values of  $k$  at which there are conduction valley minima. The envelope functions  $F_j(\vec{r})$  are the same for the two valleys. The valley splitting physics enters only in very small region near the quantum well boundary, so the  $\alpha_j$  parameters that describe the valley physics may be obtained from first-order, degenerate perturbation theory, with the valley coupling treated as a perturbation (Koiller *et al.*, 2001).

We first consider the case of a quantum well with no disorder that is perfectly aligned with its normal along (001). For this case, the energy eigenstates come in pairs with the same envelope functions but with different valley compositions as described by  $\alpha_{-z}$  and  $\alpha_z$ . The envelope function is determined using the eigenvalue equation

$$\sum_{j=\pm z} \alpha_j e^{ik_j z} [H_0 + V_v(z) - \epsilon] F_j(z) = 0, \quad (\text{B3})$$

where

$$H_0 = T(z) + V_{QW}(z) + V_{conf}(z). \quad (\text{B4})$$

Here,  $\epsilon$  is the energy eigenvalue and

$$T = -\frac{\hbar^2}{2} \frac{\partial}{\partial z} \left( \frac{1}{m_l} \frac{\partial}{\partial z} \right) \quad (\text{B5})$$



is the one-dimensional kinetic energy operator.<sup>2</sup> The three different potential energies in Eq. B3 and Eq. B4 are  $V_v(z)$ , which is the valley coupling that will be treated perturbatively,  $V_{QW}(z)$ , which describes the effects of the conduction band offsets in the heterostructure, and  $V_{conf}$ , which describes any additional, slowly varying potential. A typical confinement potential has the qualitative form  $V_{conf} \propto -eEz$ ; it is an electrostatic potential that rises either from modulation doping in the heterostructure or by application of voltages using external gates. The valley coupling arises because of abrupt changes at the quantum well interfaces, and the effective valley coupling potential  $V_v(z)$  is vanishingly small everywhere except within an atomic-scale region near the interface. Therefore, on the long length scales over which EMT is valid, the valley coupling potential can be treated as a delta function:

$$V_v(z) = v_v \delta(z - z_i), \quad (\text{B6})$$

where the interface is located at  $z = z_i$ , and  $v_v$  is a scalar parameter that can be determined from experiment or from atomistic theory (Chutia *et al.*, 2008; Saraiva *et al.*, 2009). As Fig. 66 shows, the results from effective mass theory agree very well with tight-binding results of the simple two-band model of Refs. (Boykin *et al.*, 2004a,c).

The effective mass theory no longer factorizes to yield a one-dimensional equation when the quantum wells are not perfectly flat and aligned perpendicular to  $z$ . As discussed by Friesen and Coppersmith (2010), the valley coupling potential now can cause mixing between orbital eigenstates, so that it no longer appropriate to have separate orbital and valley quantum numbers except in certain limiting cases. Introducing a tilded index  $\tilde{n}$  as a combined valley-orbital label, and ignoring umklapp terms, and using the fact that valley-orbit mixing is absent in zeroth order, one obtains an EMT equation for the eigenstate labeled by the index  $\tilde{n}$ :

$$\sum_n \sum_{j=\pm 1} \alpha_{\tilde{n},n,j} e^{ij k_0 z} [H_0 + V_j(\vec{r}') - E_{\tilde{n}}] F_n(\vec{r}') = 0. \quad (\text{B7})$$

In Eq. (B7), the index  $j = \pm 1$  is the valley index for the valley centered at  $\vec{k}_j = j k_0 \hat{z}$ . Because the interaction  $V_j$  mixes unperturbed orbitals with different quantum numbers  $n$ , Eq. (B7) includes a sum over the index  $n$ . The eigenstate labeled by  $\tilde{n}$  has energy eigenvalue  $E_{\tilde{n}}$  and eigenvector  $\alpha_{\tilde{n}}$ . This theory enables one to obtain qualitative understanding of the effects of magnetic

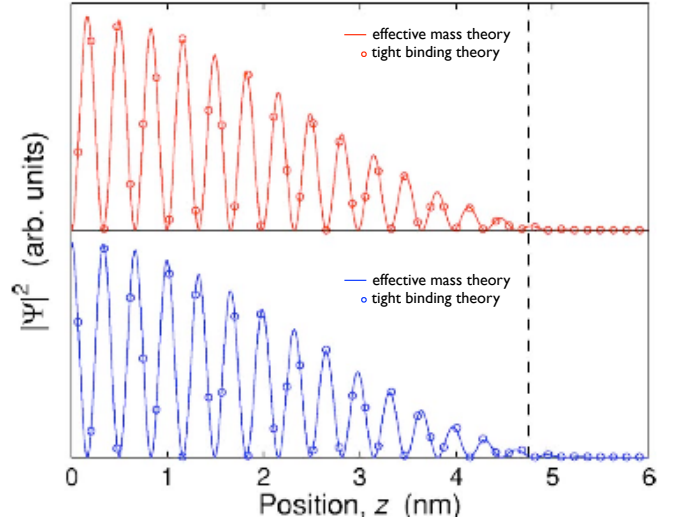


FIG. 66 Plot of two lowest eigenstates in a finite square well obtained using effective mass theory (solid curve) and using tight binding theory (circles), as a function of the quantum well width, from Ref. (Friesen *et al.*, 2007). The plots are of charge density oscillations with a wave vector close to the wave vector of the valley minimum  $k_0$ , and provide a quantitative example of the wave function oscillations sketched in Fig. 8 in the main text. The two lowest eigenstates have the same envelope; the two states are orthogonal because the fast oscillations have different phases relative to the well boundary. Results are shown for parameters appropriate for a  $\text{Si}_{0.7}\text{Ge}_{0.3}/\text{Si}/\text{Si}_{0.7}\text{Ge}_{0.3}$  quantum well of width 9.5 nm. The well width used for the effective mass theory (EMT) is allowed to differ from that used for the tight binding calculation by up to a single atomic layer, or  $a/4 = 1.36\text{\AA}$ . Similar quality agreement is obtained between EMT and tight-binding results for a broad range of quantum well widths and conduction band offsets when the valley mixing parameter is  $v_v = 7.2 \times 10^{-11} \Delta E_c$ , where  $\Delta E_c$  is the conduction band offset of the quantum well.

fields on valley splitting of electrons in rough quantum wells (Friesen *et al.*, 2006) as well as the effects of the confinement potentials from the finger gates that define the quantum dot (Friesen and Coppersmith, 2010). However, because the valley-orbit coupling itself has nontrivial spatial dependence, and the degree of the effects that valley-orbit coupling has on the wave functions depends on the nature of the orbital eigenstates, in real devices the effects of valley-orbit coupling can be highly nontrivial (Friesen and Coppersmith, 2010; Saraiva *et al.*, 2009).

### Appendix C: Atomistic treatment of valley splitting in silicon

#### 1. Atomistic representations for nanometer-scaled devices

Work on the first room temperature electronic quantum device, the resonant tunneling diode, showed (Bowen *et al.*, 1997) that the confinement of electrons to spa-

<sup>2</sup> The effective mass  $m_l$  in the kinetic energy operator is potentially materials-dependent. However, in Si/SiGe heterostructures, the change in longitudinal effective mass  $m_l$  is small, and, moreover, the results are qualitatively insensitive to the introduction of different values of the effective mass on the opposite sides of an interface.

tial regions of less than 5 nm exposes significant band structure effects that cannot be captured *a priori* with an effective mass model. These critical band structure effects are non-parabolicity, band warping to the valence band, and coupling of multiple valleys. The tight binding  $sp^3s^*$  model was found to capture these critical band structure effects without any additional material or structural parameters. Unprecedented predictive modeling capabilities for resonant tunneling diodes were achieved in the NEMO1D modeling tool (Bowen *et al.*, 1997) when an atomistic full band basis was used, while a simple effective mass model proved to be incomplete and would require *ad hoc* additional structural and material tuning (Klimeck *et al.*, 1995).

The experimental conditions of Si quantum wells buffered by  $Si_xGe_{1-x}$  confinement layers are not that different from standard resonant tunneling diodes: electrons are confined in one dimension to around 5 nm. Multi-orbital tight binding models such as  $sp^3s^*$  or  $sp^3d^5s^*$  are full Brillouin zone, atomistic representations of the underlying material. Any breaking of the translational symmetry such as heterostructures, disorder, and strain is fundamentally built into the atom-to-atom interactions of the overall Hamiltonian. No additional material or structural parameters are needed to accommodate the modeling and simulation of complex geometries and structures.

The choice of the tight binding basis set and parametrization is a critical determination of the ultimate heterostructure modeling capabilities. Direct gap III-V semiconductors can be reasonable well described with an  $sp^3s^*$  model (Klimeck *et al.*, 2000a) unless strain behaviors need to be represented (Boykin *et al.*, 2002; Klimeck *et al.*, 2002). The conduction band of Si cannot be well represented by a simple nearest neighbor  $sp^3s^*$  model (Klimeck *et al.*, 2000b) but require either a second nearest neighbor interaction (Klimeck *et al.*, 2000b) or the addition of five d-orbitals (Boykin *et al.*, 2007a, 2004b, 2010).

## 2. Atomistic valley splitting in ideal, freestanding slabs

The most simple approach to the atomistic modeling of strained Si quantum wells in a full band atomistic modeling is to avoid the explicit representation of the random  $Si_xGe_{1-x}$  buffer altogether. Studies involving empirical tight binding using the well-qualified second nearest neighbor (Klimeck *et al.*, 2000b)  $sp^3s^*$  model were first published in 2000 where ideal free-standing Si slabs biaxially strained to a  $Si_{0.75}Ge_{0.25}$  substrate were considered (Boykin *et al.*, 2004a,c). A computational study was performed to examine the dependence of the VS as a function of Si quantum well (QW) width.

The VS was found to be highly dependent on the QW width (Boykin *et al.*, 2004a,c) as depicted in Fig. 67. A

very simple 2 band model was developed to show that the VS can be directly connected to the coherent Quantum mechanical coupling of multiple valleys and does not involve any spin interactions. The simple 1d-chain 2 band model also enabled a derivation of the envelope of the VS oscillations with QW thickness (see Appendix A). The VS is sensitive to the atomistic details of the quantum well with where 2 sequences of VS dependencies, for an even and an odd number of atoms in the QW, can be seen in the simulations. Wave function parity is critical in the understanding of this symmetry.

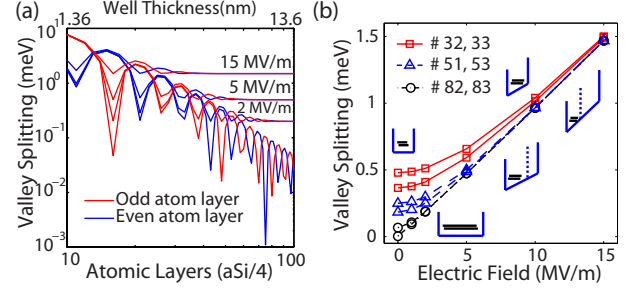


FIG. 67 (a) Valley splitting (VS) as a function of Si quantum well (QW) width. VS is sensitive to the atomic symmetry of the QW with respect to even and odd number of atoms. (b) VS as a function of electric field.

The application of an electric field in the growth direction of the QW showed that the VS oscillations can be damped out when the electron wave functions are confined against a single hetero interface and one homo-interface, rather than two interfaces. Under appreciable applied fields, the VS was found to be independent of the QW thickness when the QW thickness becomes larger than the wave function extension of the lowest 2 confined states. This result makes intuitive sense, since extending the high energy lever arm of an already long quantum well does not change the low energy triangular confinement (see inserts in Fig. 67). VS therefore must be independent of the QW thickness under a finite bias for large enough QWs.

Overall the atomistic simulation of an ideal, freestanding, strained Si slab showed that

1. VS can indeed be tuned by QW thickness and confinement electric fields.
2. VS can be computed in an atomistic approach without further structural or material parameters
3. VS is extremely sensitive to the wave function overlaps and interactions at the QW interface
4. The atomistic symmetry of the interfaces is critical as even and odd number of atoms in the quantum well show orthogonal sets of VS dependences on quantum well thickness.

However, with the availability of subsequent experimental VS splitting results (Goswami *et al.*, 2007) it became clear that the atomistic calculations as presented in Boykin *et al.* (2004a,c) overpredict the VS by two orders of magnitude. It became clear that additional physics had to be added beyond the Si QW. An explicit treatment of the surrounding  $\text{Si}_x\text{Ge}_{1-x}$  buffer material appeared to be needed. The following section illustrates the physical properties of the random alloy  $\text{Si}_x\text{Ge}_{1-x}$  in some detail and show that indeed that an atomistic treatment can deliver fundamental insight.

### 3. Atomistic description of disorder in SiGe alloys

To understand valley splitting in a strained Si QW confined by  $\text{Si}_x\text{Ge}_{1-x}$ , one challenge is how to model disorder of  $\text{Si}_x\text{Ge}_{1-x}$ . The following sub sections present the critical elements to model the  $\text{Si}_x\text{Ge}_{1-x}/\text{Si}$  interface with an atomistic approach to predict the Valley Splitting in relevant device structures quantitatively.

#### a. Atom-type-disorder

The alloy  $\text{Si}_x\text{Ge}_{1-x}$  is not ordered in certain patterns of Si and Ge atoms, but it actually is a random alloy. While the atoms nominally sit on a diamond lattice, the actual atom type on the respective lattice site is a random variable. The  $\text{Si}_x\text{Ge}_{1-x}$  is therefore not a regularly ordered Bravais crystal with a truly defined band structure, that is principally defined only on a periodic cell. Algorithms have been developed (Boykin *et al.*, 2007a) and applied to  $\text{Si}_x\text{Ge}_{1-x}$  nanowires (Kharche *et al.*, 2008) to obtain *approximate* band diagrams through a projection technique.

Figure 68 depicts a random sample of a  $\text{Si}_x\text{Ge}_{1-x}/\text{Si}$  heterostructure where it is evident that the typical assumption of an abrupt interface is evidentially false. There are fluctuations of atom type disorder at the interface resulting in different interface topologies from one sample to the next. It appears to be intuitive evident that an electron wave function that may be confined by the  $\text{Si}_x\text{Ge}_{1-x}/\text{Si}$  interface will probe different configurations and have spatially different penetration depths into the  $\text{Si}_x\text{Ge}_{1-x}$  buffer layer.

#### b. Atom-position-disorder

The natural lattice constants of pure Si and Ge, are quite different at values of  $a_{\text{Si}} = 0.5431\text{nm}$  and  $a_{\text{Ge}} = 0.5658\text{nm}$ , respectively. The lattice constant of the bulk material  $\text{Si}_x\text{Ge}_{1-x}$  follows Vegard's Law, which basically interpolates the  $\text{Si}_x\text{Ge}_{1-x}$  lattice constant linearly with the alloy fraction,  $x$ , and the respective two lattice con-

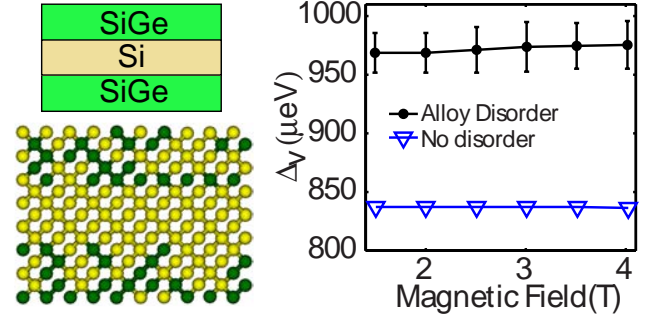


FIG. 68 Sample of an atomic plane of two [100] oriented  $\text{Si}_{0.75}\text{Ge}_{0.25}/\text{Si}$  hetero interfaces. Si atoms are represented as yellow dots and Ge atoms are represented as green dots. Sketched on the top left is a typical representation of a continuum basis  $\text{Si}_x\text{Ge}_{1-x}/\text{Si}$  interface with a typical assumption of an abrupt interface. With the atomistic representation of the random alloy it is quite evident that there are fluctuations at the interface as well as the  $\text{Si}_x\text{Ge}_{1-x}$  itself. The right graph shows the effects of the random  $\text{Si}_x\text{Ge}_{1-x}$  alloy surrounding a strained Si QW compared to a free-standing Si QW without any buffer as a function of external magnetic field. The Si QW has a thickness of 10nm and 5 samples are averaged for different statistical alloyed buffer samples. The random alloy buffer increases the VS compared to an ideal abrupt interface without a  $\text{Si}_x\text{Ge}_{1-x}$  representation.

stants. Such crystal interpolation is sometimes also referred to as Virtual Crystal Approximation (VCA).

$$a_{\text{SiGe}}^{\text{avg}}(x) = xa_{\text{Si}} + (1-x)a_{\text{Ge}} \quad (\text{C1})$$

As depicted in Figure 68  $\text{Si}_x\text{Ge}_{1-x}$  is a random alloy consistent of Si-Si, Si-Ge, and Ge-Ge bonds. In an ideal world all these bonds would have the same length  $\sqrt{3}/4a_{\text{SiGe}}^{\text{avg}}(x)$  as described by Eq. C1. Such ideal single bond length would result in an ideal diamond lattice where only the atom type would fluctuate. This ideal equidistant atom position placement, is however energetically not favorable. The forces between the bonding atoms associated with the three different bonds are different. A Si atom would like to pull a neighboring Si atom closer and push a Ge atom further than the average bond length resulting in atom position shifts off the homogeneous zincblende crystal positions. In fact in a random 3D  $\text{Si}_x\text{Ge}_{1-x}$  alloy one can find through x-ray analysis (Yonenaga *et al.*, 2007, 2005) that there is indeed a tri-modal bond distribution. Indeed any Ge atom will try to push a neighboring Ge atom away towards the unstrained Ge-Ge bond length of 0.245nm. The Ge atom will also allow a neighboring Si atom to come closer than a Ge neighbor. Similarly any Si atom will try to attract a neighboring Si atom to its unstrained bulk distance and will push a Ge atom further away. Figure 69 compares the resulting tri-modal bond distribution as a function of Ge fraction in the alloy as measured by experiment (Yonenaga *et al.*, 2007, 2005), the average bond length and the distribution obtained with the NEMO tool suite

(Klimeck *et al.*, 2007, 2002; Steiger *et al.*, 2011), which uses a valence force field. Clearly an assumption of a homogeneous bond distribution with one average value fails on a local nanometer scale.

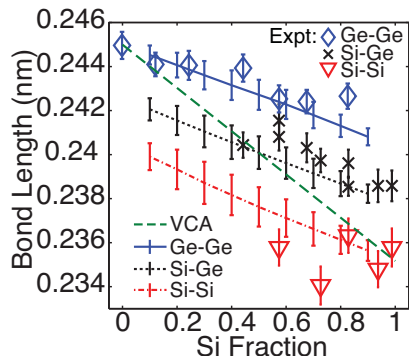


FIG. 69 Statistical bond distribution in a  $\text{Si}_x\text{Ge}_{1-x}$  alloy as a function of Si concentration ( $x$ ). The bond distribution is *not* homogeneous with a single average value, but tri-modal with distinct peaks associated with Ge-Ge, Ge-Si, and Si-Si bonds. Experimental data are taken from Yonenaga *et al.*, 2007, 2005 and numerical values are computed with the NEMO tool suite (Klimeck *et al.*, 2007, 2002; Steiger *et al.*, 2011). The computational experiment is conducted for each Ge fraction on 5 samples containing roughly  $10^6$  atoms.

#### c. Alloy concentration disorder

The two previous disorder types (Atom-type-disorder and atom-position-disorder) assumed that spatially an exact alloy concentration is known. However, the alloy concentration itself cannot be exactly controlled and is an experimentally determined random variable. This random variable will most likely be also spatially dependent pending various reactor conditions.

The slopes of the three bond lengths as a function of alloy contraction in Fig. 69 indicate that an alloy concentration disorder will further broaden the statistical distribution of sampled bond lengths within any given volume. Such additional fluctuations can be assumed to have further influence on the details of the  $\text{Si}_x\text{Ge}_{1-x}/\text{Si}$  interfaces and therefore on the resulting VS.

## 4. Valley splitting in disordered systems

The discussions in the previous sub section indicated that  $\text{Si}_x\text{Ge}_{1-x}$  cannot really be considered a smooth material. The natural question arises what such alloy disorder might "do" to VS. This line of questioning is being explored in the next sub sections.

### a. Flat disordered SiGe buffers

VS computed in atomistically flat QWs without the explicit representation of the  $\text{Si}_x\text{Ge}_{1-x}$  buffer leads to an overprediction of the experimentally observed (Goswami *et al.*, 2007) VS by two orders of magnitude, as discussed above. Figure 68 shows the results of statistical samples of explicit representations of the  $\text{Si}_x\text{Ge}_{1-x}$  Buffer (Kharche *et al.*, 2007) as a function of magnetic field. The numerical experiment suggests that the explicit buffer actually increases the VS slightly and the VS remains roughly independent of the magnetic field, unlike the experimental data. It appeared that some physical mechanism is still missing in the modeling and representation of the problem.

### b. A slanted Si quantum well without explicit SiGe

Closer inspection of the experimental data (Goswami *et al.*, 2007) indicates that the wafer had been grown under a two degree slant. Ando (1979) had shown analytically that such a wafer slant may have a significant effect on VS. Using the atomistic tight binding one can represent a slanted Si slab explicitly (Kharche *et al.*, 2007) without an explicit  $\text{Si}_x\text{Ge}_{1-x}$  representation as depicted in Fig. 70. By symmetry arguments one can find that at zero magnetic field the VS is exactly zero for the lowest conduction bands points due to the tilt in the spatial basis. A small minigap opens up in an energy range irrelevant for carrier occupation. An additional wave function confinement is needed to introduce a valley splitting in relevant energy ranges. Such additional confinement can be obtained by a magnetic field, physical lateral confinement (via electrostatic gates or heterostructures (Srinivasan *et al.*, 2008)). The simulations on an ideal, 2-degree slanted QW, with perfect steps, without any  $\text{Si}_x\text{Ge}_{1-x}$  buffer shows a roughly linear relationship with magnetic field, as observed in the experiment. However the magnitude of the VS is about one order of magnitude too small compared to the experimental data.

### c. A slanted Si quantum well with disordered SiGe buffer

The next natural step of modeling the slanted QW is to include the  $\text{Si}_x\text{Ge}_{1-x}$  buffer explicitly in it. The model data depicted in Fig. 71 assumes that the Si QW steps are straight without disorder, but buffers these regular steps with disordered  $\text{Si}_x\text{Ge}_{1-x}$ . Interestingly this disorder introduces an increased VS and indeed the VS approaches the experimental data. However also in this model the slope of the magnetic field dependence is not captured properly.

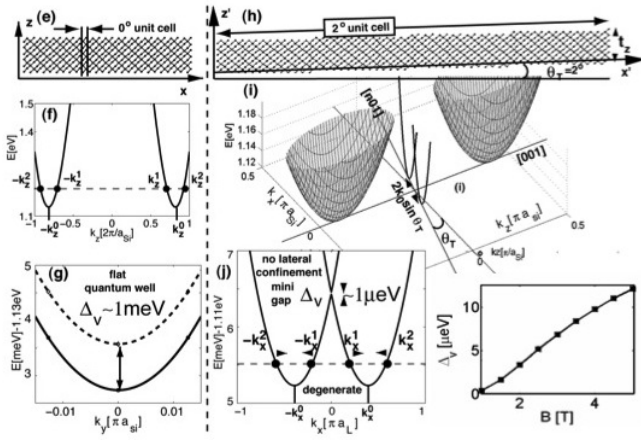


FIG. 70 VS in a free-standing flat and slanted Si QW. VS is induced due to the coupling of equivalent valleys in a flat QW due to the breaking of the symmetry in the growth direction. In a slanted QW the equivalent valleys are shifted and the bands do not split. At zero magnetic field the slanted QW VS splitting is exactly zero. Additional confinement in another direction is needed to create valley splitting. A magnetic field provides lateral confinement and increases the VS roughly linearly. The VS is, however, about one order of magnitude too small compared to the experimental data. (Goswami *et al.*, 2007).

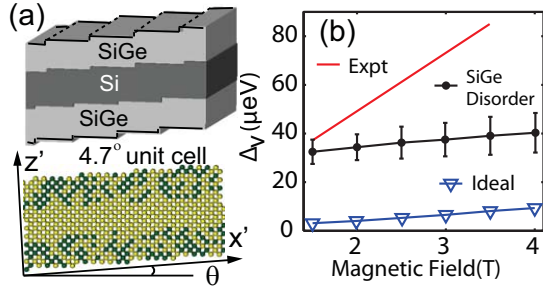


FIG. 71 (a) Sketch of a 4.7 degree slanted QW with a SiGe buffer. The large slant angle is only used for visualization purposes here. The VS simulations use a 2 degree slant. (b) VS in samples of perfectly stepped 2 degree slanted Si QWs with  $\text{Si}_x\text{Ge}_{1-x}$  disorder. The VS is increased over the ideal, non-disordered slanted QW results approaching the experimental data. The slope of the magnetic field dependence is not quite the same, however.

d. A slanted Si quantum well with disordered steps without SiGe buffer

A close look at the experimental (Goswami *et al.*, 2007) structure reveals that the slanted wafer does not have regular steps as assumed in the previous sub section. The steps are actually characterized by alternating smooth and disordered steps. In the following model enhancement the noisy steps are represented explicitly without any  $\text{Si}_x\text{Ge}_{1-x}$  buffer. The sampling of different disordered steps via atomistic representation in tight binding increases the VS significantly, reasonably close to the ex-

perimental data, although the slope of the magnetic field dependence is different as shown in Fig. 72.

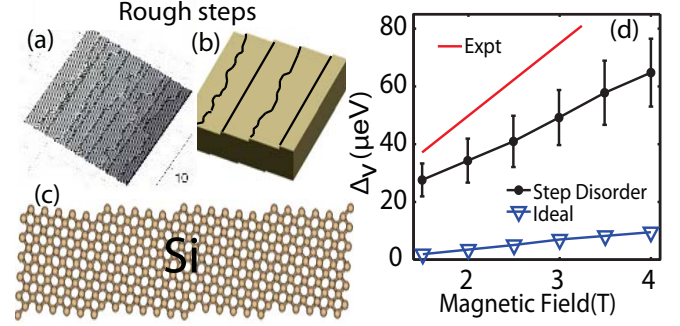


FIG. 72 (a) Experimental data from (Zandvriet and Elswijk, 1993) depicting the ordered, disordered steps on a slanted QW. (b) Model representation of such disordered steps. (c) Atomistic representation of a. 4.7 degree slanted wafer. The large slant angle is only used for visualization purposes here. The VS simulations use a 2 degree slant. (d) VS in samples of 2 degree slanted Si QWs with step disorder, without any explicit  $\text{Si}_x\text{Ge}_{1-x}$  buffer. The VS is increased over the ideal, non-disordered slanted QW results approaching the experimental data. The slope of the magnetic field dependence is not quite the same, however.

e. A slanted Si quantum well with disordered  $\text{Si}_x\text{Ge}_{1-x}$  buffer and disordered steps

The previous two subsections reviewed the effects of two different types of disorders: a) alloy disorder in the  $\text{Si}_x\text{Ge}_{1-x}$  buffer, and b) disorder in the slanted steps. Here we put these effects together. Figure 73 shows that when both disorder mechanisms, the disorder slant as well as the  $\text{Si}_x\text{Ge}_{1-x}$  alloy disorder are included in the model, one obtains statistical results that are very close to the experimental data. We therefore conclude there that the atomistic details such as step disorder in a slanted QW and alloy disorder in the  $\text{Si}_x\text{Ge}_{1-x}$  buffer are critical elements that determine the VS as observed in the experiment.

The overlap with the experimental data is quite surprising, considering that these model data utilize only previously published material parameters (Boykin *et al.*, 2007a, 2002, 2004b) and that no additional free parameters enter into this model other than the step correlation length that was taken from experimental data. The atomistic model domain is quite large with over 10 million atoms included in the strain domain and over 2 million atoms included in the subdomain of the Si QW and some additional layers in  $\text{Si}_x\text{Ge}_{1-x}$ . Details of these calculations can be found in Kharche, 2010 and Kharche *et al.*, 2007. From an atomistic modeling and simulation perspective we begin to argue now that the era of atomistic TCAD has arrived. We can demonstrate similar agreements with experimental data on other semi-

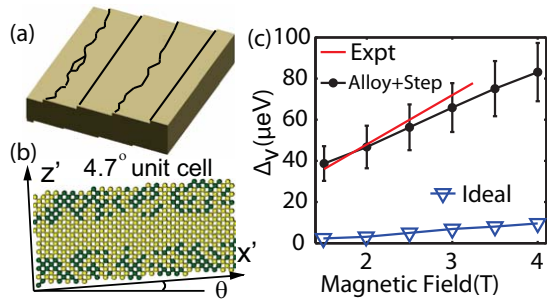


FIG. 73 (a) Model representation of ordered, disordered steps on a slanted QW. (b) Sketch of a 4.7 degree slanted QW with a SiGe buffer. The large slant angle is only used for visualization purposes here. The VS simulations use a 2 degree slant. (c) VS in samples of 2 degree slanted Si QWs with  $\text{Si}_x\text{Ge}_{1-x}$  disorder and slant disordered steps. The VS is increased over the ideal, non-disordered slanted QW results overlapping the experimental data. The slope of the magnetic field dependence is about the same as the experimental data.

conducting structures such as III-V quantum dots (Usman *et al.*, 2011a, 2009, 2011b), Phosphor-defined wires in Silicon (Weber *et al.*, 2012), and single Phosphorous impurities in silicon (Fuechsle *et al.*, 2011).

#### f. Flat disordered SiGe buffer - effects of system size

The previous subsections indicated that the detailed atomistic treatment of the  $\text{Si}_x\text{Ge}_{1-x}/\text{Si}$  interface plays a crucial role in the overall magnitude of the VS in slanted Si QW. Statistical sampling and averaging was performed to mimic larger domains. The statistical aspect of these VS fluctuations and magnetic field dependence begs the question: “How large does the system have to be, until these local fluctuations do no longer matter?” In this section we report the results of a numerical experiment (Jiang *et al.*, 2012) for a flat quantum well, where the lateral system size was increased systematically.

Sizes of realistic Si quantum dots vary with design and might range from active confinement areas of  $10 \times 10 \text{ nm}^2$  to  $40 \times 40 \text{ nm}^2$  or even larger. The natural question arises how large a quantum dot would have to be for disorder induced fluctuations to become negligible. Figure 74 explores the effects of the simulation cross section size on valley splitting. The fact that the lines in Fig. 74(a) are not flat is indicative that small systems clearly suffer from large sample to sample fluctuations such that the average is not even reaching the large system limit. Figure 74(b) indicates the decrease of the fluctuations as a function of lateral system size. Larger applied electric fields (i.e. 20MV/m versus 2MV/m) show significantly larger fluctuations supporting our argument that the wave functions explore more fluctuating state space in the SiGe buffer, since the larger electric fields push the wave function into the interface buffer stronger than the

weaker electric field.

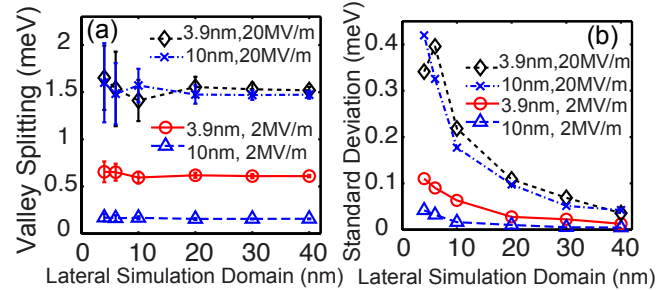


FIG. 74 VS as a function of the non-confining lateral simulation domain size for different quantum well thicknesses (in nm) and applied electric fields (in MV/m). (b) VS fluctuations as a simulation domain size.

#### g. Buffer fluctuations - conclusions

These results demonstrate that atomistic disorder is a critical element in the modeling of such Si QW buffered by disordered  $\text{Si}_x\text{Ge}_{1-x}$ . This analysis does, however, not shine much light on the reasons for these effects, nor does it provide a lot of physical intuition. The physical intuition that comes into play is that the wave functions in different samples will penetrate differently into interfaces for different interface disorder configurations.

The natural approach is to assume a constant medium for the SiGe buffer and derive explicit expressions for the VS as a function of barrier heights and effective masses (Boykin *et al.*, 2007b). While these continuum methods provide some general guidance, they depend heavily on the adjustment of mixing parameters and they do not seem to quantitatively agree with the statistical samples taken in an atomistic approach.

## REFERENCES

- Abe, E., A. Tyryshkin, S. Tojo, J. Morton, W. Witzel, A. Fujimoto, J. Ager, E. Haller, J. Isoya, S. Lyon, *et al.* (2010), *Physical Review B* **82** (12), 121201.
- Ager, J. W., J. W. Beeman, W. L. Hansen, E. E. Haller, I. D. Sharp, C. Liao, A. Yang, M. L. W. Thewalt, and H. Riemann (2005), *Journal of The Electrochemical Society* **152** (6), G448.
- Ahmed, H. (1997), *Journal of Vacuum Science & Technology B: Microelectronics and Nanometer Structures* **15**, 2101.
- Alhassid, Y. (2000), *Reviews of Modern Physics* **72**, 895.
- Ali, D., and H. Ahmed (1994), *Applied Physics Letters* **64** (16), 2119.
- Ando, T. (1979), *Physical Review B* **19** (6), 3089.
- Ando, T., A. B. Fowler, and F. Stern (1982), *Reviews of Modern Physics* **54** (2), 437.
- Andreas, B., Y. Azuma, G. Bartl, P. Becker, H. Bettin, M. Borys, I. Busch, M. Gray, P. Fuchs, K. Fujii, *et al.* (2011), *Physical Review Letters* **106**, 030801.

- Andresen, S. E. S., R. Brenner, C. J. Wellard, C. Yang, T. Hopf, C. C. Escott, R. G. Clark, A. S. Dzurak, D. N. Jamieson, and L. C. L. Hollenberg (2007), *Nano Letters* **7** (7), 2000.
- Andresen, S. E. S., *et al.* (2009), in *Electron spin resonance and related phenomena in low-dimensional structures*, Topics Appl. Physics, Vol. 115, pp. 169–182.
- Angus, S. J., A. J. Ferguson, A. S. Dzurak, and R. G. Clark (2007), *Nano Letters* **7** (7), 2051.
- Appelbaum, I., B. Huang, and D. Monsma (2007), *Nature* **447** (7142), 295.
- Asenov, A., A. R. Brown, J. H. Davies, S. Kaya, and G. Slavcheva (2003), *IEEE Transactions On Electron Devices* **50** (9), 1837.
- Askew, T. R., P. J. Muench, H. J. Stapleton, and K. L. Brower (1984), *Solid state communications* **49** (7), 667.
- Assali, L. V. C., H. M. Petrilli, R. B. Capaz, B. Koiller, X. Hu, and S. Das Sarma (2011), *Physical Review B* **83** (16), 165301.
- Averin, D. V., and Y. V. Nazarov (1990), *Physical Review Letters* **65** (19), 2446.
- Awschalom, D. D., and M. E. Flatté (2007), *Nature Physics* **3** (3), 153.
- Bardeen, J., and W. Shockley (1950), *Physical Review* **80** (1), 72.
- Baron, T., F. Martin, P. Mur, C. Wyon, and M. Dupuy (2000), *Journal of crystal growth* **209** (4), 1004.
- Barthel, C., D. J. Reilly, C. M. Marcus, M. P. Hanson, and A. C. Gossard (2009), *Physical Review Letters* **103** (16), 160503.
- Batra, A., C. D. Weis, J. Reijonen, A. Persaud, and T. Schenkel (2007), *Applied Physics Letters* **91** (19).
- Becker, P., H. Pohl, H. Riemann, and N. Abrosimov (2010), *Physica Status Solidi (a)* **207** (1), 49.
- Beenakker, C. W. J. (1991), *Physical Review B* **44** (4), 1646.
- Beenakker, C. W. J., and H. van Houten (1991), in *Solid State Physics: Advances in Research and Applications*, Vol. 44, edited by H. Ehrenreich and D. Turnbull (Academic Press, New York) pp. 1–228.
- Berer, T., D. Pachinger, G. Pillwein, M. Mühlberger, H. Lichtenberger, G. Brunthaler, and F. Schäffler (2006), *Applied Physics Letters* **88**, 162112.
- Berer, T., D. Pachinger, G. Pillwein, M. Mühlberger, H. Lichtenberger, G. Brunthaler, and F. Schäffler (2007), *Semiconductor Science and Technology* **22**, S137.
- van Beveren, L. H. W., H. Huebl, D. R. McCamey, T. Duty, A. J. Ferguson, R. G. Clark, and M. S. Brandt (2008), *Applied Physics Letters* **93**, 072102.
- Bielejec, E., J. A. Seamons, and M. S. Carroll (2010), *Nanotechnology* **21**, 085201.
- Blakemore, J. S. (1982), *Journal of Applied Physics* **53** (10), R123.
- Bluhm, H., S. Foletti, I. Neder, M. Rudner, D. Mahalu, V. Umansky, and A. Yacoby (2010), *Nature Physics* **7** (2), 109.
- Boehme, C., and K. Lips (2003), *Physical Review Letters* **91** (24), 246603.
- Boeuf, F., X. Jehl, M. Sanquer, and T. Skotnicki (2003), *Nanotechnology*, *IEEE Transactions on* **2** (3), 144 .
- Borhani, M., and X. Hu (2010), *Physical Review B* **82** (24), 241302.
- Borselli, M. G., K. Eng, E. T. Croke, B. M. Maune, B. Huang, R. S. Ross, A. A. Kiselev, P. W. Deelman, I. Alvarado-Rodriguez, A. E. Schmitz, M. Sokolich, K. S. Holabird, T. M. Hazard, M. F. Gyure, and A. T. Hunter (2011a), *Applied Physics Letters* **99**, 063109.
- Borselli, M. G., R. S. Ross, A. A. Kiselev, E. T. Croke, K. S. Holabird, P. W. Deelman, L. D. Warren, I. Alvarado-Rodriguez, I. Milosavljevic, F. C. Ku, W. S. Wong, A. E. Schmitz, M. Sokolich, M. F. Gyure, and A. T. Hunter (2011b), *Applied Physics Letters* **98**, 123118.
- Bowen, R., G. Klimeck, R. Lake, W. Frensley, and T. Moise (1997), *Journal of Applied Physics* **81**.
- Boykin, T., N. Kharche, and G. Klimeck (2007a), *Physical Review B* **76** (3).
- Boykin, T., N. Kharche, and G. Klimeck (2007b), *Physical Review B* **77** (24).
- Boykin, T., G. Klimeck, R. Bowen, and F. Oyafuso (2002), *Physical Review B* **66**.
- Boykin, T., G. Klimeck, M. Friesen, S. N. Coppersmith, P. Von Allmen, F. Oyafuso, and S. Lee (2004a), *Physical Review B* **70**.
- Boykin, T., G. Klimeck, and F. Oyafuso (2004b), *Physical Review B* **69**.
- Boykin, T., M. Luisier, M. Salmani-Jelodar, and G. Klimeck (2010), *Physical Review B* **81**.
- Boykin, T. B., G. Klimeck, P. V. Allmen, S. Lee, and F. Oyafuso (2005), *Journal of Applied Physics* **97** (11), 113702.
- Boykin, T. B., G. Klimeck, M. A. Eriksson, M. Friesen, S. N. Coppersmith, P. von Allmen, F. Oyafuso, and S. Lee (2004c), *Applied Physical Letters* **84**.
- Bradbury, F. R., A. M. Tyryshkin, G. Sabouret, J. Bokor, T. Schenkel, and S. A. Lyon (2006), *Physical Review Letters* **97**, 176404.
- Brower, K. L. (1989), *Semiconductor Science and Technology* **4**, 970.
- Buin, A. K., A. Verma, A. Svizhenko, and M. P. Anantram (2008), *Nano Letters* **8** (2), 760.
- Buttiker, M. (1988), *IBM Journal Of Research And Development* **32** (1), 63.
- Calderón, M. J., B. Koiller, and S. Das Sarma (2006a), *Physical Review B* **74** (4), 045310.
- Calderón, M. J., B. Koiller, and S. Das Sarma (2007), *Physical Review B* **75** (12).
- Calderón, M. J., B. Koiller, and S. Das Sarma (2008), *Physical Review B* **77** (15), 155302.
- Calderón, M. J., B. Koiller, X. Hu, and S. Das Sarma (2006b), *Physical Review Letters* **96** (9), 96802.
- Calderón, M. J., A. Saraiva, B. Koiller, and S. Das Sarma (2009), *Journal of Applied Physics* **105** (12).
- Calderón, M. J., J. Verduijn, G. P. Lansbergen, G. C. Tettamanzi, S. Rogge, and B. Koiller (2010a), *Physical Review B* **82** (7), 075317.
- Calderón, M. J., J. Verduijn, G. P. Lansbergen, G. C. Tettamanzi, S. Rogge, and B. Koiller (2010b), *Physical Review B* **82** (7), 075317.
- Calvet, L. E., J. P. Snyder, and W. Wernsdorfer (2011), *Physical Review B* **83** (20).
- Calvet, L. E., R. G. Wheeler, and M. A. Reed (2007a), *Physical Review B* **76** (3), 035319.
- Calvet, L. E., R. G. Wheeler, and M. A. Reed (2007b), *Physical Review Letters* **98** (9), 96805.
- Carter, D. J., N. A. Marks, O. Warschkow, and D. R. McKenzie (2011), *Nanotechnology* **22**, 065701.
- Carter, D. J., O. Warschkow, N. A. Marks, and D. R. McKenzie (2009), *Physical Review B* **79** (3), 033204.
- Chutia, S., S. N. Coppersmith, and M. Friesen (2008), *Physical Review B* **77** (19), 193311.

- Ciorga, M., A. S. Sachrajda, P. Hawrylak, C. Gould, P. Zawadzki, S. Jullian, Y. Feng, and Z. Wasilewski (2000), *Physical Review B* **61** (24), R16315.
- Cobden, D. H., M. Bockrath, P. L. McEuen, A. G. Rinzler, and R. E. Smalley (1998), *Physical Review Letters* **81**, 681.
- Cohen, M. L., and J. R. Chelikowsky (1988), *Electronic Structure and Optical Properties of Semiconductors*, Vol. 75 (Springer-Verlag).
- Cohen-Tannoudji, C., J. Dupont-Roc, and G. Grynberg (1992), *Atom-photon interactions: basic processes and applications* (Wiley Online Library).
- Coish, W. A., and F. Qassemi (2011), *Physical Review B* **84** (24), 245407.
- Cole, J. H., S. J. Devitt, and L. C. L. Hollenberg (2006), *Journal of Physics A: Mathematical and General* **39**, 14649.
- Colinge, C. A., W. Xiong, C. R. Cleavelin, and J. P. Colinge (2007), in *Nanoscaled semiconductor-on-Insulator Structures and Devices*, edited by S. Hall, S. Hall, A. Nazarov, and V. Lysenko (NATO) pp. 165–170.
- Copsey, D., M. Oskin, F. Impens, T. Metodiev, A. Cross, F. T. Chong, I. L. Chuang, and J. Kubiawicz (2003), *IEEE Journal Of Selected Topics In Quantum Electronics* **9** (6), 1552.
- Culcer, D., L. Cywiński, Q. Li, X. Hu, and S. Das Sarma (2009a), *Physical Review B* **80** (20), 205302.
- Culcer, D., L. Cywiński, Q. Li, X. Hu, and S. Das Sarma (2010a), *Physical Review B* **82**, 155312.
- Culcer, D., X. Hu, and S. Das Sarma (2009b), *Applied Physics Letters* **95** (7), 073102.
- Culcer, D., X. Hu, and S. Das Sarma (2010b), *Physical Review B* **82**, 205315.
- Culcer, D., A. L. Saraiva, B. Koiller, X. Hu, and S. Das Sarma (2012), *Physical Review Letters* **108**, 126804.
- Cullis, P. R., and J. R. Marko (1970), *Physical Review B - Solid State* **1** (2), 632.
- Das Sarma, S., X. Wang, and S. Yang (2011), *Physical Review B* **83** (23), 235314.
- Dash, S. P., S. Sharma, R. S. Patel, M. P. De Jong, and R. Jansen (2009), *Nature* **462** (7272), 491.
- Davies, J. H. (1998), *The Physics of Low-Dimensional Semiconductors* (Cambridge University Press, Cambridge, UK).
- De Sousa, R. (2007), *Physical Review B* **76** (24), 245306.
- De Sousa, R., and S. Das Sarma (2003), *Physical Review B* **68** (11), 115322.
- De Sousa, R., J. D. Delgado, and S. Das Sarma (2004), *Physical Review A* **70** (5), 052304.
- De Sousa, R., X. Hu, and S. Das Sarma (2001), *Physical Review A* **64**, 042307.
- De Sousa, R., C. C. Lo, and J. Bokor (2009), *Physical Review B* **80** (4), 045320.
- Debernardi, A., A. Baldereschi, and M. Fanciulli (2006), *Physical Review B* **74** (3), 35202.
- Devitt, S. J., J. H. Cole, and L. C. L. Hollenberg (2006), *Physical Review A* **73** (5), 052317.
- DiVincenzo, D. P. (1998), *Nature* **393**, 113.
- DiVincenzo, D. P. (2000), *Fortschritte Der Physik-Progress Of Physics* **48** (9-11), 771.
- Dresselhaus, G. (1955), *Physical Review* **100** (2), 580.
- Drumm, D. W., A. Budi, M. C. Per, S. P. Russo, and L. C. L. Hollenberg (2012), *Arxiv preprint arXiv:1201.3751*.
- Dutta, A., S. Oda, Y. Fu, and M. Willander (2000), *Japanese Journal of Applied Physics* **39**, 4647.
- Eaglesham, D., and M. Cerullo (1990), *Physical Review Letters* **64** (16), 1943.
- Eigler, D. M., and E. K. Schweizer (1990), *Nature* **344** (6266), 524.
- Elzerman, J. M., R. Hanson, L. H. W. van Beveren, B. Witkamp, L. M. K. Vandersypen, and L. P. Kouwenhoven (2004), *Nature* **430** (6998), 431.
- Eng, K., R. N. McFarland, and B. E. Kane (2005), *Applied Physics Letters* **87** (5), 052106.
- Eng, K., R. N. McFarland, and B. E. Kane (2007), *Physical Review Letters* **99**, 016801.
- Eriksson, M. A., M. Friesen, S. N. Coppersmith, R. Joynt, L. J. Klein, K. A. Slinker, C. Tahan, P. M. Mooney, J. O. Chu, and S. J. Koester (2004), *Quant. Inf. Proc.* **3**, 133.
- Escott, C. C., F. A. Zwanenburg, and A. Morello (2010), *Nanotechnology* **21** (27).
- Fang, A., Y. Chang, and J. Tucker (2002), *Physical Review B* **66** (15).
- Fang, A., Y. C. Chang, and J. R. Tucker (2005), *Physical Review B* **72** (7), 075355.
- Fano, U. (1961), *Physical Review* **124**, 1866.
- Feher, G. (1959), *Physical Review* **114** (5), 1219.
- Feher, G., and E. A. Gere (1959), *Physical Review* **114** (5), 1245.
- Field, M., C. G. Smith, M. Pepper, D. A. Ritchie, J. E. F. Frost, G. A. C. Jones, and D. G. Hasko (1993), *Physical Review Letters* **70** (9), 1311.
- Field, S. B., M. A. Kastner, U. Meirav, J. H. F. Scott-Thomas, D. A. Antoniadis, H. Smith, and S. J. Wind (1990), *Physical Review B* **42** (6), 3523.
- Foletti, S., H. Bluhm, D. Mahalu, V. Umansky, and A. Yacoby (2009), *Nature Physics* **5** (12), 903.
- Fowler, A. B., J. J. Wainer, and R. A. Webb (1988), *IBM Journal of Research and Development* **32** (3), 372.
- Fowler, A. G., C. J. Wellard, and L. C. L. Hollenberg (2003), *Physical Review A* **67** (1), 012301.
- Friesen, M. (2005), *Physical Review Letters* **94** (18), 186403.
- Friesen, M., S. Chutia, C. Tahan, and S. N. Coppersmith (2007), *Physical Review B* **75**, 115318.
- Friesen, M., and S. N. Coppersmith (2010), *Physical Review B* **81** (11), 115324.
- Friesen, M., M. A. Eriksson, and S. N. Coppersmith (2006), *Applied Physics Letters* **89**, 202106.
- Friesen, M., P. Rugheimer, D. E. Savage, M. G. Lagally, D. W. Van Der Weide, R. Joynt, and M. A. Eriksson (2003), *Physical Review B* **67** (12), 121301.
- Fritzsche, H. (1962), *Physical Review* **125**, 1560.
- Fuchsle, M., S. Mahapatra, F. A. Zwanenburg, M. Friesen, M. A. Eriksson, and M. Y. Simmons (2010), *Nature Nanotechnology* **5** (7), 502.
- Fuchsle, M., J. Miwa, S. Mahapatra, H. Ryu, S. Lee, O. Warschkow, L. C. L. Hollenberg, G. Klimeck, and M. Y. Simmons (2011), *Nature Nanotechnology*.
- Fuhrer, A., M. Fuchsle, T. C. G. Reusch, B. Weber, and M. Y. Simmons (2009), *Nano Letters* **9** (2), 707.
- Fujiwara, A., H. Inokawa, K. Yamazaki, H. Namatsu, Y. Takahashi, N. M. Zimmerman, and S. B. Martin (2006), *Applied Physics Letters* **88** (5), 053121.
- Fujiwara, A., Y. Takahashi, and K. Murase (1997), *Physical Review Letters* **78** (8), 1532.
- Fulton, T. A., and G. J. Dolan (1987), *Physical Review Letters* **59** (1), 109.
- Gamble, J. K., M. Friesen, S. N. Coppersmith, and X. Hu (2012), *Arxiv preprint arXiv:1203.6332*.
- Gerstmann, U. (2011), *Physica Status Solidi B-Basic Solid State Physics* **248** (6), 1319.



- Ghosh, R. N., and R. H. Silsbee (1992), *Physical Review B* **46** (19), 12508.
- Glavin, B. A., and K. W. Kim (2003), *Physical Review B* **68** (4), 045308.
- Glazman, L. I., and M. Pustilnik (2003), in *New Directions in Mesoscopic Physics (Towards Nanoscience)*, edited by F. Fazio, V. Gantmakher, and Y. Imry (Kluwer, Dordrecht) pp. 93–115.
- Goan, H. S. (2005), *International Journal of Quantum Information* **3** (3), 27.
- Goldhaber-Gordon, D., J. Gores, M. Kastner, H. Shtrikman, D. Mahalu, and U. Meirav (1998), *Physical Review Letters* **81** (23), 5225.
- Golovach, V. N., M. Borhani, and D. Loss (2006), *Physical Review B* **74** (16), 165319.
- Golovach, V. N., X. Jehl, M. Houzet, M. Pierre, B. Roche, M. Sanquer, and L. I. Glazman (2011), *Physical Review B* **83** (7), 075401.
- Gordon, J. P., and K. D. Bowers (1958), *Physical Review Letters* **1** (10), 368.
- Gorman, J., D. G. Hasko, and D. A. Williams (2005), *Physical Review Letters* **95** (9), 90502.
- Goswami, S., K. A. Slinker, M. Friesen, L. M. McGuire, J. L. Truitt, C. Tahan, L. J. Klein, J. O. Chu, P. M. Mooney, D. W. Van Der Weide, R. Joynt, S. N. Coppersmith, and M. A. Eriksson (2007), *Nature Physics* **3** (1), 41.
- Grabert, H., M. H. Devoret, and M. Kastner (1993), *Physics Today* **46**, 62.
- Green, M. A. (1990), *Journal of Applied Physics* **67** (6), 2944.
- Greenland, P. T., S. A. Lynch, A. F. G. Van der Meer, B. N. Murdin, C. R. Pidgeon, B. Redlich, N. Q. Vinh, and G. Aepli (2010), *Nature* **465** (7301), 1057.
- Greentree, A. D., J. H. Cole, A. R. Hamilton, and L. C. L. Hollenberg (2004), *Physical Review B* **70** (23).
- Hada, Y., and M. Eto (2003), *Physical Review B* **68** (15), 155322.
- Hanson, R., L. P. Kouwenhoven, J. R. Petta, S. Tarucha, and L. M. K. Vandersypen (2007), *Reviews of Modern Physics* **79** (4), 1217.
- Hao, Y. L., A. P. Djotyan, A. A. Avetisyan, and F. M. Peeters (2009), *Physical Review B* **80** (3), 035329.
- Hao, Y. L., A. P. Djotyan, A. A. Avetisyan, and F. M. Peeters (2011), *Journal Of Physics-Condensed Matter* **23** (11), 115303.
- Hasegawa, H. (1960), *Physical Review* **118** (6), 1523.
- Hayes, R. R., A. A. Kiselev, M. G. Borselli, S. S. Bui, E. T. Croke III, P. W. Deelman, B. M. Maune, I. Milosavljevic, J. S. Moon, R. S. Ross, A. E. Schmitz, M. F. Gyure, and A. T. Hunter (2009), *Arxiv preprint arXiv:0908.0173*.
- Herring, C., and M. Flicker (1964), *Physical Review* **134**, A362.
- Herring, C., and E. Vogt (1956), *Physical Review* **101** (3), 944.
- Hill, C. D. (2007), *Physical Review Letters* **98** (18), 180501.
- Hill, C. D., and H. S. Goan (2003), *Physical Review A* **68** (1), 012321.
- Hill, C. D., and H. S. Goan (2004), *Physical Review A* **70** (2), 022310.
- Hill, C. D., L. C. L. Hollenberg, A. G. Fowler, C. J. Wellard, A. D. Greentree, and H.-S. Goan (2005), *Physical Review B* **72** (4), 045350.
- Hofheinz, M., X. Jehl, M. Sanquer, G. Molas, M. Vinet, and S. Deleonibus (2006a), *European Physical Journal B* **54** (3), 299.
- Hofheinz, M., X. Jehl, M. Sanquer, G. Molas, M. Vinet, and S. Deleonibus (2006b), *Applied Physics Letters* **89**, 143504.
- Hofmann, F., T. Heinzl, D. Wharam, J. Kotthaus, G. Böhm, W. Klein, G. Tränkle, and G. Weimann (1995), *Physical Review B* **51** (19), 13872.
- Hollenberg, L. C. L., A. S. Dzurak, C. Wellard, A. R. Hamilton, D. J. Reilly, G. J. Milburn, and R. G. Clark (2004), *Physical Review B* **69** (11), 113301.
- Hollenberg, L. C. L., A. D. Greentree, A. G. Fowler, and C. J. Wellard (2006), *Physical Review B* **74** (4).
- Hu, X., and S. Das Sarma (2006), *Physical Review Letters* **96** (10), 100501.
- Hu, X., B. Koiller, and S. Das Sarma (2005), *Physical Review B* **71** (23), 235332.
- Hu, X., R. de Sousa, and S. Das Sarma (2001), *Physical Review Letters* **86**, 918.
- Hu, Y., H. O. H. Churchill, D. J. Reilly, J. Xiang, C. M. Lieber, and C. M. Marcus (2007), *Nature Nanotechnology* **2** (10), 622.
- Hu, Y., F. Kuemmeth, C. M. Lieber, and C. M. Marcus (2011), *Nature Nanotechnology*.
- Hudson, F. E., A. J. Ferguson, C. C. Escott, C. Yang, D. N. Jamieson, R. G. Clark, and A. S. Dzurak (2008), *Nanotechnology* **19** (19).
- Huebl, H., F. Hoehne, B. Grolik, A. Stegner, M. Stutzmann, and M. Brandt (2008), *Physical Review letters* **100** (17), 177602.
- Huebl, H., C. Nugroho, A. Morello, C. Escott, M. Eriksson, C. Yang, D. Jamieson, R. Clark, and A. Dzurak (2010), *Physical Review B* **81** (23), 235318.
- Hüttel, A. K., H. Qin, A. W. Holleitner, R. H. Blick, K. Neumaier, D. Weinmann, K. Eberl, and J. P. Kotthaus (2003), *Europhysics Letters* **62**, 712.
- Ishikuro, H., T. Fujii, T. Saraya, G. Hashiguchi, T. Hiramoto, and T. Ikoma (1996), *Applied Physics Letters* **68** (25), 3585.
- ITRS, (2011), “International technology roadmap for semiconductors,” <http://www.itrs.net>.
- Ivey, J. L., and R. L. Miehler (1975a), *Physical Review B* **11** (2), 822.
- Ivey, J. L., and R. L. Miehler (1975b), *Physical Review B* **11** (2), 849.
- Jamieson, D. N., C. Yang, T. Hopf, S. M. Hearne, C. I. Pakes, S. Praver, M. Mitic, E. Gauja, S. E. Andresen, F. E. Hudson, A. S. Dzurak, and R. G. Clark (2005), *Applied Physics Letters* **86** (20), 202101.
- Jansen, R. (2012), *Nature Materials* **11** (5), 400.
- Jantsch, W., Z. Wilamowski, N. Sandersfeld, and F. Schäffler (1998), *Physica Status Solidi (b)* **210** (2), 643.
- Jiang, Z., N. Kharche, T. Boykin, and G. Klimeck (2012), *Applied Physical Letters* **100** (10).
- Johnson, A. C., J. R. Petta, C. M. Marcus, M. P. Hanson, and A. C. Gossard (2005a), *Physical Review B* **72**, 165308.
- Johnson, A. C., J. R. Petta, J. M. Taylor, A. Yacoby, M. D. Lukin, C. M. Marcus, M. P. Hanson, and A. C. Gossard (2005b), *Nature* **435** (7044), 925.
- Johnson, B. C., G. C. Tettamanzi, A. D. C. Alves, S. Thompson, C. Yang, J. Verduijn, J. A. Mol, R. Wacquez, M. Vinet, M. Sanquer, S. Rogge, and D. N. Jamieson (2010), *Applied Physics Letters* **96** (26).
- Kalmeyer, V., and R. B. Laughlin (1987), *Physical Review B* **35**, 9805.
- Kandasamy, G., C. J. Wellard, and L. C. L. Hollenberg (2006), *Nanotechnology* **17** (18), 4572.

- Kane, B. (2000), Fortschritte Der Physik-Progress of Physics **48** (9-11), 1023.
- Kane, B. E. (1998), Nature **393** (6681), 133.
- Kane, B. E. (2005), MRS Bulletin **30** (2), 105.
- Katsaros, G., V. N. Golovach, P. Spathis, N. Ares, M. Stoffel, F. Fournel, O. G. Schmidt, L. I. Glazman, and S. De Franceschi (2011), Physical Review Letters **107** (24), 246601.
- Katsaros, G., P. Spathis, M. Stoffel, F. Fournel, M. Mongillo, V. Bouchiat, F. Lefloch, A. Rastelli, O. G. Schmidt, and S. De Franceschi (2010), Nature Nanotechnology **5** (6), 458.
- Katsaros, G., J. Tersoff, M. Stoffel, A. Rastelli, P. Acosta-Diaz, G. S. Kar, G. Costantini, O. G. Schmidt, and K. Kern (2008), Physical Review Letters **101** (9), 96103.
- Kerridge, A., S. Savory, A. H. Harker, *et al.* (2006), Journal of Physics - Condensed Matter **18** (21), S767.
- Kettle, L. M., H. S. Goan, and S. C. Smith (2006), Physical Review B **73** (11), 115205.
- Kettle, L. M., H. S. Goan, S. C. Smith, C. J. Wellard, L. C. L. Hollenberg, and C. I. Pakes (2003), Physical Review B **68** (7), 75317.
- Kettle, L. M., H. S. Goan, S. C. Smith, *et al.* (2004), Journal of Physics - Condensed Matter **16** (7), 1101.
- Khaetskii, A., and Y. Nazarov (2000), Physical Review B **61** (19), 12639.
- Khalafalla, M. A. H., Y. Ono, K. Nishiguchi, and A. Fujiwara (2009), Applied Physics Letters **94** (22), 223501.
- Kharche, N. (2010), *Atomistic Modeling of Electronic Structure and Transport in Disordered Nanostructures*, Ph.D. thesis.
- Kharche, N., M. Luisier, T. Boykin, and G. Klimeck (2008), Journal of Computational Electronics **2** (3).
- Kharche, N., M. Prada, T. B. Boykin, and G. Klimeck (2007), Applied Physical Letters **90**.
- Khrapai, V. S., A. A. Shashkin, and V. T. Dolgoplov (2003), Physical Review B **67** (11), 113305.
- Kittel, C. (1963), *Quantum Theory of Solids* (John Wiley and Sons, New York).
- Klauder, J., and P. Anderson (1962), Physical Review **125** (3), 912.
- Klein, L. J., K. L. M. Lewis, K. A. Slinker, S. Goswami, D. W. Van der Weide, R. H. Blick, P. M. Mooney, J. O. Chu, S. N. Coppersmith, M. Friesen, and M. A. Eriksson (2006), Journal of Applied Physics **99**, 023509.
- Klein, L. J., D. E. Savage, and M. A. Eriksson (2007), Applied Physics Letters **90**, 033103.
- Klein, L. J., K. A. Slinker, J. L. Truitt, S. Goswami, K. L. M. Lewis, S. N. Coppersmith, D. W. van der Weide, M. Friesen, R. H. Blick, D. E. Savage, M. G. Lagally, C. Tahan, R. Joynt, M. A. Eriksson, J. O. Chu, J. A. Ott, and P. M. Mooney (2004), Applied Physics Letters **84**, 4047.
- Klimeck, G., S. Ahmed, N. Kharche, M. Korkusinski, M. Usman, M. Prada, and T. Boykin (2007), Special Issue on Nanoelectronic Device Modeling **54** (9).
- Klimeck, G., R. Bowen, T. Boykin, and T. Cwik (2000a), Superlattices and Microstructures **27**, 519.
- Klimeck, G., R. Bowen, T. Boykin, C. Salazar-Lazaro, T. Cwik, and A. Stoica (2000b), Superlattices and Microstructures **27** (2/3), 77.
- Klimeck, G., R. Lake, R. Bowen, W. Frensley, and D. Blanks (1995), 1995 53rd Device Research Conference, Charlottesville, VA, June 19-21, 1995.
- Klimeck, G., F. Oyafuso, T. Boykin, R. Bowen, and P. Allen (2002), Computer Modeling in Engineering and Science **3** (5).
- Kloeffel, C., M. Trif, and D. Loss (2011), Physical Review B **84** (19), 195314.
- Koester, S. J., K. Ismail, and J. O. Chu (1997), Semiconductor science and technology **12**, 384.
- Koh, T. S., C. Simmons, M. Eriksson, S. Coppersmith, and M. Friesen (2011), Physical Review Letters **106**, 186801.
- Köhler, H., and M. Roos (1979), Physica Status Solidi (b) **91** (1), 233.
- Kohn, W., and J. M. Luttinger (1955a), Physical Review **98** (4), 915.
- Kohn, W., and J. M. Luttinger (1955b), Physical Review **98**, 915.
- Koiller, B., R. B. Capaz, X. D. Hu, *et al.* (2004), Physical Review B **70** (11), 115207.
- Koiller, B., and X. Hu (2005), Nanotechnology, IEEE Transactions on **4** (1), 113.
- Koiller, B., X. Hu, and S. Das Sarma (2001), Physical Review Letters **88** (2), 027903.
- Koiller, B., X. D. Hu, and S. Das Sarma (2002a), Physical Review Letters **88** (2), 027903.
- Koiller, B., X. D. Hu, and S. Das Sarma (2002b), Physical Review B **66** (11), 115201.
- Koiller, B., X. D. Hu, H. D. Drew, *et al.* (2003), Physical Review Letters **90** (6), 067401.
- Koppens, F. H. L., C. Buizert, K. J. Tielrooij, I. T. Vink, K. C. Nowack, T. Meunier, L. P. Kouwenhoven, and L. M. K. Vandersypen (2006), Nature **442** (7104), 766.
- Koppens, F. H. L., J. A. Folk, J. M. Elzerman, R. Hanson, L. H. W. van Beveren, I. T. Vink, H. P. Tranitz, W. Wegscheider, L. P. Kouwenhoven, and L. M. K. Vandersypen (2005), Science **309**, 1346.
- Kouwenhoven, L. P., D. G. Austing, and S. Tarucha (2001), Reports on Progress in Physics **64** (6), 701.
- Kouwenhoven, L. P., C. M. Marcus, P. L. McEuen, S. Tarucha, R. M. Westervelt, and N. S. Wingreen (1997a), in *Mesoscopic electron transport*, Vol. 345, edited by L. Sohn, L. Kouwenhoven, and G. Schon (Kluwer Academic Publishers, Dordrecht, The Netherlands) p. 105.
- Kouwenhoven, L. P., T. H. Oosterkamp, M. W. S. Danoastro, M. Eto, D. G. Austing, T. Honda, and S. Tarucha (1997b), Science **278**, 1788.
- Kravchenko, S., and M. Sarachik (2004), Reports on Progress in Physics **67**, 1.
- Ladd, T. D., F. Jelezko, R. Laflamme, Y. Nakamura, C. Monroe, and J. L. O'Brien (2010), Nature **464** (7285), 45.
- Lai, K., T. M. Lu, W. Pan, D. C. Tsui, S. Lyon, J. Liu, Y. H. Xie, M. Mühlberger, and F. Schäffler (2006), Physical Review B **73** (16), 161301(R).
- Lai, K., W. Pan, D. C. Tsui, S. Lyon, M. Mühlberger, and F. Schäffler (2004), Physical Review Letters **93**, 156805.
- Lai, K., P. D. Ye, W. Pan, D. C. Tsui, S. A. Lyon, M. Mühlberger, and F. Schäffler (2005), Applied Physics Letters **87** (14), 142103.
- Lai, N. S., W. H. Lim, C. H. Yang, F. A. Zwanenburg, W. A. Coish, F. Qassemi, A. Morello, and A. S. Dzurak (2011), Scientific reports **1**.
- Lansbergen, G. P. (2010), *Electron transport through single donors in silicon*, Ph.D. thesis (Kavli Institute of Nanoscience Delft, Delft University of Technology, The Netherlands).
- Lansbergen, G. P., Y. Ono, and A. Fujiwara (2012), Nano Letters **12** (2), 763.

- Lansbergen, G. P., R. Rahman, J. Verduijn, G. C. Tettamanzi, N. Collaert, S. Biesemans, G. Klimeck, and S. Rogge (2011), *Physical Review Letters* **107**, 136602.
- Lansbergen, G. P., R. Rahman, C. J. Wellard, I. Woo, J. Caro, N. Collaert, S. Biesemans, G. Klimeck, L. C. L. Hollenberg, and S. Rogge (2008), *Nature Physics* **4** (8), 656.
- Lansbergen, G. P., G. C. Tettamanzi, and J. Verduijn (2010), *Nano Letters* **10**, 455.
- Larionov, A. A., F. L. E., A. A. Kokin, and K. A. Valiev (2000), *Nanotechnology* **11** (4), 392.
- Larionov, A. A., L. E. Fedichkin, and K. A. Valiev (2001), *Nanotechnology* **12**, 536.
- Larsen, D. M. (1981), *Physical Review B* **23** (10), 5521.
- Larsen, D. M., and S. Y. McCann (1992), *Physical Review B* **46** (7), 3966.
- Lauhon, L. J., M. S. Gudiksen, D. Wang, and C. M. Lieber (2002), *Nature* **420** (6911), 57.
- Lee, S., H. Ryu, H. Campbell, L. C. L. Hollenberg, M. Y. Simmons, and G. Klimeck (2011), *Physical Review B* **84** (20), 205309.
- Leobandung, E., L. Guo, Y. Wang, and S. Chou (1995), *Applied Physics Letters* **67** (7), 938.
- Leu, P. W., B. Shan, and K. Cho (2006), *Physical Review B* **73** (19), 195320.
- Levy, J. (2002), *Physical Review Letters* **89** (14), 147902.
- Li, Q., L. Cywinski, D. Culcer, X. Hu, and S. Das Sarma (2010), *Physical Review B* **81**, 085313.
- Likharev, K. (1999), *Proceedings of the IEEE* **87** (4), 606.
- Lim, W. H., H. Huebl, L. H. W. van Beveren, S. Rubanov, P. G. Spizzirri, S. J. Angus, R. G. Clark, and A. S. Dzurak (2009a), *Applied Physics Letters* **94**, 173502.
- Lim, W. H., C. H. Yang, F. A. Zwanenburg, and A. S. Dzurak (2011), *Nanotechnology* **22**, 335704.
- Lim, W. H., F. A. Zwanenburg, H. Huebl, M. Möttönen, K. W. Chan, A. Morello, and A. S. Dzurak (2009b), *Applied Physics Letters* **95**, 242102.
- Liu, H., T. Fujisawa, H. Inokawa, Y. Ono, A. Fujiwara, and Y. Hirayama (2008a), *Applied Physics Letters* **92** (22).
- Liu, H. W., T. Fujisawa, Y. Ono, H. Inokawa, A. Fujiwara, K. Takashina, and Y. Hirayama (2008b), *Physical Review B* **77** (7), 73310.
- Lloyd, S. (1993), *Science* **261** (5128), 1569.
- Lo, C. C., J. Bokor, T. Schenkel, A. M. Tyryshkin, and S. A. Lyon (2007), *Applied Physics Letters* **91** (24).
- Lo, C. C., A. Persaud, S. Dhuey, D. Olynick, F. Borondics, M. C. Martin, H. A. Bechtel, J. Bokor, and T. Schenkel (2009), *Semiconductor Science and Technology* **24**, 105022.
- Loss, D., and D. P. DiVincenzo (1998), *Physical Review A* **57** (1), 120.
- Lu, J., F. Hoehne, A. Stegner, L. Dreher, M. Stutzmann, M. Brandt, and H. Huebl (2011), *Physical Review B* **83** (23), 235201.
- Lu, T., J. Liu, J. Kim, K. Lai, D. Tsui, and Y. Xie (2007), *Applied Physics Letters* **90**, 182114.
- Lu, T., D. Tsui, C. Lee, and C. Liu (2009), *Applied Physics Letters* **94**, 182102.
- Lu, W., J. Xiang, B. P. Timko, Y. Wu, and C. M. Lieber (2005), *Proceedings of the National Academy of Sciences of the United States of America* **102** (29), 10046.
- Lyding, J. W., T. C. Shen, J. S. Hubacek, J. R. Tucker, and G. C. Abeln (1994), *Applied Physics Letters* **64** (15), 2010.
- Lyo, I. W., and P. Avouris (1990), *Journal Of Chemical Physics* **93** (6), 4479.
- Macmillen, D. B., and U. Landman (1984), *Physical Review B* **29** (8), 4524.
- Mahapatra, S., H. Buech, and M. Y. Simmons (2011), *Nano Letters* **11** (10), 4376.
- Majorana, E. (1937), *Il Nuovo Cimento* (1924-1942) **14** (4), 171.
- Martin, I., D. Mozysky, and H. W. Jiang (2003), *Physical Review Letters* **90** (1), 18301.
- Martins, A. S., T. B. Boykin, G. Klimeck, and B. Koiller (2005), *Physical Review B* **72** (19), 193204.
- Martins, A. S., R. B. Capaz, and B. Koiller (2004), *Physical Review B* **69** (8), 85320.
- Matsuoka, H., T. Ichiguchi, T. Yoshimura, and E. Takeda (1994), *Applied Physics Letters* **64** (5), 586.
- Matsuoka, H., and S. Kimura (1995), *Applied Physics Letters* **66**, 613.
- Maune, B. M., M. G. Borselli, B. Huang, T. D. Ladd, P. W. Deelman, K. S. Holabird, A. A. Kiselev, I. Alvarado-Rodriguez, R. S. Ross, A. E. Schmitz, M. Sokolich, C. A. Watson, M. F. Gyure, and A. T. Hunter (2012), *Nature* **481** (7381), 344.
- McCamey, D. R., H. Huebl, M. S. Brandt, W. D. Hutchison, J. C. McCallum, R. G. Clark, and A. R. Hamilton (2006), *Applied Physics Letters* **89**, 182115.
- McCamey, D. R., J. Van Tol, G. W. Morley, and C. Boehme (2010), *Science* **330** (6011), 1652.
- McGuire, L. M., M. Friesen, K. A. Slinker, S. N. Coppersmith, and M. A. Eriksson (2010), *New Journal of Physics* **12**, 033039.
- Medeiros-Ribeiro, G., A. M. Bratkovski, T. I. Kamins, D. A. A. Ohlberg, and R. S. Williams (1998), *Science* **279** (5349), 353.
- Meir, Y., and N. S. Wingreen (1993), *Physical Review Letters* **70**, 2601.
- Meirav, U., and E. B. Foxman (1996), *Semiconductor Science and Technology* **11**, 255.
- Meirav, U., M. A. Kastner, and S. J. Wind (1990), *Physical Review Letters* **65** (6), 771.
- Mitic, M., K. D. Petersson, M. C. Cassidy, R. P. Starrett, E. Gauja, A. J. Ferguson, C. Yang, D. N. Jamieson, R. G. Clark, and A. S. Dzurak (2008), *Nanotechnology* **19** (26).
- Mizuno, T., J. Okamura, and A. Toriumi (1994), *IEEE Transactions On Electron Devices* **41** (11), 2216.
- Mo, Y. W., D. E. Savage, B. S. Swartzentruber, and M. G. Lagally (1990), *Physical Review Letters* **65** (8), 1020.
- Mongillo, M., P. Spathis, G. Katsaros, P. Gentile, M. Sanquer, and S. De Franceschi (2011), *ACS nano*.
- Mooney, P. (1996), *Materials Science and Engineering: R: Reports*.
- Morales, A. M., and C. M. Lieber (1998), *Science* **279** (5348), 208.
- Morello, A., C. C. Escott, H. Huebl, L. H. W. van Beveren, L. C. L. Hollenberg, D. N. Jamieson, A. S. Dzurak, and R. G. Clark (2009), *Physical Review B* **80** (8).
- Morello, A., J. J. Pla, F. A. Zwanenburg, K. W. Chan, K. Y. Tan, H. Huebl, M. Möttönen, C. D. Nugroho, C. Yang, J. A. van Donkelaar, *et al.* (2010), *Nature* **467** (7316), 687.
- Morello, A., P. C. E. Stamp, and I. S. Tupitsyn (2006), *Physical Review Letters* **97** (20), 207206.
- Morton, J. J. L., D. R. McCamey, M. A. Eriksson, and S. A. Lyon (2011), *Nature* **479** (7373), 345.
- Morton, J. J. L., A. M. Tyryshkin, R. M. Brown, S. Shankar, B. W. Lovett, A. Ardavan, T. Schenkel, E. E. Haller, J. W. Ager, and S. A. Lyon (2008), *Nature* **455** (7216), 1085.
- Möttönen, M., K. Y. Tan, K. W. Chan, F. A. Zwanenburg,

- W. H. Lim, C. C. Escott, J. M. Pirkkalainen, A. Morello, C. Yang, J. A. van Donkelaar, A. D. C. Alves, D. N. Jamieson, L. C. L. Hollenberg, and A. S. Dzurak (2010), *Physical Review B* **81** (16), 161304.
- Nabors, K., and J. White (1991), *IEEE Transactions On Computer-Aided Design Of Integrated Circuits And Systems* **10** (11), 1447.
- Nadj-Perge, S., S. M. Frolov, E. Bakkers, and L. P. Kouwenhoven (2010), *Nature* **468** (7327), 1084.
- Nazarov, Y. V., and Y. M. Blanter (2009), *Quantum Transport* (Cambridge University Press).
- Nestoklon, M. O., L. E. Golub, and E. L. Ivchenko (2006), *Physical Review B* **73** (23), 235334.
- Nicholas, R. J., K. von Klitzing, and T. Englert (1980), *Solid State Communications* **34** (1), 51.
- Nielsen, M. A., and I. L. Chuang (2000), *Quantum Computation and Quantum information* (Cambridge University Press).
- Niquet, Y. M., A. Lherbier, N. H. Quang, M. V. Fernández-Serra, X. Blase, and C. Delerue (2006), *Physical Review B* **73** (16).
- Nordberg, E. P., G. A. T. Eyck, H. L. Stalford, R. P. Muller, R. W. Young, K. Eng, L. A. Tracy, K. D. Childs, J. R. Wendt, R. K. Grubbs, J. Stevens, M. P. Lilly, M. A. Eriksson, and M. S. Carroll (2009a), *Physical Review B* **80**, 115331.
- Nordberg, E. P., H. L. Stalford, R. Young, G. A. T. Eyck, K. Eng, L. A. Tracy, K. D. Childs, J. R. Wendt, R. K. Grubbs, J. Stevens, M. P. Lilly, M. A. Eriksson, and M. S. Carroll (2009b), *Applied Physics Letters* **95**, 202102.
- Notargiacomo, A., L. Di Gaspare, G. Scappucci, G. Mariottini, F. Evangelisti, E. Giovine, and R. Leoni (2003), *Applied Physics Letters* **83**, 302.
- Nowack, K. C., F. H. L. Koppens, Y. V. Nazarov, and L. M. K. Vandersypen (2007), *Science* **318**, 1430.
- Ohkawa, F. J., and Y. Uemura (1977a), *Journal of the Physical Society of Japan* **43** (3), 907.
- Ohkawa, F. J., and Y. Uemura (1977b), *Journal of the Physical Society of Japan* **43** (3), 917.
- Ono, K., D. G. Austing, Y. Tokura, and S. Tarucha (2002), *Science* **297** (5585), 1313.
- Ono, Y., A. Fujiwara, K. Nishiguchi, H. Inokawa, and Y. Takahashi (2005), *Journal of Applied Physics* **97**, 031101.
- Ono, Y., M. A. H. Khalafalla, K. Nishiguchi, K. Takashina, A. Fujiwara, S. Horiguchi, H. Inokawa, and Y. Takahashi (2008), *Applied Surface Science* **254** (19), 6252.
- Ono, Y., K. Nishiguchi, A. Fujiwara, H. Yamaguchi, H. Inokawa, and Y. Takahashi (2007), *Applied Physics Letters* **90**, 102106.
- Otobe, M., H. Yajima, and S. Oda (1998), *Applied Physics Letters* **72**, 1089.
- Overhof, H., and U. Gerstmann (2004), *Physical Review Letters* **92** (8), 087602.
- Pantelides, S. T. (1978), *Reviews of Modern Physics* **50**, 797.
- Pantelides, S. T., and C. T. Sah (1974), *Physical Review B* **10**, 621.
- Park, S. H., R. Rahman, G. Klimeck, and L. Hollenberg (2009), *Physical Review Letters* **103**.
- Park, S. J., A. Persaud, J. A. Liddle, J. Nilsson, J. Bokor, D. H. Schneider, I. W. Rangelow, and T. Schenkel (2004), *Microelectronic Engineering* **73-4** (SI), 695.
- Paul, D. J., J. R. A. Cleaver, H. Ahmed, and T. E. Whall (1993), *Applied Physics Letters* **63** (5), 631.
- Payette, C., K. Wang, P. J. Koppinen, Y. Dovzhenko, J. C. Sturm, and J. R. Petta (2012), *Applied Physics Letters* **100**, 043508.
- Peters, M. G., S. G. Den Hartog, J. I. Dijkhuis, O. J. A. Buyk, and L. W. Molenkamp (1998), *Journal of Applied Physics* **84**, 5052.
- Petta, J. R., A. C. Johnson, J. M. Taylor, E. A. Laird, A. Yacoby, M. D. Lukin, C. M. Marcus, M. P. Hanson, and A. C. Gossard (2005), *Science* **309** (5744), 2180.
- Phillips, J. C. (1962), *Physical Review* **125**, 1931.
- Pierre, M., R. Wacquez, X. Jehl, M. Sanquer, M. Vinet, and M. Cueto (2010), *Nature Nanotechnology* **5**, 133.
- Podd, G., S. Angus, D. Williams, and A. Ferguson (2010), *Applied Physics Letters* **96** (8), 082104.
- Poindexter, E. H., and P. J. Caplan (1983), *Progress in Surface Science* **14** (3), 201.
- Prada, M., R. H. Blick, and R. Joynt (2008), *Physical Review B* **77** (11), 115438.
- Prance, J. R., Z. Shi, C. B. Simmons, D. E. Savage, M. G. Lagally, L. R. Schreiber, L. M. K. Vandersypen, M. Friesen, R. Joynt, S. N. Coppersmith, and M. A. Eriksson (2012), *Physical Review Letters* **108** (4), 46808.
- Prati, E., M. Belli, S. Cocco, G. Petretto, and M. Fanciulli (2011), *Applied Physics Letters* **98** (5).
- Pudalov, V. M., S. G. Semenchinskii, and V. S. Édel'Man (1985), *JETP Letters* **41** (6).
- Qassemi, F., W. A. Coish, and F. K. Wilhelm (2009), *Physical Review Letters* **102** (17), 176806.
- Qian, G. F., Y. C. Chang, and J. R. Tucker (2005), *Physical Review B* **71** (4), 045309.
- Rahman, R., G. P. Lansbergen, S. H. Park, J. Verduijn, G. Klimeck, S. Rogge, and L. C. L. Hollenberg (2009a), *Physical Review B* **80** (16).
- Rahman, R., G. P. Lansbergen, J. Verduijn, G. C. Tettamanzi, S. H. Park, N. Collaert, S. Biesemans, G. Klimeck, L. C. L. Hollenberg, and S. Rogge (2011a), *Physical Review B* **84** (11), 115428.
- Rahman, R., R. P. Mueller, J. E. Levy, M. S. Carroll, and G. Klimeck (2010), *Physical Review B* **82** (15), 155315.
- Rahman, R., S. H. Park, T. B. Boykin, G. Klimeck, S. Rogge, and L. C. L. Hollenberg (2009b), *Physical Review B* **80** (15), 155301.
- Rahman, R., S. H. Park, G. Klimeck, and L. C. L. Hollenberg (2011b), *Nanotechnology* **822** (22), 225202.
- Rahman, R., J. Verduijn, N. Kharche, G. P. Lansbergen, G. Klimeck, L. C. L. Hollenberg, and S. Rogge (2011c), *Physical Review B* **83** (19), 195323.
- Rahman, R., C. J. Wellard, F. R. Bradbury, M. Prada, J. H. Cole, G. Klimeck, and L. C. L. Hollenberg (2007), *Physical Review Letters* **99** (3), 36403.
- Raith, M., P. Stano, and J. Fabian (2011), *Physical Review B* **83** (19), 195318.
- Ramdas, A. K., and S. Rodriguez (1981), *Reports on Progress in Physics* **44** (12), 1297.
- Rashba, E. (1960), *Soviet Physics Solid State* **2**, 1109.
- Reimann, S. M., and M. Manninen (2002), *Reviews of modern physics* **74** (4), 1283.
- Ricco, B., and M. Azbel (1984), *Physical Review B* **29** (4), 1970.
- Roche, B., E. Dupont-Ferrier, B. Voisin, M. Cobian, X. Jehl, R. Wacquez, M. Vinet, Y. M. Niquet, and M. Sanquer (2012), *Physical Review Letters* **108** (20), 206812.
- Roddaro, S., A. Fuhrer, P. Brusheim, C. Fasth, H. Q. Xu,

- L. Samuelson, J. Xiang, and C. M. Lieber (2008), *Physical Review Letters* **101** (18), 186802.
- Rokhinson, L. P., L. J. Guo, S. Y. Chou, and D. C. Tsui (2000), *Applied Physics Letters* **76**, 1591.
- Rokhinson, L. P., L. J. Guo, S. Y. Chou, and D. C. Tsui (2001), *Physical Review B* **63** (3), 035321.
- Ross, F. M., R. M. Tromp, and M. C. Reuter (1999), *Science* **286** (5446), 1931.
- Roth, L. M. (1960), *Physical Review* **118**, 1534.
- Rowan, L. G., E. L. Hahn, and W. B. Mims (1965), *Physical Review* **137** (1A), A61.
- Ruess, F. J., A. P. Micolich, W. Pok, K. E. J. Goh, A. R. Hamilton, and M. Y. Simmons (2008), *Applied Physics Letters* **92** (5).
- Ruess, F. J., L. Oberbeck, K. E. J. Goh, M. J. Butcher, E. Gauja, A. R. Hamilton, and M. Y. Simmons (2005), *Nanotechnology* **16** (10), 2446.
- Ruess, F. J., L. Oberbeck, M. Y. Simmons, K. E. J. Goh, A. R. Hamilton, T. Hallam, S. R. Schofield, N. J. Curson, and R. G. Clark (2004), *Nano Letters* **4** (10), 1969.
- Ruess, F. J., W. Pok, T. C. G. Reusch, M. J. Butcher, K. E. J. Goh, L. Oberbeck, G. Scappucci, A. R. Hamilton, and M. Y. Simmons (2007a), *Small* **3** (4), 563.
- Ruess, F. J., B. Weber, K. E. J. Goh, O. Klochan, A. R. Hamilton, and M. Y. Simmons (2007b), *Physical Review B* **76** (8).
- Saikin, S., and L. Fedichkin (2003), *Physical Review B* **67** (16), 161302.
- Sailer, J., V. Lang, G. Abstreiter, G. Tsuchiya, K. M. Itoh, J. W. Ager III, E. E. Haller, D. Kupidura, D. Harbusch, S. Ludwig, and D. Bougeard (2009), *Physica Status Solidi* **3**, 61.
- Sakr, M., H. Jiang, E. Yablonovitch, and E. Croke (2005), *Applied Physics Letters* **87** (22), 223104.
- Sanquer, M., M. Specht, L. Ghenim, S. Deleonibus, and G. Guegan (2000), *Physical Review B* **61** (11), 7249.
- Saraiva, A., M. Calderón, X. Hu, S. Das Sarma, and B. Koiller (2009), *Physical Review B* **80**, 081305(R).
- Saraiva, A. L., M. J. Calderón, X. Hu, S. Das Sarma, and B. Koiller (2010), *Arxiv preprint arXiv:1006.3338*.
- Sarovar, M., K. C. Young, T. Schenkel, and K. B. Whaley (2008), *Physical Review B* **78** (24), 245302.
- Schäffler, F. (1997), *Semiconductor Science and Technology* **12**, 1515.
- Schäffler, F., D. Tobben, H.-J. Herzog, G. Abstreiter, and B. Hollander (1992), *Semicond Sci Tech* **7**, 260.
- Schenkel, T., A. Persaud, S. J. Park, J. Nilsson, J. Bokor, J. A. Liddle, R. Keller, D. H. Schneider, D. W. Cheng, and D. E. Humphries (2003), *Journal of Applied Physics* **94** (11), 7017.
- Schoelkopf, R. J., P. Wahlgren, A. A. Kozhevnikov, P. Delsing, and D. E. Prober (1998), *Science* **280** (5367), 1238.
- Schofield, S. R., N. J. Curson, M. Y. Simmons, F. J. Ruess, T. Hallam, L. Oberbeck, and R. G. Clark (2003), *Physical Review Letters* **91** (13).
- Scott-Thomas, J. H. F., S. Field, M. A. Kastner, H. I. Smith, and D. A. Antoniadis (1989), *Physical Review Letters* **62** (5), 583.
- Seamons, J. A., E. Bielejec, M. S. Carroll, and K. D. Childs (2008), *Applied Physics Letters* **93**, 043124.
- Seitz, F., and D. Turnbull, Eds. (1957), in *Solid State Physics*, Vol. 5 (Academic Press, New York) pp. 257–320.
- Sellier, H., G. P. Lansbergen, J. Caro, S. Rogge, N. Collaert, I. Ferain, M. Jurczak, and S. Biesemans (2006), *Physical Review Letters* **97** (20), 206805.
- Shaji, N., C. B. Simmons, M. Thalakulam, L. J. Klein, H. Qin, H. Luo, D. E. Savage, M. G. Lagally, A. J. Rimberg, R. Joynt, M. Friesen, R. H. Blick, S. N. Coppersmith, and M. A. Eriksson (2008), *Nature Physics* (4), 540.
- Sham, L. J., and M. Nakayama (1979), *Physical Review B* **20** (2), 734.
- Shi, Z., C. B. Simmons, J. Prance, J. K. Gamble, M. Friesen, D. E. Savage, M. G. Lagally, S. N. Coppersmith, and M. A. Eriksson (2011), *Applied Physics Letters* **99**, 233108.
- Shi, Z., C. B. Simmons, J. R. Prance, J. K. Gamble, T. S. Koh, Y.-P. Shim, X. Hu, D. E. Savage, M. G. Lagally, M. A. Eriksson, M. Friesen, and S. N. Coppersmith (2012), *Physical Review Letters* **108**, 140503, arXiv:1110.6622.
- Shiau, S., and R. Joynt (2007), *Physical Review B* **76** (20), 205314.
- Shiau, S.-Y., S. Chutia, and R. Joynt (2007), *Physical Review B* **75** (19), 195345.
- Shin, S. J., C. S. Jeong, B. J. Park, T. K. Yoon, J. J. Lee, S. J. Kim, J. B. Choi, Y. Takahashi, and D. G. Hasko (2010), *Arxiv preprint arXiv:1001.3724*.
- Shin, Y. S., R. Brunner, A. Shibatomi, T. Obata, T. Otsuka, J. Yoneda, Y. Shiraki, K. Sawano, Y. Tokura, Y. Harada, K. Ishibashi, and S. Tarucha (2011), *Semiconductor Science and Technology* **26**, 055004.
- Shinada, T., M. Hori, and F. Guagliardo (2011), *IEDM*, 978.
- Shinada, T., T. Kurosawa, H. Nakayama, Y. Zhu, M. Hori, and I. Ohdomari (2008), *Nanotechnology* **19** (34).
- Shinada, T., S. Okamoto, T. Kobayashi, and I. Ohdomari (2005), *Nature* **437** (7062), 1128.
- Simmel, F., D. A. Wharam, M. A. Kastner, and J. P. Kotthaus (1999), *Physical Review B* **59** (16), R10441.
- Simmons, C. B., T. S. Koh, N. Shaji, M. Thalakulam, L. J. Klein, H. Qin, H. Luo, D. E. Savage, M. G. Lagally, A. J. Rimberg, R. Joynt, R. Blick, M. Friesen, S. N. Coppersmith, and M. A. Eriksson (2010), *Physical Review B* **82**, 245312.
- Simmons, C. B., J. R. Prance, B. J. Van Bael, T. S. Koh, Z. Shi, D. E. Savage, M. G. Lagally, R. Joynt, M. Friesen, S. N. Coppersmith, and M. A. Eriksson (2011), *Physical Review Letters* **106** (15), 156804.
- Simmons, C. B., M. Thalakulam, B. M. Rosemeyer, B. J. Van Bael, E. K. Sackmann, D. E. Savage, M. G. Lagally, R. Joynt, M. Friesen, S. N. Coppersmith, and M. A. Eriksson (2009), *Nano Letters* **9** (9), 3234.
- Simmons, C. B., M. Thalakulam, N. Shaji, L. J. Klein, H. Qin, R. H. Blick, D. E. Savage, M. G. Lagally, S. N. Coppersmith, and M. A. Eriksson (2007), *Applied Physics Letters* **91**, 213103.
- Simmons, M. Y., F. J. Ruess, K. E. J. Goh, T. Hallam, S. R. Schofield, L. Oberbeck, N. J. Curson, A. R. Hamilton, M. J. Butcher, R. G. Clark, and T. C. G. Reusch (2005), *Molecular Simulation* **31** (6-7), 505.
- Skinner, A. J., M. E. Davenport, and B. Kane (2003), *Physical Review Letters* **90** (8), 87901.
- Slichter, C. (1990), *Principles of magnetic resonance* (Springer-Verlag).
- Slinker, K. A., K. L. M. Lewis, C. C. Haselby, S. Goswami, L. Klein, J. Chu, S. Coppersmith, R. Joynt, R. Blick, M. Friesen, and M. A. Eriksson (2005), *New Journal of Physics* **7**, 246.
- Smit, G. D. J., S. Rogge, J. Caro, and T. M. Klapwijk (2003), *Physical Review B* **68** (19), 193302.
- Smit, G. D. J., S. Rogge, J. Caro, and T. M. Klapwijk (2004),

- Physical Review B **70** (3), 35206.
- Sorokin, P. B., P. V. Avramov, A. G. Kvashnin, D. G. Kvashnin, S. G. Ovchinnikov, and A. S. Fedorov (2008), Physical Review B **77**, 235417.
- Srinivasan, S. T., G. Klimeck, and L. P. Rokhinson (2008), Applied Physical Letters **93** (11).
- Stangl, J., V. Holý, and G. Bauer (2004), Reviews of modern physics **76** (3), 725.
- Steger, M., K. Saeedi, M. L. W. Thewalt, J. J. L. Morton, H. Riemann, N. V. Abrosimov, P. Becker, and H. J. Pohl (2012), Science **336** (6086), 1280.
- Stegner, A. R., C. Boehme, H. Huebl, M. Stutzmann, K. Lips, and M. S. Brandt (2006), Nature Physics **2** (12), 835.
- Steiger, S., M. Povolotskyi, H.-H. Park, T. Kubis, and G. Klimeck (2011), IEEE Transactions on Nanotechnology.
- Steimle, R. F., R. Muralidhar, R. Rao, M. Sadd, C. T. Swift, J. Yater, B. Hradsky, S. Straub, H. Gasquet, L. Vishnubhotla, E. J. Prinz, T. Merchant, B. Acred, K. Chang, and B. White Jr. (2007), Microelectronics Reliability **47** (4), 585.
- Stoneham, A. M., A. J. Fisher, and P. T. Greenland (2003), Journal of Physics: Condensed Matter **15**, L447.
- Stutzmann, M., and D. K. Biegelsen (1983), Physical Review B **28** (11), 6256.
- Sugii, N., K. Nakagawa, Y. Kimura, S. Yamaguchi, and M. Miyao (1998), Semiconductor science and technology **13**, A140.
- Sze, S. M., and K. K. Ng (1981), *Physics of semiconductor devices*, 2nd ed. (Wiley).
- Tabe, M., D. Moraru, M. Ligowski, M. Anwar, R. Jablonski, Y. Ono, and T. Mizuno (2010), Physical Review Letters **105** (1), 016803.
- Tahan, C. (2007), Arxiv preprint arXiv:0710.4263.
- Tahan, C., M. Friesen, and R. Joynt (2002), Physical Review B **66** (3), 035314.
- Tahan, C., and R. Joynt (2005), Physical Review B **71** (7), 75315.
- Takahashi, Y., M. Nagase, H. Namatsu, K. Kurihara, K. Iwdate, Y. Nakajima, S. Horiguchi, K. Murase, and M. Tabe (1994), in *Electron Devices Meeting, 1994. IEDM'94. Technical Digest., International* (IEEE) pp. 938–940.
- Takahashi, Y., M. Nagase, H. Namatsu, K. Kurihara, K. Iwdate, Y. Nakajima, S. Horiguchi, K. Murase, and M. Tabe (1995), Electronics Letters **31** (2), 136.
- Takahashi, Y., Y. Ono, A. Fujiwara, and H. Inokawa (2002), Journal of Physics: Condensed Matter **14**, R995.
- Takashina, K., Y. Ono, A. Fujiwara, Y. Takahashi, and Y. Hirayama (2006), Physical Review Letters **96** (23), 236801.
- Tan, K. Y., K. W. Chan, M. Möttönen, A. Morello, C. Yang, J. A. van Donkelaar, A. D. C. Alves, J.-M. Pirkkalainen, D. N. Jamieson, R. G. Clark, and A. S. Dzurak (2010), Nano Letters **10** (1), 11.
- Taylor, J. M., H. A. Engel, W. Dur, A. Yacoby, C. M. Marcus, P. Zoller, and M. D. Lukin (2005), Nature Physics **1** (3), 177.
- Testolin, M. J., A. D. Greentree, C. J. Wellard, and L. C. L. Hollenberg (2005), Physical Review B **72** (19), 195325.
- Tettamanzi, G. C., J. Verduijn, G. P. Lansbergen, M. Blaauboer, M. J. Calderón, R. Aguado, and S. Rogge (2012), Physical Review Letters **108** (4), 046803.
- Tezuka, H., A. R. Stegner, A. M. Tyryshkin, S. Shankar, M. L. W. Thewalt, S. A. Lyon, K. M. Itoh, and M. S. Brandt (2010), Physical Review B **81** (16).
- Thalakulam, M., C. B. Simmons, B. J. V. Bael, B. M. Rosemeyer, D. E. Savage, M. G. Lagally, M. Friesen, S. N. Coppersmith, and M. A. Eriksson (2011), Physical Review B **84**, 045307.
- Thalakulam, M., C. B. Simmons, B. M. Rosemeyer, D. E. Savage, M. G. Lagally, M. Friesen, S. N. Coppersmith, and M. A. Eriksson (2010), Applied Physics Letters **96**, 183104.
- Thilderkvist, A., M. Kleverman, G. Grossmann, and H. G. Grimmeiss (1994), Physical Review B **49** (20), 14270.
- Tilke, A. T., F. C. Simmel, R. H. Blick, H. Lorenz, and J. P. Kotthaus (2001), Progress in quantum electronics **25** (3), 97.
- Tracy, L. A., E. P. Nordberg, R. W. Young, C. B. Pinilla, H. L. Stalford, G. A. T. Eyck, K. Eng, K. D. Childs, J. R. Wendt, R. K. Grubbs, J. Stevens, M. P. Lilly, M. A. Eriksson, and M. S. Carroll (2010), Applied Physics Letters **97**, 192110.
- Trauzettel, B., D. V. Bulaev, D. Loss, and G. Burkard (2007), Nature Physics **3** (3), 192.
- Tsai, D. B., P. W. Chen, and H. S. Goan (2009), Physical Review A **79** (6), 060306.
- Tsai, D. B., and H. Goan (2008), AIP Conference Proceedings, Solid-State Quantum Computing **1074**, 50.
- Tyryshkin, A., S. Lyon, W. Jantsch, and F. Schäffler (2005), Physical Review Letters **94** (12), 126802.
- Tyryshkin, A. M., S. A. Lyon, A. V. Astashkin, and A. M. Raitsimring (2003), Physical Review B **68** (19).
- Tyryshkin, A. M., S. Tojo, J. J. L. Morton, H. Riemann, N. V. Abrosimov, P. Becker, H. J. Pohl, T. Schenkel, M. L. W. Thewalt, K. M. Itoh, *et al.* (2011), Nature Materials **11** (2), 143.
- Usman, M., S. Heck, E. Clarke, P. Spencer, H. Ryu, R. Murray, and G. Klimeck (2011a), Journal of Applied Physics **83**.
- Usman, M., H. Ryu, I. Woo, D. Ebert, and G. Klimeck (2009), IEEE Transactions on Nanotechnology **8**, 330.
- Usman, M., Y.-H. M. Tan, H. Ryu, S. S. Ahmed, H. J. Hubert J Krenner, T. B. Boykin, and G. Klimeck (2011b), IOP Nanotechnology **22**.
- Van der Vaart, N. C., A. T. Johnson, L. P. Kouwenhoven, D. J. Maas, W. de Jong, M. P. de Ruyter van Steveninck, A. van der Enden, C. J. P. M. Harmans, and C. T. Foxon (1993), Physica B: Condensed Matter **189** (1-4), 99.
- Verduijn, J., G. C. Tettamanzi, G. P. Lansbergen, N. Collaert, S. Biesemans, and S. Rogge (2010), Applied Physics Letters **96** (7), 072110.
- Verduijn, J., G. C. Tettamanzi, R. Wacquez, B. Roche, B. Voisin, X. Jehl, M. Sanquer, and S. Rogge (2012), submitted **z**, **x**.
- Vinh, N. Q., P. T. Greenland, K. Litvinenko, B. Redlich, A. F. G. Van Der Meer, S. A. Lynch, M. Warner, A. M. Stoneham, G. Aeppli, D. J. Paul, *et al.* (2008), Proceedings of the National Academy of Sciences **105** (31), 10649.
- Vorojtsov, S., E. R. Mucciolo, and H. U. Baranger (2004), Physical Review B **69** (11), 115329.
- Vrijen, R., E. Yablonoitch, K. Wang, H. W. Jiang, A. Balandin, V. Roychowdhury, T. Mor, and D. P. DiVincenzo (2000), Physical Review A **62** (1), 12306.
- Wacquez, R., M. Vinet, M. Pierre, B. Roche, X. Jehl, O. Cueto, J. Verduijn, G. C. Tettamanzi, S. Rogge, V. Deshpande, B. Previtali, C. Vizios, S. Pauliac-Vaujour, C. Comboroure, N. Bove, O. Faynot, and M. Sanquer (2010), in *2010 IEEE Symposium on VLSI Technology* (IEEE) pp. 193–194.
- Wagner, R. S., and W. C. Ellis (1964), Applied Physics Letters **4**, 89.

- Van de Walle, C. G., and R. M. Martin (1986), *Physical Review B* **34** (8), 5621.
- Wang, L., K. Shen, B. Y. Sun, and M. W. Wu (2010), *Physical Review B* **81** (23), 235326.
- Wang, L., and M. W. Wu (2011), *Journal of Applied Physics* **110** (4), 043716.
- Wasshuber, C., H. Kosina, and S. Selberherr (1997), *IEEE transactions on computer-aided design of integrated circuits and systems* **16** (9), 937.
- Waugh, F., M. Berry, D. Mar, R. Westervelt, K. Campman, and A. Gossard (1995), *Physical Review Letters* **75** (4), 705.
- Weber, B. (2012), *Physical Review B*.
- Weber, B., S. Mahapatra, H. Ryu, S. Lee, A. Fuhrer, T. Reusch, D. Thompson, W. C. T. Lee, G. Klimeck, L. Hollenberg, and M. Y. Simmons (2012), *Science* **335**, 64.
- Weber, W. M., L. Geelhaar, A. P. Graham, E. Unger, G. S. Duesberg, M. Liebau, W. Pamler, C. Chèze, H. Riechert, P. Lugli, *et al.* (2006), *Nano Letters* **6** (12), 2660.
- Wegewijs, M. R., and Y. V. Nazarov (2001), Arxiv preprint cond-mat/0103579.
- Weis, C. D., A. Schuh, A. Batra, A. Persaud, I. W. Rangelow, J. Bokor, C. C. Lo, S. Cabrini, E. Sideras-Haddad, G. D. Fuchs, R. Hanson, D. D. Awschalom, and T. Schenkel (2008), *Journal Of Vacuum Science & Technology B* **26** (6), 2596.
- Weitz, P., R. Haug, K. von Klitzing, and F. Schäffler (1996), *Surface Science* **361-362**, 542.
- Wellard, C. J., and L. C. L. Hollenberg (2001), *Quantum Communication, Computing, and Measurement* (3), 247.
- Wellard, C. J., and L. C. L. Hollenberg (2002), *Journal of Physics D - Applied Physics* **35** (20), 2499.
- Wellard, C. J., and L. C. L. Hollenberg (2004), *Journal of Physics - Condensed Matter* **16** (32), 5697.
- Wellard, C. J., and L. C. L. Hollenberg (2005), *Physical Review B* **72** (8), 85202.
- Wellard, C. J., L. C. L. Hollenberg, and S. Das Sarma (2006), *Physical Review B* **74** (7), 075306.
- Wellard, C. J., L. C. L. Hollenberg, and C. I. Pakes (2002), *Nanotechnology* **13** (5), 570.
- Wellard, C. J., L. C. L. Hollenberg, F. Parisoli, *et al.* (2003), *Physical Review B* **68** (19), 195209.
- Van der Wiel, W. G., T. Fujisawa, S. Tarucha, and L. P. Kouwenhoven (2003), *Reviews of Modern Physics* **75** (1), 1.
- Wild, A., J. Kierig, J. Sailer, J. Ager III, E. Haller, G. Abstreiter, S. Ludwig, and D. Bougeard (2012), *Applied Physics Letters* **100**, 143110.
- Wild, A., J. Sailer, J. Nützel, G. Abstreiter, S. Ludwig, and D. Bougeard (2010), *New Journal of Physics* **12**, 113019.
- Wilson, D. K., and G. Feher (1961), *Physical Review* **124**, 1068.
- Wilson, H. F., O. Warschkow, N. A. Marks, S. R. Schofield, N. J. Curson, P. Smith, M. W. Radny, D. R. McKenzie, and M. Y. Simmons (2004), *Physical Review Letters* **93** (22).
- Witzel, W. M., M. S. Carroll, A. Morello, L. Cywiński, and S. Das Sarma (2010), *Physical Review Letters* **105** (18), 187602.
- Witzel, W. M., and S. Das Sarma (2006), *Physical Review B* **74** (3), 035322.
- Witzel, W. M., X. Hu, and S. Das Sarma (2007), *Physical Review B* **76** (3), 035212.
- Witzel, W. M., R. de Sousa, and S. Das Sarma (2005), *Physical Review B* **72** (16), 161306.
- Wolf, S. (1990), *Process integration*, Silicon processing for the VLSI era (Lattice Press).
- Xiao, M., M. G. House, and H. W. Jiang (2010a), *Physical Review Letters* **104** (9), 096801.
- Xiao, M., M. G. House, and H. W. Jiang (2010b), *Applied Physics Letters* **97** (3), 032103.
- Xiao, M., I. Martin, E. Yablonovitch, and H. W. Jiang (2004), *Nature* **430** (6998), 435.
- Xie, P., Y. Hu, Y. Fang, J. Huang, and C. M. Lieber (2009), *Proceedings of the National Academy of Sciences* **106** (36), 15254.
- Yamahata, G., T. Kodera, H. O. H. Churchill, K. Uchida, C. M. Marcus, and S. Oda (2011), Arxiv preprint arXiv:1111.6873.
- Yang, C., Z. Zhong, and C. M. Lieber (2005), *Science* **310** (5752), 1304.
- Yang, C. H., W. H. Lim, F. A. Zwanenburg, and A. S. Dzurak (2011), *AIP Advances* **1** (4), 042111.
- Yao, W., R. Liu, and L. Sham (2006), *Physical Review B* **74** (19), 195301.
- Yonenaga, I., M. Sakurai, and M. H. F. Sluite (2007), *Trans Tech, Stafa-Zurich, SUISSE*.
- Yonenaga, I., M. Sakurai, M. H. F. Sluite, Y. Kawazoe, and S. Muto (2005), *Journal of materials science. Materials in electronics* **16** (7), 429.
- Yu, P. Y., and M. Cardona (2001), *Fundamentals of Semiconductors*, 3rd ed. (Springer-Verlag, Berlin).
- Yuan, M., F. Pan, Z. Yang, T. J. Gilheart, F. Chen, D. E. Savage, M. G. Lagally, M. A. Eriksson, and A. J. Rimberg (2011), *Applied Physics Letters* **98**, 142104.
- Zaknoon, B., G. Bahir, C. Saguy, R. Edrei, A. Hoffman, R. A. Rao, R. Muralidhar, and K. M. Chang (2008), *Nano Letters* **8** (6), 1689.
- Zandvriet, H. J. W., and H. B. Elswijk (1993), *Physical Review B* **48**.
- Zhong, Z., Y. Fang, W. Lu, and C. M. Lieber (2005), *Nano Letters* **5** (6), 1143.
- Zimmerman, N. M., B. J. Simonds, A. Fujiwara, Y. Ono, Y. Takahashi, and H. Inokawa (2007), *Applied Physics Letters* **90** (3), 033507.
- Žutić, I., J. Fabian, and S. D. Sarma (2004), *Reviews of Modern Physics* **76** (2), 323.
- Zwanenburg, F. A., A. A. van Loon, G. A. Steele, C. E. W. M. van Rijmenam, T. Balder, Y. Fang, C. M. Lieber, and L. P. Kouwenhoven (2009a), *Journal of Applied Physics* **105** (12), 124314.
- Zwanenburg, F. A., C. E. W. M. van Rijmenam, Y. Fang, C. M. Lieber, and L. P. Kouwenhoven (2009b), *Nano Letters* **9** (3), 1071.